UNIVERSITY OF ROCHESTER
LABORATORY FOR LASER ENERGETICS

Volume 109
October–December 2006
DOE/SF/19460-739

LLE Review

Quarterly Report

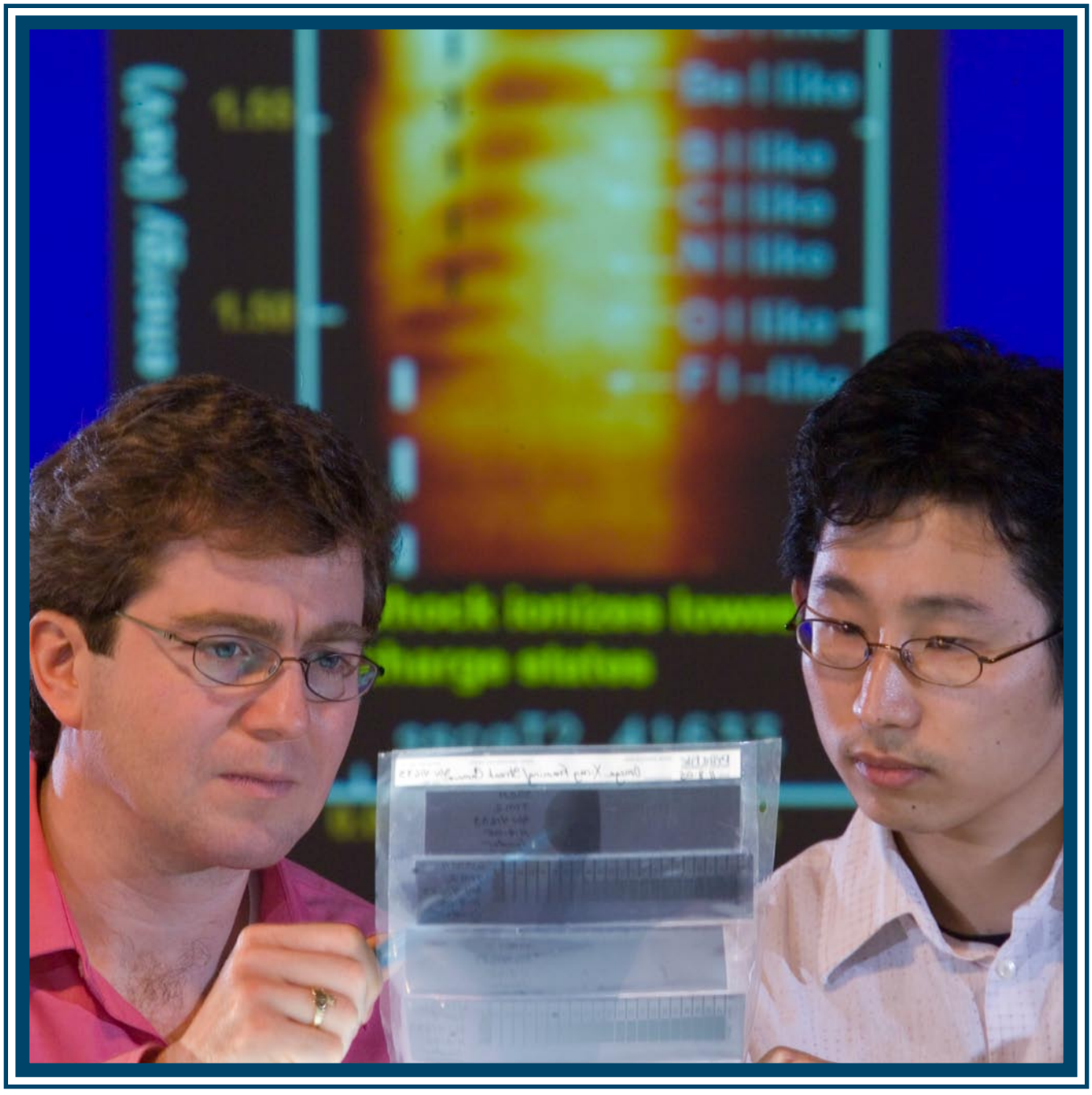

About the Cover:

Senior Scientist Sean Regan (left) and graduate student Hiroshi Sawada (right) (of the Department of Mechanical Engineering) analyze an x-ray absorption spectrum measured on the OMEGA Laser System. The time-resolved spectrum was recorded on film using an x-ray streak camera outfitted with a Bragg crystal spectrometer. A digital image of the absorption spectrum is projected in the background. An investigation of thermal transport in direct-drive targets is the main subject of Mr. Sawada's Ph.D. thesis research. The shock-heating and heat-front penetration resulting from the laser-ablation process are examined spectroscopically using a point-source x-ray backlighter. When the shock, and subsequently the heat front, reach the buried Al tracer layer in a planar plastic target, the Al is ionized and a time history of the electron temperature is inferred from the Al absorption spectral features. Experimental results of shock heating for direct-drive targets along with laser-absorption and mass-ablation-rate measurements are compared with simulations of the one-dimensional hydrodynamics code *LILAC* (see "Laser Absorption, Mass Ablation Rate, and Shock Heating in Direct-Drive Inertial Confinement Fusion," p. 1).

In preparation for a shot day on the OMEGA Laser System, Senior Scientist Sean Regan (principal investigator) presents the experimental objectives of the shock-heating campaign to the watchstanders at the 0800 Pre-Watch Briefing. Watchstanders are responsible for different aspects of the laser operation, including experimental operations, laser drivers, beamline operations, power conditioning, and amplifiers. Thirty watchstanders are needed for a 12-h shot day on OMEGA, which requires pre-watch system-startup activities beginning at 0400.

The work described in this volume includes current research at the Laboratory for Laser Energetics, which is supported by New York State Energy Research and Development Authority, the University of Rochester, the U.S. Department of Energy Office of Inertial Confinement Fusion under Cooperative Agreement No. DE-FC52-92SF19460, and other agencies.

Printed in the United States of America
Available from
National Technical Information Services
U.S. Department of Commerce
5285 Port Royal Road
Springfield, VA 22161
Price codes: Printed Copy A04
Microfiche A01

For questions or comments, contact Igor Igumenshchev, Editor, Laboratory for Laser Energetics, 250 East River Road, Rochester, NY 14623-1299, (585) 275-4792.

Worldwide-Web Home Page: http://www.lle.rochester.edu/

UNIVERSITY OF ROCHESTER
LABORATORY FOR LASER ENERGETICS

Volume 109
October–December 2006
DOE/SF/19460-739

LLE Review

Quarterly Report

UR LLE

Contents

In Brief

This volume of the LLE Review, covering October–December 2006, features "Laser Absorption, Mass Ablation Rate, and Shock Heating in Direct-Drive Inertial Confinement Fusion," by S. P. Regan, R. Epstein, V. N. Goncharov, I. V. Igumenshchev, D. Li, P. B. Radha, H. Sawada, W. Seka, T. R. Boehly, J. A. Delettrez, O. V. Gotchev, J. P. Knauer, J. A. Marozas, F. J. Marshall, R. L. McCrory, P. W. McKenty, D. D. Meyerhofer, T. C. Sangster, S. Skupsky, V. A. Smalyuk, and B. Yaakobi (LLE); D. Shvarts, (Negev Research Center, Ben Gurion University, Israel); and R. C. Mancini (University of Nevada). In this article (p. 1), the authors report on direct-drive laser absorption, mass ablation rate, and shock-heating experimental studies on the OMEGA Laser System, which are used to validate hydrodynamic simulations. A comprehensive set of measurements tracking the flow of energy from the laser to the target was conducted. Time-resolved measurements of laser absorption in the corona are performed on spherical implosion experiments. The mass ablation rate is inferred from time-resolved Ti K-shell spectroscopic measurements of nonaccelerating, solid CH spherical targets with a buried tracer layer of Ti. Shock heating is diagnosed in planar-CH-foil targets using noncollective spectrally resolved x-ray scattering and also in targets with a buried tracer layer of Al using time-resolved x-ray absorption spectroscopy. A detailed comparison of the experimental results and the simulations indicates that a time-dependent flux limiter in the thermal transport model is required to simulate the laser-absorption measurements.

Additional highlights of research presented in this issue include the following:

- J. R. Rygg, J. A. Frenje, C. K. Li, F. H. Séguin, and R. D. Petrasso (Plasma Science and Fusion Center, MIT) along with J. A. Delettrez, V. Yu. Glebov, V. N. Goncharov, D. D. Meyerhofer, P. B. Radha, S. P. Regan, and T. C. Sangster (LLE) present results of nuclear measurements of fuel–shell mix in inertial confinement fusion implosions on OMEGA (p. 14). To probe the extent of mix, nuclear yields were measured from implosions of capsules containing a deuterated plastic (CD) layer and filled with pure ^{3}He. D^{3}He-proton spectral measurements have been used to constrain the amount of mix at shock time, to demonstrate that some of the fuel mixes with the CD layer, and that capsules with a higher initial fill density or thicker shell are less susceptible to the effects of mix.

- C. K. Li, F. H. Séguin, J. A. Frenje, J. R. Rygg, and R. D. Petrasso (Plasma Science and Fusion Center, MIT); R. P. J. Town, P. A. Amendt, S. P. Hatchett, O. L. Landen, A. J. Mackinnon, P. K. Patel, and M. Tabak (LLNL); and J. P. Knauer, T. C. Sangster, and V. A. Smalyuk (LLE) report on magnetic-field evolution and instabilities in laser-produced plasmas (p. 21). Monoenergetic proton radiography was used to make the first measurements of a laser–plasma-generated magnetic (B) field structure and evolution over a time interval that is longer compared to the laser pulse duration. While a circular, long-pulse (1-ns), low-intensity (~10^{14} W/cm^2) laser beam illuminates a plastic foil, a hemispherical plasma bubble forms and grows linearly, surrounded by a symmetric B field. After the laser turns off, the bubble continues to expand, but field strengths decay and the field structure around the edge becomes asymmetric through the resistive-interchange instability.

- T. J. B. Collins, J. A. Marozas, R. Betti, D. R. Harding, P. W. McKenty, P. B. Radha, S. Skupsky, V. N. Goncharov, J. P. Knauer, and R. L. McCrory present simulation results of the performance of the 1-MJ, wetted-foam target design for the National Ignition Facility (p. 26). Wetted-foam designs take advantage of the increased laser absorption provided by the higher-atomic-number elements in a target ablator composed of plastic foam saturated with deuterium–tritium. A stability analysis of a 1-MJ design was

performed using the two-dimensional hydrodynamic code *DRACO*. A nonuniformity-budget analysis has been constructed and suggests that two-dimensional smoothing by spectral dispersion (SSD) is needed to reduce single-beam nonuniformities to levels sufficient for ignition to proceed.

- J. Myatt, W. Theobald, J. A. Delettrez, C. Stoeckl, M. Storm, T. C. Sangster, A. V. Maximov, and R. W. Short present results of the modeling of petawatt laser-generated hot electrons in mass-limited, solid-foil–target interactions at "relativistic" laser intensities using copper targets and parameters motivated by recent experiments at the Rutherford Appleton Laboratory (RAL) Petawatt and 100-TW facilities (p. 37). Electron refluxing allows a unique determination of the laser–electron conversion efficiency and a test with simulations. Implications of the results for fast-ignition experiments on OMEGA EP are considered.

- D. H. Edgell, R. S. Craxton, L. M. Elasky, D. R. Harding, S. J. Verbridge, M. D. Wittman, and W. Seka present three-dimensional characterization of spherical cryogenic targets using ray-trace analysis of multiple shadowgraph views (p. 46). A 3-D ray-tracing model into the backlit optical shadowgraph analysis, which is the primary diagnostic for hydrogenic ice-layer characterization in cryogenic targets at LLE, was incorporated. The result is an improved self-consistent determination of the hydrogen/vapor surface structure for cryogenic targets up to mode numbers around $\ell_{\max} = 16$.

- L. Sun and J. R. Marciante present filamentation analysis in large-mode-area fiber lasers (p. 55). Starting from the paraxial wave equation, an analytic expression for filament thresholds in fiber lasers is derived. The occurrence of filamentation is determined by the larger of two thresholds—one of perturbative gain and one of spatial confinement. The threshold value is around a few megawatts.

- J. R. Marciante, W. R. Donaldson, and R. G. Roides present a technique for enhanced-dynamic-range, single-shot measurement of nanosecond optical pulses by averaging of replicated pulses (p. 61). A dynamic-range enhancement of three bits is experimentally demonstrated and compared with conventional multi-shot averaging. This technique can be extended to yield an increase of up to seven bits of additional dynamic range over nominal oscilloscope performance.

Igor Igumenshchev
Editor

Laser Absorption, Mass Ablation Rate, and Shock Heating in Direct-Drive Inertial Confinement Fusion

Introduction

Inertial confinement fusion (ICF) occurs when a spherical shell target containing cryogenic thermonuclear fuel (i.e., DT) is imploded.[1–9] The implosion is initiated by the ablation of material from the outer surface using either intense laser beams (direct drive)[3,5,6,8,9] or x rays produced in a high-Z enclosure (indirect drive).[4,7] The ablated shell mass forms a coronal plasma that surrounds the target and accelerates the shell inward via the rocket effect. When the higher-density shell converges toward the target center and is decelerated by the lower-density fuel, a hot spot forms. Compression by the cold, dense shell causes the pressure and DT fusion reaction rate of the hot spot to increase. It is predicted that the α-particle fusion products will deposit sufficient energy in the hot spot to launch a thermonuclear burn wave out through the cold, dense fuel in the shell just prior to stagnation when the areal density of the hot spot exceeds 0.3 g/cm^2 and the hot-spot temperature reaches 10 keV (Ref. 4). Energy gain with hot-spot ignition depends on the implosion velocity of the shell V_{imp}, the shell areal density ρR_{shell} at the time of burn, and the in-flight shell adiabat $\alpha = P_{\text{fuel}} \big/ P_{\text{Fermi}}$, defined as the ratio of the pressure in the main fuel layer P_{fuel} to the Fermi-degenerate pressure P_{Fermi}.[4,10–12]

A physical understanding of the energy transport from the laser to the target is required to develop capsule designs that can achieve energy gain with ICF. An experimental investigation of direct-drive energy coupling is the subject of this article. The 60-beam, 30-kJ, 351-nm OMEGA Laser System[13] is used to irradiate millimeter-scale, spherical and planar plastic and cryogenic D_2 and DT targets on nanosecond time scales with peak intensities I ranging from 10^{13} to 10^{15} W/cm^2. High levels of laser drive uniformity are achieved with 2-D smoothing by spectral dispersion (SSD) and polarization smoothing (PS).[14] The three major parts of energy coupling—laser absorption, electron thermal transport, and shock heating of the target—were diagnosed with a wide variety of experiments. The experimental results are compared with the simulations of the 1-D hydrodynamics code *LILAC*,[15] which is used to design ignition targets for the 1.8-MJ, 351-nm, 192-beam National Ignition Facility (NIF).[16] The initial design of a direct-drive-ignition target relies on 1-D simulations to optimize the energetics of the implosion. Subsequent calculations are performed with the 2-D hydrodynamics code *DRACO* to mitigate the deleterious effects of hydrodynamic instabilities on target performance.[17] Energy coupling to the target is primarily a 1-D effect; therefore, comparisons of experimental results with 1-D *LILAC* simulations are presented. The physics of direct-drive energy coupling is similar for plastic and cryogenic targets. The initial coupling is identical since cryogenic targets have a thin plastic ablator; however, the subsequently formed lower-Z, hydrogen-isotope, coronal plasma absorbs less laser energy. Plastic targets reduce the complexity and cost of the experiment and increase the shot rate.

ICF target acceleration and deceleration are realized when hot, low-density plasma pushes against cold, high-density plasma, making the target implosion inherently susceptible to the Rayleigh–Taylor (RT) hydrodynamic instability.[4–9,18–20] High-gain, direct-drive ICF target implosions require accurate predictions of the shell adiabat α since it defines the minimum energy needed for hot-spot ignition and the amount of ablative stabilization in the RT growth rate. The shell adiabat is tuned by varying the temporal pulse shape of the laser irradiation. The minimum energy for hot-spot ignition scales as $E_{\min} \propto \left(\alpha^{1.8} \big/ V_{\text{imp}}^{5.8}\right)$ (Refs. 11 and 12); hence, low-adiabat implosions with high-implosion velocities require less laser energy to ignite. A higher adiabat at the ablation front reduces the RT growth rate $\gamma_{\text{RT}} = \alpha_{\text{RT}} \sqrt{kg} - \beta_{\text{RT}} V_a$, where α_{RT} and β_{RT} are constants, k is the wave number of the perturbation, and g is the target acceleration (Refs. 18 and 19), by increasing the ablative stabilization term,[21,22] which is proportional to the velocity of the ablation front with respect to the unablated shell V_a. The ablation velocity depends on the shell adiabat $V_a \propto \alpha^{3/5}$ (Ref. 19). A balance must be struck between the laser energy and the shell stability constraints to choose a shell adiabat.

A schematic of direct-drive energy coupling is presented in Fig. 109.1. After the initial breakdown of the target surface with the intense laser beams, the laser light no longer propagates to the ablation front. Instead, the expanding coronal plasma forms a critical electron density $n_{\text{cr}} = \pi mc^2 \big/ e^2 \lambda_L^2$, where m is the

electron mass, c is the speed of light, e is the electron charge, and λ_L is the laser wavelength, and the laser energy is absorbed primarily via inverse bremsstrahlung in the underdense corona having electron densities less than the critical density $n_e \le n_{cr}$, where $n_{cr}\,(\lambda_L = 351\text{ nm}) = 9 \times 10^{21}\text{ cm}^{-3}$. The fraction of laser energy absorbed in the corona, f_{abs}, is inferred from measurements of the scattered light.

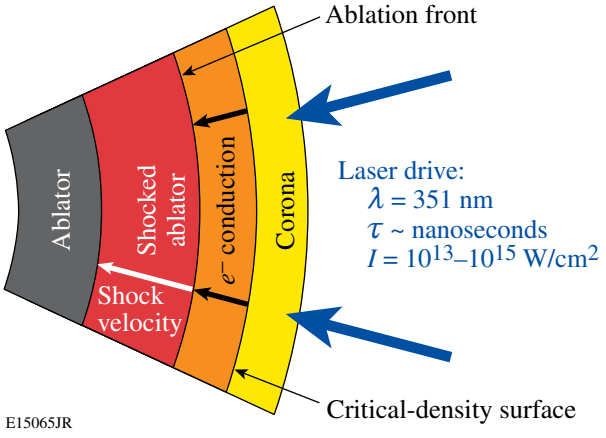

Figure 109.1
Diagram illustrating the flow of energy from the laser to the target in direct-drive ICF. Typical laser irradiation conditions are listed. The laser energy is absorbed in the corona at densities less than the critical density via inverse bremsstrahlung. Thermal electron conduction transports the absorbed energy to the ablation front. Laser ablation launches a shock wave in the ablator or shell of the target.

As shown in Fig. 109.1, the energy flows from the critical-density surface to the ablation front via electron thermal transport. This process is calculated in *LILAC*[15] using a flux-limited thermal transport model.[23] The efficiency η_{hydro} of this process can be obtained by comparing the mass ablation rate $\dot{m}$ to the measured laser absorption fraction f_{abs}.[4] The mass ablation rate is inferred from time-resolved x-ray burnthrough measurements of laser-driven targets with buried high-Z tracer layers.[24–34] To eliminate the early burnthrough due to the RT instability growth,[34] the measurements are performed on solid, plastic spherical targets. In contrast to an accelerating, spherical shell target with a buried high-Z layer, a solid target does not accelerate and is not susceptible to the RT instability; therefore, the burnthrough measurement will be affected only by the laser ablation. The effects of the Richtmyer–Meshkov instability on the burnthrough experiments presented here have been estimated to be negligible. Both the ablation pressure P and the mass ablation rate depend on the amount of energy coupled to the ablation front: $P \propto (f_{abs}\eta_{hydro}I)^{2/3}$ and $\dot{m} \propto \left(f_{abs}\eta_{hydro}I\right)^{1/3}$, and the implosion velocity is proportional to the ratio of the ablation pressure to the mass ablation rate $V_{imp} \propto \left(P/\dot{m}\right)$ (Ref. 4).

The laser ablation process launches a shock wave into the target that compresses and heats the shell (Fig. 109.1). This primary source of heating determines the adiabat for the bulk of the shell. X-ray radiation and energetic electrons provide additional but lower levels of shell heating. Diagnosing the plasma conditions in the shock-heated shell and modeling its equation of state are challenging since they straddle the boundaries between Fermi-degenerate, strongly coupled, and weakly coupled plasmas (i.e., $10^{23}\text{ cm}^{-3} < n_e < 10^{24}\text{ cm}^{-3}$ and $10\text{ eV} < T_e < 40\text{ eV}$). Such plasmas are too cold to emit x rays and too dense to be probed with optical Thomson scattering. The amount of shock heating in planar-CH-foil targets was diagnosed with time-resolved x-ray absorption spectroscopy[35–37] and noncollective spectrally resolved x-ray scattering.[38]

The implosion can be divided into four stages: shock propagation, acceleration phase, deceleration phase, and peak compression. This article concentrates on the first two stages, when the laser irradiates the target and when the shell adiabat is set. It is organized as follows: A description of the 1-D hydrodynamics code and its predictions are presented in **1-D Hydrodynamics Code** (p. 2). The scattered-light measurements are presented in **Laser-Absorption Experiment** (p. 3). The laser-driven burnthrough measurements are described in **Mass-Ablation-Rate Experiment** (p. 5). The shock-heating measurements are presented in **Shock-Heating Experiment** (p. 8). Throughout this article, the highly reproducible experimental results achieved with a high level of laser drive uniformity are shown to constrain the modeling of direct-drive energy transport from the laser to the target. The limitations of the flux-limited thermal-transport model[23] and further improvements in the modeling are presented in **Discussion** (p. 11). A nonlocal treatment of the thermal transport, which is in progress,[39] is expected to improve agreement between the simulation and the experiment.

1-D Hydrodynamics Code

Direct-drive implosions on the OMEGA Laser System are routinely simulated with the 1-D hydrodynamics code *LILAC*.[15] This code is used to design high-gain, direct-drive implosions for the NIF.[6,8,9] The electron thermal conduction that throttles the energy flow in direct-drive ICF is challenging to model.[23,39,40] As described below, it is currently simulated with a flux-limited thermal-transport model. The main objective of this detailed investigation is to tune the physics models in *LILAC* by comparing the predicted laser absorption, mass ablation rate, and shock heating with the measured quantities. Accurate simulations of OMEGA experiments will instill confidence in the target designs for the NIF.

A detailed description of *LILAC* can be found elsewhere[15] with the main features of the code described in this section. Laser absorption is calculated using a ray-trace algorithm that models inverse bremsstrahlung. Transport of radiation is modeled through multigroup diffusion with the Los Alamos National Laboratory Astrophysical Tables[41] providing the opacities. The *SESAME* tables are used to model the equation of state. *LILAC* uses a flux-limited Spitzer–Härm[42] electron-thermal-conduction model that calculates the effective heat flux q_{eff} using a sharp cutoff model [i.e., $q_{\text{eff}} = \min(q_{\text{SH}}, fq_{\text{FS}})$]. The heat flux is proportional to the temperature gradient $q_{\text{SH}} = -\kappa\nabla T_e$. In the region where $q_{\text{SH}} > q_{\text{FS}}$, the heat flux is calculated as a fraction f of the free stream limit $q_{\text{FS}} = nT_eV_T$, where κ is the heat conductivity, T_e is the electron temperature, $V_T = \sqrt{T_e/m_e}$ is the thermal electron velocity, and n_e is the electron density. The coefficient f is commonly referred to as a "flux limiter." Typical values of f for simulations of direct-drive experiments are $0.04 < f < 0.1$. The larger the flux limiter, the closer the heat flux is to the classical Spitzer–Härm limit.

The classical heat-transport theory of Spitzer–Härm is valid when the mean free path of the electron is much smaller than the temperature-gradient length of the plasma. This is not a good approximation for the steep gradients near the critical density in direct-drive ICF. Nonlocal energy-transport calculations have been proposed using Fökker–Planck codes to model the heat flux in direct-drive ICF when the temperature scale length is a few electron mean free paths;[40] however, until recently such calculations have been implemented with limited success in hydrodynamics codes.[43] A new nonlocal-transport model using a simplified Boltzmann equation (Krook model) has been developed and incorporated in *LILAC*.[39]

Laser-Absorption Experiment

The fraction of laser energy absorbed in the corona is inferred from power measurements of the 351-nm light scattered from spherical implosions[44–47] of cryogenic D_2 and plastic-shell targets.[48] Scattered light is detected behind two focusing lenses in the full-aperture backscatter stations (FABS) of beams 25 and 30: time-resolved spectra and calorimetric measurements are recorded.[49] Time-resolved spectra of the scattered light collected between the focusing lenses are also recorded. The scattered light is assumed to be distributed uniformly over 4π since the calculated deviations from isotropy are in the 1% to 2% range. As shown in Fig. 109.2, there is good agreement (within ±2% rms) between time-integrated

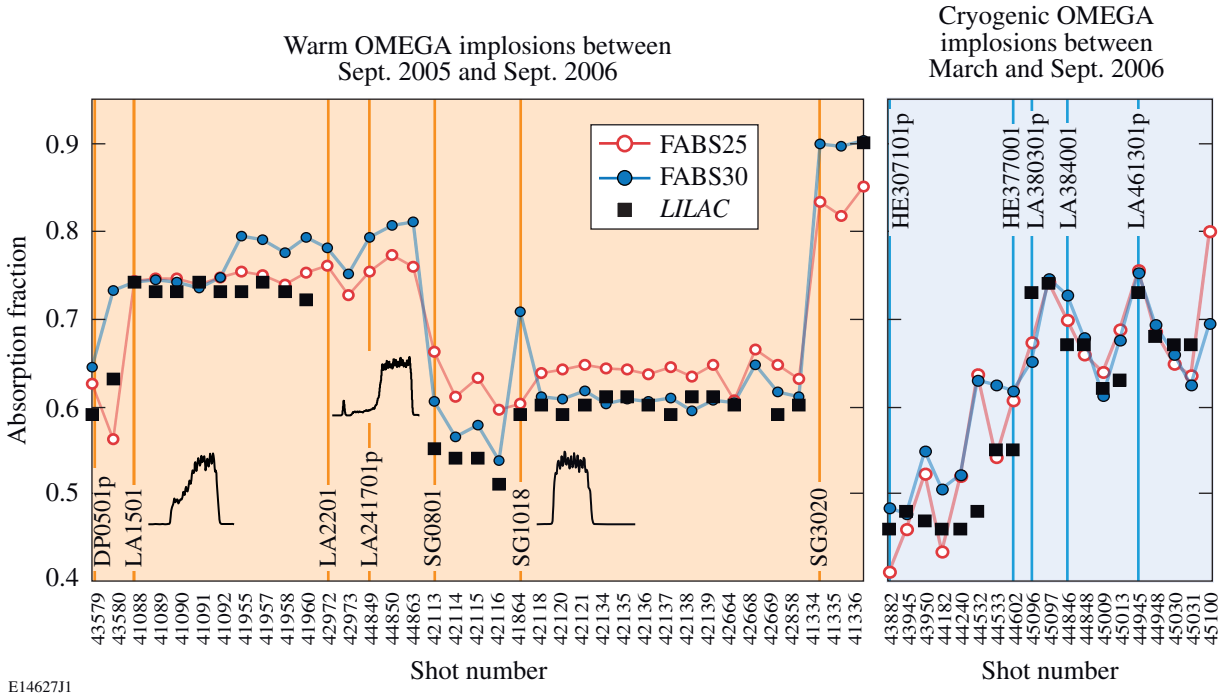

Figure 109.2
Time-integrated laser-absorption fraction measured on OMEGA for a variety of targets, laser pulse shapes, and irradiation energies. Good agreement is observed between the *LILAC* prediction (square symbols) and the measurements recorded in beams 25 and 30 (circle symbols) with the full-aperture backscatter stations (FABS25 and FABS30).

absorption data and the *LILAC* predictions for a wide variety of targets, laser pulse shapes, and irradiation energies. (The overall accuracy of the FABS calorimetry is estimated at 1% to 2% rms. Systematic errors of ≤3% between the calorimeters in the two FABS stations arise from the shot-to-shot variations in the transmissions of the blast shields protecting the OMEGA focus lenses that are coated with target debris from experiments. These errors are calibrated and corrected during routine system maintenance every few weeks.)

Since the shell adiabat is tuned by varying the temporal pulse shape of the laser irradiation, power measurements of the scattered light are essential to characterize the drive. The time-resolved scattered-light spectrum presented in Fig. 109.3(a) was recorded for the shaped laser pulse drive shown on a linear scale in Fig. 109.3(a) and a log scale in Fig. 109.3(b). The laser pulse has a low-intensity foot followed by a higher-intensity main drive. The shell adiabat is set during the foot portion of the pulse. A comparison of the time histories of the measured, spectrally integrated, scattered-light signal and the *LILAC* prediction is shown in Fig. 109.3(b). Two flux limiters were considered: $f = 0.06$ and $f = 0.1$. Overall the *LILAC* prediction for the scattered-light power is in good agreement with the measurement over more than three orders of magnitude; however, some differences (10% of the absolute scattered-light fraction) are observed that could affect the shock dynamics (i.e., shock timing and shock strength). It is difficult to ascribe a single rms error estimate to the time-resolved absorption (or scattered-light) measurements. The absorption and scattering processes are affected by detailed coronal plasma conditions created by the incident laser pulse shape. During the first 100 ps of the laser pulse and at low intensities, the discrepancy can be as high as 50% or more without affecting the time-integrated absorption, while later in the plasma evolution, nonlinear effects can instantaneously lead to enhanced scattering of up to 10%. These discrepancies are well outside the experimental error bars, which depend on the dynamic range and the recording intensities on the streak camera. The discrepancy revealed with the scattered-light power is not evident in shock-velocity measurements, which can discriminate between the flux limiters under consideration.[39,50]

The measured absorption is systematically higher than predicted during the first 100 to 200 ps of the laser pulse. This is difficult to see in Fig. 109.3(b) because of the compressed time scale. The higher absorption at early times during the initial plasma formation is more apparent with a double-picket laser pulse (i.e., a train of two 100-ps laser pulses separated by 400 ps with ~12 J/beam in the first pulse and ~18 J/beam in the second pulse) experiment. The double-picket laser pulse shape is presented in Fig. 109.4(a), with the resulting streaked spectrum of the measured scattered light shown in Fig. 109.4(b).

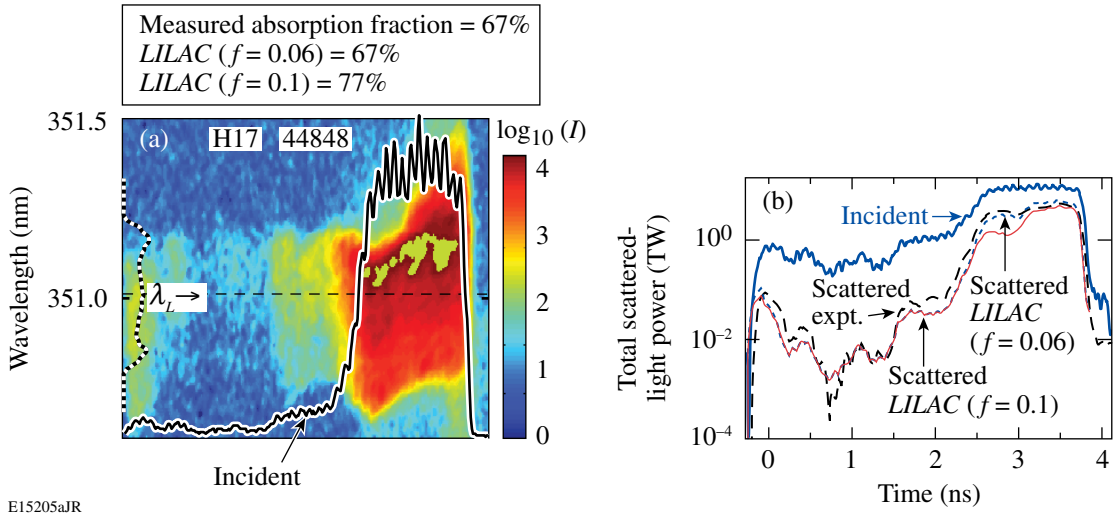

Figure 109.3
(a) Time-resolved spectral measurement of 351-nm scattered laser light for a shaped laser pulse irradiating a spherical DT cryogenic implosion target having a 95-μm-thick cryogenic DT layer inside a 5.4-μm-thick CD shell. The incident pulse shape (solid curve) and the broad incident spectrum (dotted curve) are overplotted on linear scales. (b) Spectrally integrated power measurement of scattered laser light (dashed curve) recorded with a laser pulse shape (bold solid curve) incident on target. *LILAC* predictions for two flux limiters are shown: $f = 0.06$ (dotted curve) and $f = 0.1$ (solid curve). Time-integrated laser absorption fractions are listed for the three scattered-light curves.

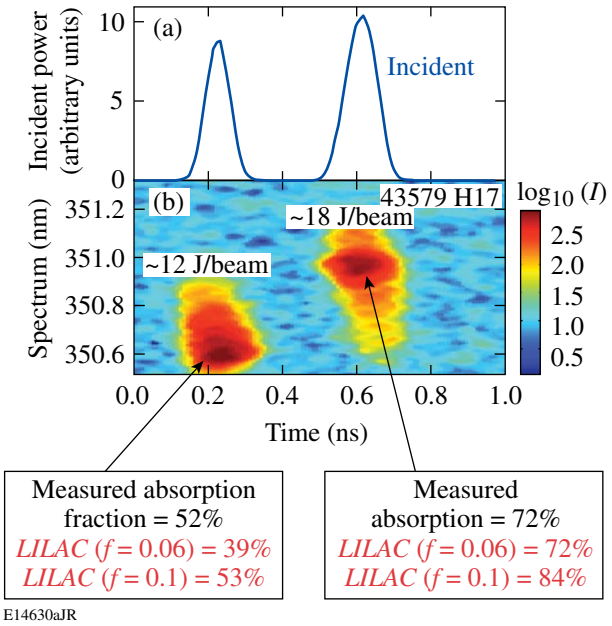

Figure 109.4
(a) Intensity of double-picket laser pulse shape irradiating a spherical plastic target, and (b) associated time-resolved, spectral measurement of scattered laser light. Measured time-integrated laser absorption fractions are listed for the two 100-ps picket pulses and compared with the *LILAC* predictions for two flux limiters ($f = 0.06$ and $f = 0.1$). The first pulse has ~12 J/beam and the second pulse has ~18 J/beam.

Although the 52% temporally integrated absorption fraction inferred from the experiment for the first peak is higher than the 39% *LILAC* prediction with $f = 0.06$, a simulation with a higher flux limiter of $f = 0.1$ (predicted absorption fraction = 53%) matches the experimental result. After the corona is established with the first pulse, the measured absorption fraction of the second pulse (72%) is matched with the lower flux limiter (predicted absorption fraction = 72%), while the higher flux limiter of $f = 0.1$ overpredicts an absorption fraction of 84%. Therefore, the flux limiter needs to vary in time to simulate the measured absorption fraction. Fokker–Planck simulations have predicted a time-varying flux limiter.[43] The enhanced absorption at early times is likely due to resonance absorption at very low $I\lambda_L^2 < 10^{13}\ \mathrm{W}\mu\mathrm{m}^2/\mathrm{cm}^2$ with concomitant low energetic electron production ($T_h < 10$ keV). In the overall energetics this enhanced absorption is negligible; however, the energetic electrons can deposit their energy in the shell.

The time-resolved scattered-light spectra shown in Figs. 109.3(a) and 109.4(b) contain significant information. The initial rapid blue shift in the spectra is directly related to the rapid buildup of the plasma corona whose optical path length decreases as the plasma size increases. This is most easily seen in Fig. 109.4(b) where the incident laser bandwidth was very narrow compared to the scattered-light spectra shown. In addition, the broad incident spectrum presented in Fig. 109.3(a) (dotted line) changes dramatically during the high-intensity part of the laser pulse, indicating that nonlinear processes are changing the spectra and possibly the scattered-light levels. A detailed investigation of these spectra is currently underway.

Mass-Ablation-Rate Experiment

The mass ablation rate is inferred from time-resolved x-ray burnthrough measurements[24–34] of solid, spherical plastic targets with buried tracer layers of Ti. Hydrodynamic instabilities are expected to have negligible effects on the inferred mass ablation rate since these targets do not accelerate. The 1-D simulations show that the shell trajectory of an imploding target has a negligible effect on the mass ablation rate for the 1-ns square laser pulse; therefore, the non-accelerating, solid, spherical burnthrough target is predicted to have a mass ablation rate similar to the shell target. The target shown in Fig. 109.5 is irradiated with 60 beams smoothed with 2-D SSD and PS,[14] using a 23-kJ, 1-ns square laser pulse with a peak intensity of 1×10^{15} W/cm^2. The ablation time is measured for three ablator thicknesses (2, 5, and 8 μm) to sample the mass ablation rate at different times during the laser pulse. It is predicted that the mass ablation rate for the 1-ns square laser pulse, having near-constant laser irradiation, has small temporal variations; therefore, the burnthrough experiment is not preferentially sampling particular times during the laser pulse. The mass ablation rate is inferred from the onset of the K-shell emission of the ablated Ti tracer layer. Prior to ablation the Ti layer is too cold to emit x rays; however, as the Ti is ablated into the hot corona, a significant fraction of

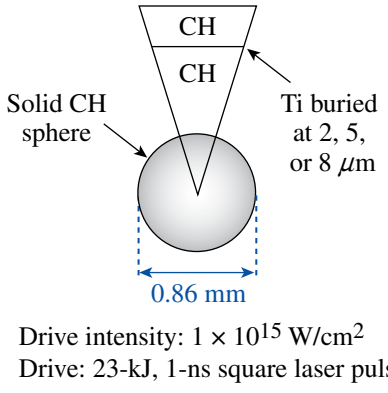

Figure 109.5
Diagram of nonaccelerating target used for laser-driven burnthrough experiment. The solid, spherical plastic (CH) target has a buried tracer layer of Ti (0.1 μm thick). The target specifications and laser irradiation conditions are shown.

its population is ionized to the He-like and H-like charge states and emits K-shell emission in the 4.5- to 5.5-keV photon energy range. The experimental signature of burnthrough is given by the Ti He_α emission.

Time-resolved, Ti K-shell spectroscopic measurements were performed with x-ray streak cameras[51] outfitted with a Bragg crystal spectrometer that used a flat RbAP (rubidium acid phthalate) crystal to disperse the spectrum onto a gold photocathode. The time axis for the streaked x-ray spectra was established as follows: The streak speed of the camera is calibrated using a temporally modulated ultraviolet laser pulse (i.e., a sequence of eight consecutive Gaussian laser pulses having a 548-ps period). The temporal resolution, defined by the streak speed and the photocathode slit width, is 50 ps. Defining the time $t = 0$ is challenging because the initial x-ray emission from the target is below the detection threshold of the diagnostic. Using the 4.5-keV x-ray continuum emission as a timing fiducial, the absolute timing is determined by synchronizing the measured pulse with the simulated one as described below. The synchronization is performed for each flux limiter under consideration since the temporal shape of the x-ray pulse depends on the flux limiter. The standard deviation of the difference between the measured and simulated x-ray pulse duration is 50 ps; therefore, the uncertainty in the measured burnthrough time is estimated to be ±50 ps. The spectra recorded for the 2-μm CH ablator are shown in Fig. 109.6(a). The laser strikes the target at $t = 0$ ns and the onset of the Ti He_α signature burnthrough emission occurs around 0.3 ns. A similar measurement is presented in Fig. 109.6(b) for the 8-μm CH ablator. The spectral resolving power ($E/\Delta E \sim 50$) is limited by source broadening but is clearly high enough to resolve the prominent Ti K-shell emissions. The streaked spectra presented in Fig. 109.6 show that the burnthrough occurs later for the target with the thicker CH ablator, as expected.

Weak Ca K-shell emissions are observed in the burnthrough x-ray spectra of Fig. 109.6. Calcium is a surface contaminant of the solid plastic target introduced during production of the sphere. The calcium layer is ablated into the coronal plasma and emits K-shell emission around the same time as Ti. It is an experimental artifact that does not affect the measured burnthrough time.

The x-ray emission from the corona is simulated by post-processing the *LILAC* prediction with the time-dependent atomic physics code *Spect3D*.[52] As mentioned above, the x-ray continuum emission from the target during the first few hundred picoseconds is below the detection threshold of the diagnostic; therefore, the absolute timing of the measurement is established by synchronizing the measured x-ray continuum in the 4.5-keV range with the *LILAC*/*Spect3D* prediction. The

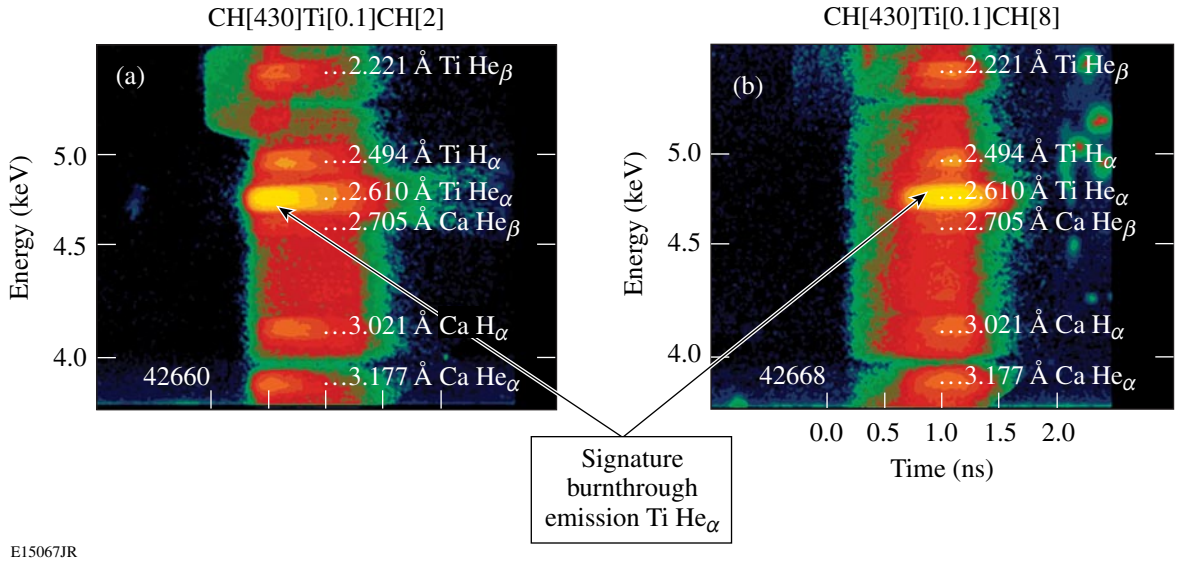

Figure 109.6
(a) Streaked x-ray spectrum recorded on a laser-driven burnthrough experiment with the prominent Ti K-shell emissions identified for the 2-μm-thick CH ablator. The mass ablation rate is inferred from the signature Ti He_α emission. (b) Streaked x-ray spectrum for the 8-μm-thick CH ablator. Calcium is a surface contaminant of the solid plastic target introduced during production of the sphere. The calcium layer is ablated into the coronal plasma and emits K-shell emission around the same time as Ti.

synchronized x-ray pulses are shown in Fig. 109.7(a) for the 8-μm CH ablator. In Fig. 109.7(b), the temporal evolution of the Ti He$_\alpha$ emission predicted with *LILAC*/*Spect3D* is compared with the measured burnthrough emission for the 8-μm CH ablator. Two flux limiters ($f = 0.06$ and $f = 0.1$) were considered, and the experimental results are closer to the predictions with the higher flux-limiter value. Comparisons of the predicted and measured burnthrough times for these two flux limiters are presented in Fig. 109.8 for the ablators under consideration. The burnthrough time is defined as the time at which the Ti He$_\alpha$ emission reaches 10% of its peak intensity. It is clear from Fig. 109.8 that the burnthrough experiment is more consistent with the higher mass ablation rate of the *LILAC* prediction with $f = 0.1$. A flux limiter of $f = 0.1$ was also needed to simulate the

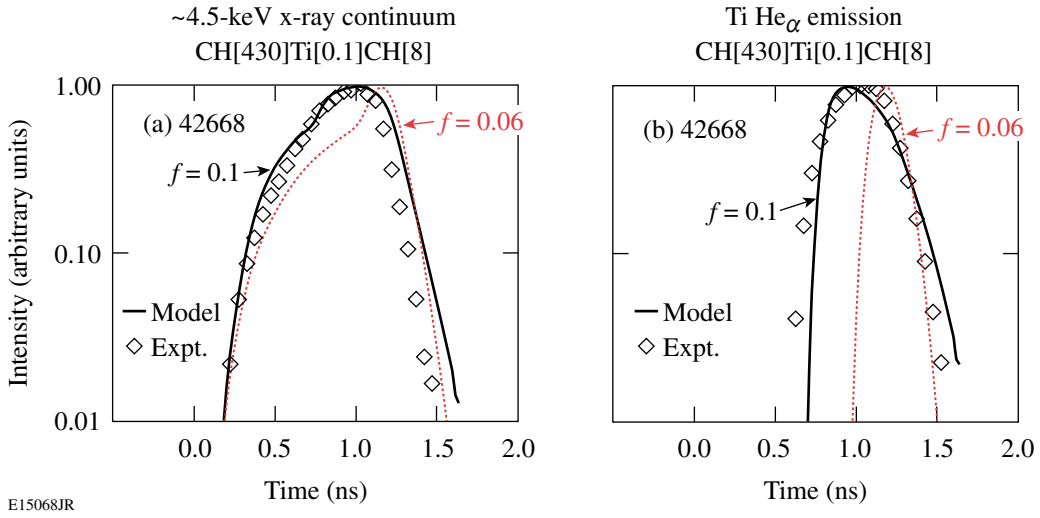

Figure 109.7
(a) Time histories of the measured (diamond symbols) and simulated (dotted curve for $f = 0.06$ and solid curve for $f = 0.1$) x-ray continuum in the ~4.5-keV range, and (b) time histories of the measured (diamond symbols) and simulated (dotted curve for $f = 0.06$ and solid curve for $f = 0.1$) Ti He$_\alpha$ emission for the laser-driven burnthrough experiment.

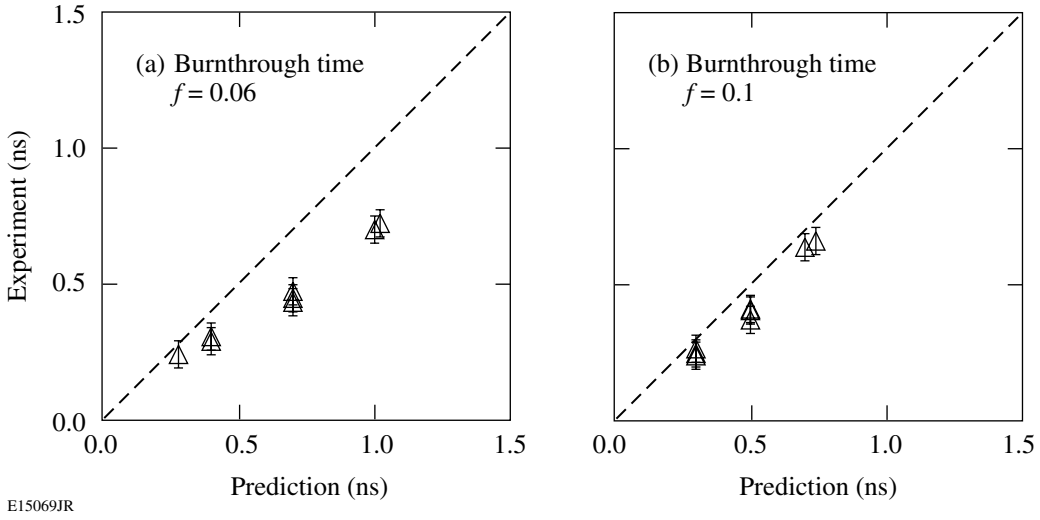

Figure 109.8
A comparison of the measured laser-driven burnthrough time and (a) the *LILAC* prediction with a flux limiter $f = 0.06$ and (b) the *LILAC* prediction with a flux limiter $f = 0.1$ for the three ablators under consideration.

ablation-front perturbation oscillations for Richtmyer–Meshkov instability experiments on OMEGA.[39,53]

Shock-Heating Experiment

The shock wave launched by laser ablation into the target is the primary source of heating for the bulk of the shell. X-ray radiation and energetic electrons from the corona can provide additional heating to portions of the shell near the ablation front. The amount of shock heating in planar-CH-foil targets was diagnosed using two techniques: time-resolved x-ray absorption spectroscopy and noncollective spectrally resolved x-ray scattering. A detailed description of the latter experiment can be found elsewhere.[38] The results of the former experiment will be briefly described in this section; however, a more detailed version will be published separately.[37] Planar geometry is a good approximation for the shell during the shock-propagation stage of the implosion since convergence can be neglected. It also provides better diagnostic access than a spherical shell target.

Local shell conditions were measured using time-resolved x-ray absorption spectroscopy of plastic foil targets with a buried tracer layer of Al as shown in Fig. 109.9. As the shock wave propagates through the Al, it compresses and ionizes the Al. The buried depth of the tracer layer is varied to probe the plasma conditions in different regions of the target. As shown in Fig. 109.10, Al 1*s*–2*p* x-ray absorption spectroscopy of a CH planar target with a buried Al tracer layer (1 to 2 μm thick) was performed with a point-source (i.e., <100-μm) Sm backlighter irradiated with laser intensities of ~10^{16} W/cm^2. The overall thickness (~50 μm) of the drive foil was chosen to delay the acceleration phase until after the absorption spectra were recorded, minimizing the influences of hydrodynamic instabilities on the measurements. The direct-drive target was irradiated with up to 18 laser beams that were smoothed with phase plates, 2-D SSD, and PS.[14] The overlapped intensity had a uniform drive portion with a 400-μm diameter and peak intensities in the range of 10^{14} to 10^{15} W/cm^2. The Sm M-shell emission in the 1.4- to 1.7-keV range overlaps the bound–bound absorption features of Al near 1.5 keV and probes the uniform drive portion of the target.[35]

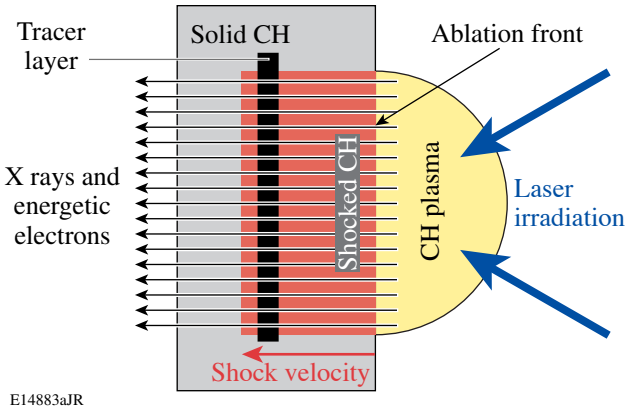

Figure 109.9
Diagram of the target used to diagnose the shock-heated conditions of a direct-drive ICF target. X-ray radiation and energetic electrons provide additional heating. X-ray absorption spectra of buried high-*Z* tracer layer are used to diagnose the plasma conditions in the shock-heated target. The position of the layer is varied to probe different regions of the target.

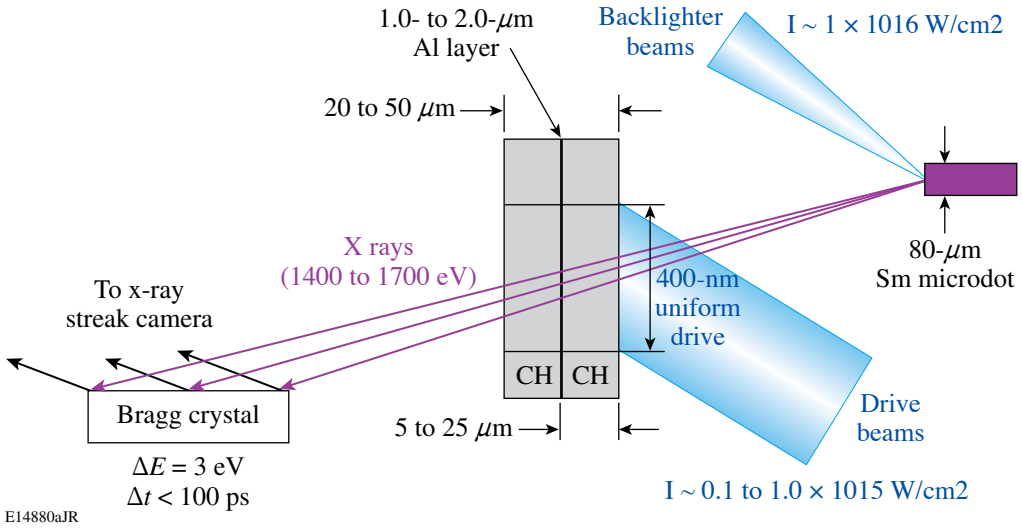

Figure 109.10
Layout of the Al 1*s*–2*p* absorption-spectroscopy experiment showing the Sm backlighter, the plastic drive foil with the buried Al layer, and the Bragg crystal spectrometer.

The frequency-dependent transmission of the shock-heated Al layer, obtained from the ratio $I(\nu)/I_0(\nu) = e^{[-\mu(\nu,n_e,T_e)\rho\Delta L]}$ of the transmitted backlighter spectrum $I(\nu)$ to the incident Sm spectrum $I_0(\nu)$, depends on the mass absorption coefficient μ and the areal density of the Al layer $\rho\Delta L$. The absorption coefficient is sensitive to variations in n_e and T_e for the shock-heated conditions under consideration.[36] The high electron densities cause the spectral line shapes of the bound–bound absorption features to be Stark-broadened beyond the instrumental spectral resolution (~3 eV). The incident and transmitted spectra were recorded with an x-ray streak camera[51] outfitted with a Bragg crystal spectrometer that used a flat RbAP crystal to disperse the spectrum onto a low-density CsI photocathode. The temporal resolution of the measurement was ~100 ps.

The sensitivity of the absorption spectroscopy to variations in the electron temperature is illustrated in Fig. 109.11. The predicted Al 1*s*–2*p* absorption spectra, obtained by post-processing the *LILAC* simulation for shot #44116 with the time-dependent atomic physics code *Spect3D*,[52] are compared to the electron temperature in the Al layer. The target had a 1-μm-thick Al layer buried at a depth of 10 μm in a 50-μm-thick CH target and was irradiated with a 1-ns square laser pulse having a peak intensity of 1×10^{15} W/cm^2. A flux limiter of 0.06 was used for the simulation. The electron temperature in the Al layer was calculated as follows: The *LILAC*/*Spect3D* spectra

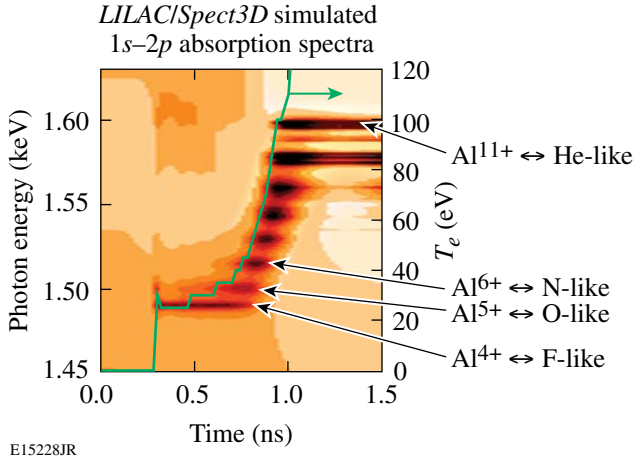

Figure 109.11
Temporal evolution of the Al 1*s*–2*p* absorption spectrum simulated with *LILAC* using $f = 0.06$ and *Spect3D* for shot #44116. The target had a 1-μm-thick Al layer buried at a depth of 10 μm in a 50-μm-thick CH target and was irradiated with a 1-ns square laser pulse having a peak intensity of 1×10^{15} W/cm^2. The predicted electron temperature in the Al layer is also plotted (solid curve). Higher-charge states of Al are ionized in succession and absorb in 1*s*–2*p* transitions as T_e increases.

were compared with spectra calculated with the time-dependent atomic physics code PrismSPECT[52] assuming uniform shell conditions for various combinations of n_e and T_e. The best fit between the *LILAC*/*Spect3D* spectra and PrismSPECT was determined based on a least-squares-fitting routine, which inferred n_e and T_e simultaneously. The accuracy of the T_e inference is 10%, while the uncertainty of the n_e inference is about a factor of 2. The stair step in the simulated electron temperature observed in Fig. 109.11 around 0.5 ns is due to the discrete electron temperatures considered in the spectral fitting routine. Higher-charge states of Al are ionized in succession and absorb in 1*s*–2*p* transitions as the shell T_e increases. At time $t = 0$ ns, the laser irradiation of the target begins. When the shock propagates through the buried Al layer, the sharp rise in the temperature ionizes the Al and the lowest-charge states of Al (i.e., F-like and O-like) are observed in 1*s*–2*p* absorption. The second rise in electron temperature at 0.75 ns occurs when the heat front penetrates the Al layer and ultimately ionizes it to the K shell. The minimum electron temperature that can be currently diagnosed using this technique is ~10 eV.

Time-resolved x-ray absorption spectroscopy was performed using a 50-μm-thick target with a 1- or 2-μm-thick Al layer buried at a depth of 10 μm. Two laser intensities were studied: 1×10^{14} W/cm^2 generating a 10-Mbar shock and 1×10^{15} W/cm^2 generating a 50-Mbar shock. The predicted, shocked mass density in the Al layer for the higher intensity drive is ~8 g/cm^3. The streaked x-ray spectra are presented in Fig. 109.12 with the prominent absorption features identified. The cold K edge of Al can be observed prior to the shock arrival at the Al layer. The diagnostic utility of the temperature and density dependence of the K-edge shift is currently being studied. Only the F-like Al 1*s*–2*p* absorption feature is observed with the lower drive intensity [Fig. 109.12(a)]. The three lowest-charge states (F-like, O-like, and N-like) appear in absorption when shock heated by the higher intensity [Fig. 109.12(b)]. The Sm backlighter and the CH/Al/CH target have the same 1-ns square laser pulse drive, but the Sm backlighter was fired 200 ps earlier than the drive foil to optimize the backlighter brightness for the shock-heating period of the Al layer. The higher charge states associated with the heat-front penetration that are predicted in Fig. 109.11 are not observed in Fig. 109.12(b) because the Sm backlighter was off at that time. The temporal onset of the 1*s*–2*p* absorption depends on the buried depth of the Al layer and the shock velocity.

The measured spectral line shapes were compared with simulated absorption spectra calculated with *LILAC* and *Spect3D*.

A detailed description can be found elsewhere.[37] Reasonable agreement was observed for the lower drive intensity; however, the higher-charge states were observed in the measured absorption spectrum compared to the simulated absorption spectrum for the higher drive intensity. This indicates that the measured electron temperature is higher than the prediction. The measured spectra were compared with simulated spectra calculated with PrismSPECT[52] assuming uniform shell conditions for various combinations of n_e and T_e. The best fit to the measured spectra was determined based on a least-squares-fitting routine, which inferred n_e and T_e simultaneously. The electron density inferred from the higher laser drive intensity was 1×10^{24} cm^{-3} and for the lower drive intensity was 5×10^{23} cm^{-3}, consistent with the 1-D predictions. The time history comparing the predicted electron temperature with the measurements is shown in Fig. 109.13. Again, the simulated electron temperature was calculated as follows: (1) *LILAC* was post-processed with *Spect3D* and (2) the simulated absorption spectra were fitted with PrismSPECT, assuming uniform electron temperature and density in the Al layer. These calculations were performed

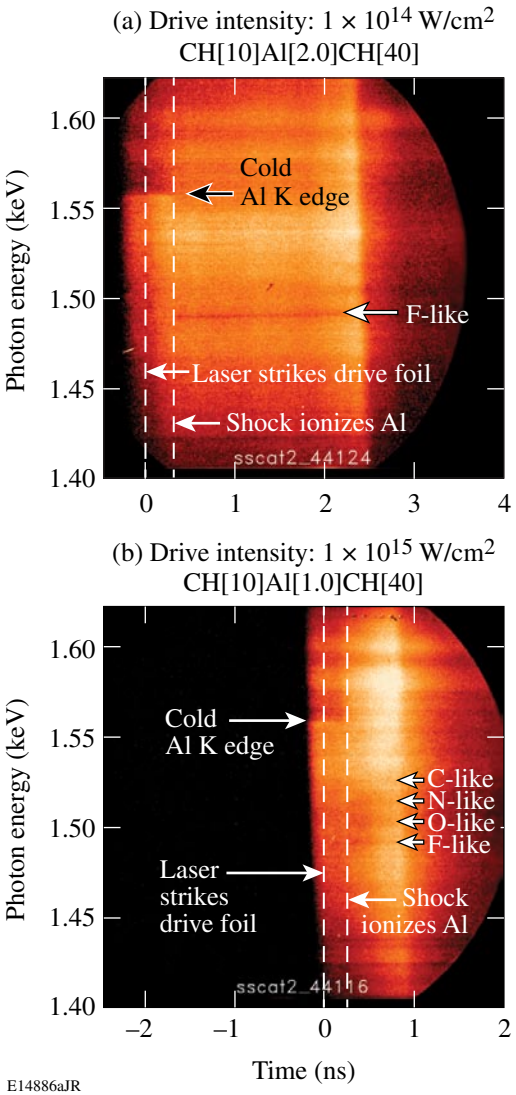

Figure 109.12
Time-resolved x-ray absorption spectra recorded for drive intensities of (a) 1×10^{14} W/cm^2 and (b) 1×10^{15} W/cm^2. The prominent absorption features are identified.

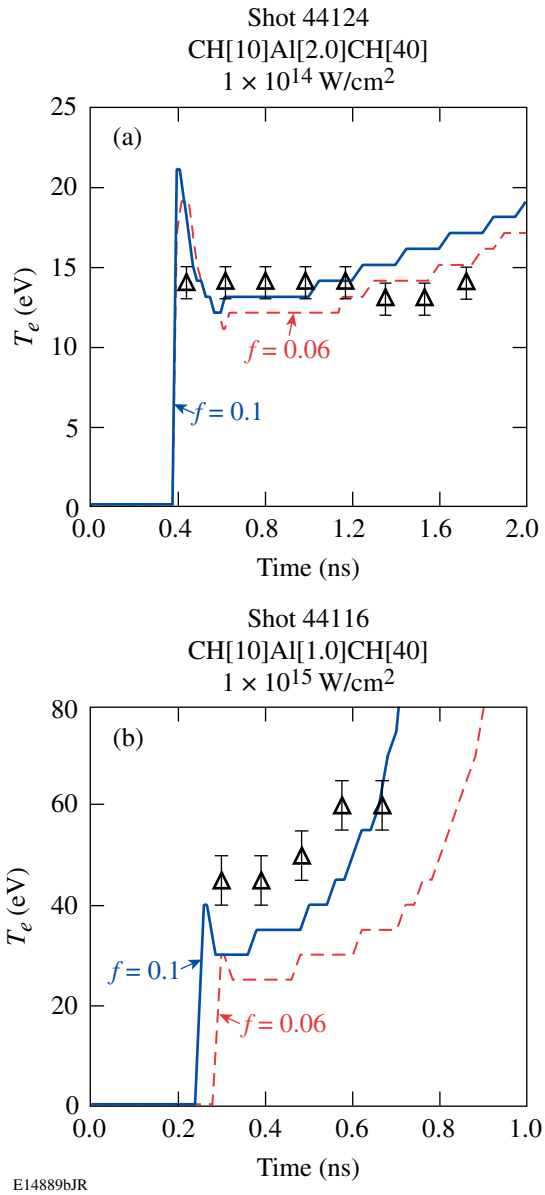

Figure 109.13
Comparison of time-resolved electron temperature in the Al layer inferred from the experiment (triangles) with *LILAC* simulations using $f = 0.06$ (dashed curves) and $f = 0.1$ (solid curves) for drive intensities of (a) 1×10^{14} W/cm^2 and (b) 1×10^{15} W/cm^2.

for two flux limiters ($f = 0.06$ and $f = 0.1$). For the lower drive intensity the predicted electron temperatures for both flux limiters are close to the time-resolved electron temperatures inferred from the measured absorption spectra [Fig. 109.13(a)]. These experimental measurements are consistent with the results from the noncollective spectrally resolved x-ray scattering experiment of a similar drive foil: an upper limit of $T_e = 20$ eV was inferred in those experiments.[38] The time-resolved electron temperatures inferred from the measured absorption spectra are higher than the simulated ones for the 1×10^{15} W/cm^2 drive intensity [Fig. 109.13(b)]. The simulation with the higher flux limiter predicts more shock heating and an earlier penetration of the heat front. The initial level of measured shock heating is higher than the simulation with $f = 0.1$; however, the timing of the heat-front penetration is similar.

Discussion

The experimental results indicate that the energy transport from the critical density to the ablation front cannot be described by flux-limited diffusion and may be nonlocal. The role of nonlocal thermal transport is twofold: (1) It results in an effective time-dependent flux limiter that influences the laser absorption fraction, the shock timing, and the shock-heated conditions. (2) It results in preheat through the transport of energetic electrons, which would increase the shell temperature. All of the experimental results presented in this article were compared with *LILAC* simulations having flux limiters of $f = 0.06$ and $f = 0.1$. The measurements are accurate enough to distinguish between these two models. In some cases the simulations with the higher flux limiter were closer to the experimental observables. A higher flux limiter was needed to reduce the discrepancies between the simulations and measurements for the early-time laser absorption, the mass ablation rate with laser irradiation of 1×10^{15} W/cm^2, and the shock heating with laser irradiation of 1×10^{15} W/cm^2. Preheat due to energetic electrons and x rays from the corona may explain shock heating at laser irradiation of 1×10^{15} W/cm^2. These observations are consistent with the effects of nonlocal electron thermal transport.[39] Other effects influencing the measurements also need to be investigated. The higher early-time laser absorption may be caused by resonance absorption,[54] which is not included in the *LILAC* prediction. *LILAC* may be underestimating the predicted electron temperature due to shock heating. The accuracy of modeling the electron temperature in the Al layer needs to be investigated. The simulations with the lower flux limiter of $f = 0.06$ were close to the measurements of shock heating at laser irradiation of 1×10^{14} W/cm^2. This could be consistent with a nonlocal electron thermal transport if the preheat is negligible at the lower intensity.

This detailed comparison of the results from the experiment and *LILAC* reveals the limitations of a flux-limited thermal-transport model for direct-drive ICF: a single-flux limiter cannot explain all the experimental observables. Laser absorption measurements indicate a time-dependent flux limiter is required. However, a nonlocal treatment of the thermal transport currently under development[39] is expected to improve agreement between the simulations and the experimental results.

Conclusion

An investigation of direct-drive energy coupling was conducted to tune the physics models of the 1-D hydrodynamics code *LILAC*. The flow of energy from the laser to the target was inferred by measuring the laser absorption fraction, the mass ablation rate, and the amount of shock heating. The highly reproducible experimental results achieved with a high level of laser drive uniformity constrain the modeling of direct-drive energy coupling. All of the experimental results were compared with *LILAC* simulations having flux limiters of $f = 0.06$ and $f = 0.1$. The detailed comparison reveals the limitation of a flux-limited thermal-transport model for direct-drive ICF: a single-flux limiter cannot explain all the experimental observables. Furthermore, simulations of laser absorption measurements need a time-dependent flux limiter to match the data. The experimental results indicate that the energy transport from the critical density to the ablation front is probably nonlocal. A nonlocal treatment of the thermal transport in *LILAC* is expected to improve the agreement between the simulations and the experimental results.

ACKNOWLEDGMENT

This work was supported by the U.S. Department of Energy Office of Inertial Confinement Fusion under Cooperative Agreement No. DE-FC52-92SF19460, the University of Rochester, and the New York State Energy Research and Development Authority. The support of DOE does not constitute an endorsement by DOE of the views expressed in this article.

REFERENCES

1. J. Nuckolls *et al*., Nature **239**, 139 (1972).
2. J. D. Lindl, R. L. McCrory, and E. M. Campbell, Phys. Today **45**, 32 (1992).
3. R. L. McCrory, J. M. Soures, C. P. Verdon, F. J. Marshall, S. A. Letzring, S. Skupsky, T. J. Kessler, R. L. Kremens, J. P. Knauer, H. Kim, J. Delettrez, R. L. Keck, and D. K. Bradley, Nature **335**, 225 (1988).
4. J. D. Lindl, *Inertial Confinement Fusion: The Quest for Ignition and Energy Gain Using Indirect Drive* (Springer-Verlag, New York, 1998).
5. S. E. Bodner, D. G. Colombant, J. H. Gardner, R. H. Lehmberg, S. P. Obenschain, L. Phillips, A. J. Schmitt, J. D. Sethian, R. L. McCrory, W. Seka, C. P. Verdon, J. P. Knauer, B. B. Afeyan, and H. T. Powell, Phys. Plasmas **5**, 1901 (1998).

6. P. W. McKenty, V. N. Goncharov, R. P. J. Town, S. Skupsky, R. Betti, and R. L. McCrory, Phys. Plasmas **8**, 2315 (2001).

7. J. D. Lindl *et al*., Phys. Plasmas **11**, 339 (2004).

8. P. W. McKenty, T. C. Sangster, M. Alexander, R. Betti, R. S. Craxton, J. A. Delettrez, L. Elasky, R. Epstein, A. Frank, V. Yu. Glebov, V. N. Goncharov, D. R. Harding, S. Jin, J. P. Knauer, R. L. Keck, S. J. Loucks, L. D. Lund, R. L. McCrory, F. J. Marshall, D. D. Meyerhofer, S. P. Regan, P. B. Radha, S. Roberts, W. Seka, S. Skupsky, V. A. Smalyuk, J. M. Soures, K. A. Thorp, M. Wozniak, J. A. Frenje, C. K. Li, R. D. Petrasso, F. H. Séguin, K. A. Fletcher, S. Padalino, C. Freeman, N. Izumi, J. A. Koch, R. A. Lerche, M. J. Moran, T. W. Phillips, G. J. Schmid, and C. Sorce, Phys. Plasmas **11**, 2790 (2004).

9. R. L. McCrory, S. P. Regan, S. J. Loucks, D. D. Meyerhofer, S. Skupsky, R. Betti, T. R. Boehly, R. S. Craxton, T. J. B. Collins, J. A. Delettrez, D. Edgell, R. Epstein, K. A. Fletcher, C. Freeman, J. A. Frenje, V. Yu. Glebov, V. N. Goncharov, D. R. Harding, I. V. Igumenshchev, R. L. Keck, J. D. Kilkenny, J. P. Knauer, C. K. Li, J. Marciante, J. A. Marozas, F. J. Marshall, A. V. Maximov, P. W. McKenty, J. Myatt, S. Padalino, R. D. Petrasso, P. B. Radha, T. C. Sangster, F. H. Séguin, W. Seka, V. A. Smalyuk, J. M. Soures, C. Stoeckl, B. Yaakobi, and J. D. Zuegel, Nucl. Fusion **45**, S283 (2005).

10. R. Betti, K. Anderson, T. R. Boehly, T. J. B. Collins, R. S. Craxton, J. A. Delettrez, D. H. Edgell, R. Epstein, V. Yu. Glebov, V. N. Goncharov, D. R. Harding, R. L. Keck, J. H. Kelly, J. P. Knauer, S. J. Loucks, J. A. Marozas, F. J. Marshall, A. V. Maximov, D. N. Maywar, R. L. McCrory, P. W. McKenty, D. D. Meyerhofer, J. Myatt, P. B. Radha, S. P. Regan, C. Ren, T. C. Sangster, W. Seka, S. Skupsky, A. A. Solodov, V. A. Smalyuk, J. M. Soures, C. Stoeck, W. Theobald, B. Yaakobi, C. Zhou, J. D. Zuegel, J. A. Frenje, C. K. Li, R. D. Petrasso, and F. H. Séguin, Plasma Phys. Control. Fusion **48**, B153 (2006).

11. M. C. Herrmann, M. Tabak, and J. D. Lindl, Nucl. Fusion **41**, 99 (2001).

12. R. Betti, K. Anderson, V. N. Goncharov, R. L. McCrory, D. D. Meyerhofer, S. Skupsky, and R. P. J. Town, Phys. Plasmas **9**, 2277 (2002).

13. T. R. Boehly, D. L. Brown, R. S. Craxton, R. L. Keck, J. P. Knauer, J. H. Kelly, T. J. Kessler, S. A. Kumpan, S. J. Loucks, S. A. Letzring, F. J. Marshall, R. L. McCrory, S. F. B. Morse, W. Seka, J. M. Soures, and C. P. Verdon, Opt. Commun. **133**, 495 (1997).

14. S. P. Regan, J. A. Marozas, R. S. Craxton, J. H. Kelly, W. R. Donaldson, P. A. Jaanimagi, D. Jacobs-Perkins, R. L. Keck, T. J. Kessler, D. D. Meyerhofer, T. C. Sangster, W. Seka, V. A. Smalyuk, S. Skupsky, and J. D. Zuegel, J. Opt. Soc. Am. B **22**, 998 (2005).

15. J. Delettrez, R. Epstein, M. C. Richardson, P. A. Jaanimagi, and B. L. Henke, Phys. Rev. A 36, 3926 (1987); J. Delettrez, Can. J. Phys. **64**, 932 (1986).

16. J. Paisner *et al*., Laser Focus World **30**, 75 (1994).

17. P. B. Radha, V. N. Goncharov, T. J. B. Collins, J. A. Delettrez, Y. Elbaz, V. Yu. Glebov, R. L. Keck, D. E. Keller, J. P. Knauer, J. A. Marozas, F. J. Marshall, P. W. McKenty, D. D. Meyerhofer, S. P. Regan, T. C. Sangster, D. Shvarts, S. Skupsky, Y. Srebro, R. P. J. Town, and C. Stoeckl, Phys. Plasmas **12**, 032702 (2005).

18. H. Takabe *et al*., Phys. Fluids **28**, 3676 (1985).

19. R. Betti, V. N. Goncharov, R. L. McCrory, and C. P. Verdon, Phys. Plasmas **5**, 1446 (1998).

20. S. P. Regan, J. A. Delettrez, V. N. Goncharov, F. J. Marshall, J. M. Soures, V. A. Smalyuk, P. B. Radha, B. Yaakobi, R. Epstein, V. Yu. Glebov, P. A. Jaanimagi, D. D. Meyerhofer, T. C. Sangster, W. Seka, S. Skupsky, C. Stoeckl, D. A. Haynes, Jr., J. A. Frenje, C. K. Li, R. D. Petrasso, and F. H. Séguin, Phys. Rev. Lett. **92**, 185002 (2004).

21. V. N. Goncharov, J. P. Knauer, P. W. McKenty, P. B. Radha, T. C. Sangster, S. Skupsky, R. Betti, R. L. McCrory, and D. D. Meyerhofer, Phys. Plasmas **10**, 1906 (2003).

22. K. Anderson and R. Betti, Phys. Plasmas **10**, 4448 (2003).

23. R. C. Malone, R. L. McCrory, and R. L. Morse, Phys. Rev. Lett. **34**, 721 (1975).

24. W. Seka, J.-L. Schwob, and C. Breton, J. Appl. Phys. **42**, 315 (1971).

25. F. C. Young *et al*., Appl. Phys. Lett. **30**, 45 (1977).

26. B. Yaakobi and T. C. Bristow, Phys. Rev. Lett. **38**, 350 (1977).

27. B. H. Ripin *et al*., Phys. Fluids **23**, 1012 (1980).

28. M. H. Key, R. G. Evans, and D. J. Nicholas, Rutherford Appleton Laboratory, Chilton, Didcot, Oxon, England, Report RL-78-020/XAB (1978).

29. B. Yaakobi, T. Boehly, P. Bourke, Y. Conturie, R. S. Craxton, J. Delettrez, J. M. Forsyth, R. D. Frankel, L. M. Goldman, R. L. McCrory, M. C. Richardson, W. Seka, D. Shvarts, and J. M. Soures, Opt. Commun. **39**, 175 (1981).

30. T. J. Goldsack *et al*., Opt. Commun. **42**, 55 (1982); T. J. Goldsack *et al*., Phys. Fluids **25**, 1634 (1982).

31. M. H. Key *et al*., Phys. Fluids **26**, 2011 (1983).

32. A. Hauer *et al*., Phys. Rev. Lett. **53**, 2563 (1984).

33. J. Delettrez, R. Epstein, M. C. Richardson, P. A. Jaanimagi, and B. L. Henke, Phys. Rev. A **36**, 3926 (1987).

34. D. K. Bradley, J. A. Delettrez, and C. P. Verdon, Phys. Rev. Lett. **68**, 2774 (1992).

35. D. J. Hoarty *et al*., J. Quant. Spectrosc. Radiat. Transf. **99**, 283 (2006).

36. T. R. Boehly, J. A. Delettrez, J. P. Knauer, D. D. Meyerhofer, B. Yaakobi, R. P. J. Town, and D. Hoarty, Phys. Rev. Lett. **87**, 145003 (2001).

37. H. Sawada, S. P. Regan, R. Epstein, D. Li, V. N. Gonchraov, P. B. Radha, D. D. Meyerhofer, T. R. Boehly, V. A. Smalyuk, T. C. Sangster, B. Yaakobi, and R. C. Mancini, "Investigation of Direct-Drive Shock Heating Using XRay Absorption Spectroscopy," to be submitted to Physics of Plasmas.

38. H. Sawada, S. P. Regan, D. D. Meyerhofer, I. V. Igumenshchev, V. N. Goncharov, T. R. Boehly, T. C. Sangster, V. A. Smalyuk, B, Yaakobi, G. Gregori, S. H. Glenzer, and O. L. Landen, "Diagnosing Direct-Drive, Shock-Heated Plastic Planar Foils with Noncollective Spectrally Resolved X-Ray Scattering," to be submitted to Physics of Plasmas.

39. V. N. Goncharov, O. V. Gotchev, E. Vianello, T. R. Boehly, J. P. Knauer, P. W. McKenty, P. B. Radha, S. P. Regan, T. C. Sangster, S. Skupsky, V. A. Smalyuk, R. Betti, R. L. McCrory, D. D. Meyerhofer, and C. Cherfils-Clérouin, Phys. Plasmas **13**, 012702 (2006).

40. A. R. Bell, R. G. Evans, and D. J. Nicholas, Phys. Rev. Lett. **46**, 243 (1981).

41. W. F. Huebner *et al*., Los Alamos National Laboratory, Los Alamos, NM, Report LA-6760-M (1977).

42. L. Spitzer, Jr. and R. Härm, Phys. Rev. **89**, 977 (1953).

43. A. Sunahara, J. A. Delettrez, C. Stoeckl, R. W. Short, and S. Skupsky, Phys. Rev. Lett. **91**, 095003 (2003).

44. W. Seka, L. M. Goldman, M. C. Richardson, J. M. Soures, K. Tanaka, B. Yaakobi, R. S. Craxton, R. L. McCrory, R. Short, E. A. Williams, T. Boehly, R. Keck, and R. Boni, in *Plasma Physics and Controlled Nuclear Fusion Research 1982* (IAEA, Vienna, 1983), Vol. I, pp. 131–137.

45. J. M. Soures, T. C. Bristow, H. Deckman, J. Delettrez, A. Entenberg, W. Friedman, J. Forsyth, Y. Gazit, G. Halpern, F. Kalk, S. Letzring, R. McCrory, D. Peiffer, J. Rizzo, W. Seka, S. Skupsky, E. Thorsos, B. Yaakobi, and T. Yamanaka, in *Laser Interaction and Related Plasma Phenomena*, edited by H. J. Schwarz, H. Hora, M. J. Lubin, and B. Yaakobi (Plenum Press, New York, 1981), Vol. 5, pp. 463–481.

46. W. Seka, R. S. Craxton, J. Delettrez, L. Goldman, R. Keck, R. L. McCrory, D. Shvarts, J. M. Soures, and R. Boni, Opt. Commun. **40**, 437 (1982).

47. M. C. Richardson, R. S. Craxton, J. Delettrez, R. L. Keck, R. L. McCrory, W. Seka, and J. M. Soures, Phys. Rev. Lett. **54**, 1656 (1985).

48. W. Seka, V. N. Goncharov, J. A. Delettrez, D. H. Edgell, I. V. Igumenshchev, R. W. Short, A. V. Maximov, J. Myatt, and R. S. Craxton, "Time-Dependent Absorption Measurements in Direct-Drive Spherical Implosions," to be submitted to Physics of Plasmas.

49. S. P. Regan, D. K. Bradley, A. V. Chirokikh, R. S. Craxton, D. D. Meyerhofer, W. Seka, R. W. Short, A. Simon, R. P. J. Town, B. Yaakobi, J. J. Caroll III, and R. P. Drake, Phys. Plasmas **6**, 2072 (1999).

50. T. R. Boehly, E. Vianello, J. E. Miller, R. S. Craxton, T. J. B. Collins, V. N. Goncharov, I. V. Igumenshchev, D. D. Meyerhofer, D. G. Hicks, P. M. Celliers, and G. W. Collins, Phys. Plasmas **13**, 056303 (2006).

51. D. H. Kalantar *et al*., in *22nd International Congress on High-Speed Photography and Photonics*, edited by D. L. Paisley and A. M. Frank (SPIE, Bellingham, WA, 1997), Vol. 2869, pp. 680–685.

52. Prism Computational Sciences, Inc., Madison, WI 53711.

53. O. Gotchev, V. N. Goncharov, J. P. Knauer, T. R. Boehly, T. J. B. Collins, R. Epstein, P. A. Jaanimagi, and D. D. Meyerhofer, Phys. Rev. Lett. **96**, 115005 (2006).

54. W. L. Kruer, *The Physics of Laser–Plasma Interactions, Frontiers in Physics*, Vol. 73, edited by D. Pines (Addison-Wesley, Redwood City, CA, 1988).

Nuclear Measurements of Fuel–Shell Mix in Inertial Confinement Fusion Implosions on OMEGA

Introduction

Turbulent mix is a vital concern in inertial confinement fusion (ICF)[1,2] since it can quench the nuclear burn in the hot spot prematurely, or even extinguish it entirely. The saturation of Rayleigh–Taylor (RT) instability growth at a density interface leads to small-scale, turbulent eddies that in turn lead to mixing of the high- and low-density materials.[3] These mixing processes can disrupt the formation of the low-density hot spot, lowering its temperature and reducing its volume. The resulting lower nuclear production can fail to ignite the capsule. Understanding the extent of mix under different conditions is a crucial step toward mitigating its adverse effects.

A substantial and sustained effort to understand hydrodynamic instabilities and mix has been ongoing for many decades, due in large part to their heavy impact on ICF. Reviews of the literature on experimental, computational, and theoretical work on hydrodynamic instabilities and mix can be found on, for example, the first page of Refs. 4 and 5. Related work on mix in ICF implosions includes papers by Li,[6] Radha,[7] Regan,[8] and Wilson,[9] as well as many others.

This article reviews and extends aspects of the work published by Li *et al.*[6] over a wider range of capsule parameters. In addition, we calculate a quantitative upper limit on the null result published by Petrasso *et al.*[10] of the amount of mix at the time of shock collapse, which occurs before the onset of the deceleration phase. Results from time-dependent nuclear production history measurements of the mix region will be published elsewhere.[11] A brief review of the causes and effects of mix can be found in the next section. The remaining sections (1) describe the experimental setup, (2) present experimental observations, (3) describe the constraint on the amount of fuel–shell mix between shock collapse and deceleration-phase onset, and (4) summarize our results.

Causes and Effects of Mix

When a fluid of density ρ_1 accelerates a heavier fluid of density ρ_2, the fluid interface is RT unstable. The rapid growth of initial perturbations sends spikes of the heavy fluid into the light fluid, while bubbles of the light fluid penetrate into the heavy fluid. The exponential growth eventually saturates into a nonlinear regime where the spike and bubble amplitudes grow quadratically in time. As the spikes and bubbles continue to interpenetrate, velocity shear between the two fluids results in further instability (the drag-driven Kelvin–Helmholtz instability), causing the spike tips to "mushroom" and roll up on increasingly finer scales, increasing the vorticity of the flow and eventually leading to mixing of the two fluids on the atomic scale.

In ICF, both the acceleration and deceleration phases have RT-unstable surfaces.[2] The low-density ablating mass pushes against the high-density "payload" during the acceleration phase, and after further convergence and compression, the high-density shell is stopped by the low-density hot spot during the deceleration phase. Initial perturbations are seeded by laser and target surface nonuniformities, and growth of these perturbations during the acceleration phase can feed through to the inner surface and contribute to seeding perturbations for the deceleration phase.[2]

Unmitigated RT growth during the acceleration phase can eventually break through the shell, compromising its compressibility and reducing the attainable areal density of the assembled target at stagnation. RT growth during the deceleration phase can send spikes of cold, dense fuel into the central hot spot, potentially disrupting its formation. Even if the spikes do not reach the center, their penetration and the resultant mixing of the cold, dense shell with the low-density hot spot will cool the outer regions of the hot spot, reducing the volume participating in nuclear production.

Experimental Setup

Direct-drive implosions were conducted on OMEGA,[12] with 60 beams of frequency-tripled (351 nm) UV light in a 1-ns square pulse and a total energy of 23 kJ. One-THz-bandwidth smoothing by spectral dispersion and polarization smoothing of the laser beam were used.[13] The beam-to-beam energy imbalance was typically between 2% and 4% rms. The spherical capsules had diameters between 860 and 940 μm, plastic-shell thicknesses of 20, 24, or 27 μm, and a surface coating of 0.1 μm of aluminum.

Three target configurations were used (Fig. 109.14): The reference "CH" capsules had shells made of plastic (CH) and a gaseous fill of D_2 and ^{3}He. "CD" capsules had gaseous fills of pure ^{3}He, and a shell made mostly of CH, except for a 1-μm layer of deuterated plastic (CD) on the inner surface. "CD offset" capsules are like the CD capsules, except that the 1-μm CD layer is offset from the inner surface by 1 μm of CH. The composition of the ordinary plastic consists of an H to C ratio of 1.38, and the deuterated plastic has a D to C ratio of 1.56 (Ref. 6).

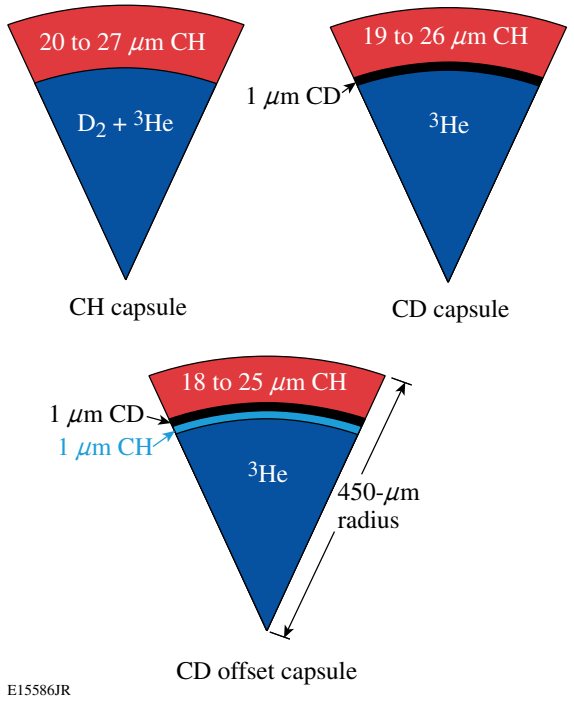

Figure 109.14
0.5 or 2.5 mg/cm^3 of pure ^{3}He gas fills a 20- to 27-μm-thick plastic shell with a 1-μm deuterated layer either adjacent to the inner surface (CD capsule) or offset from the inner surface by 1 μm (CD offset capsule). The reference (CH capsule) contains D^{3}He gas and has no deuterated layer. Whereas CH capsules will produce D^{3}He protons whenever the fuel gets sufficiently hot, CD capsules will produce only D^{3}He protons if the fuel and shell become atomically mixed.

The pure ^{3}He gases were filled to initial pressures of 4 and 20 atm at a temperature of 293 K, corresponding to initial mass densities (ρ_0) of 0.5 and 2.5 mg/cm^3. The D_2–^{3}He gas is an equimolar mixture of D to ^{3}He by atom and is filled to a hydrodynamically equivalent initial pressure as the pure-^{3}He fill, as described in Ref. 14. Because fully ionized D and ^{3}He have the same value of $(1 + Z)/A$, mixtures with the same mass density will also have the same total particle density and equation of state and can be considered hydrodynamically equivalent. For the 4- and 20-atm ^{3}He fills, the hydrodynamically equivalent D_2–^{3}He pressures are 3.6 and 18 atm, respectively.

Hydrodynamic simulations of capsule implosions using the 1-D code *LILAC*[15] showed only minor differences in the timing and profiles between the equivalent CH and CD implosions. The convergence ratio C_r, defined as the initial inner capsule radius over the fuel–shell interface radius at the time of stagnation, for capsules with different shell thicknesses and initial fill density is shown in Table 109.I.

Table 109.I: Predicted convergence ratio C_r calculated by *LILAC* for different capsule parameters. Capsules with higher convergence ratios are expected to be more susceptible to mix. The convergence ratio does not differ significantly between CH and CD capsules.

ρ_0 (mg/cm^3)	Thickness (μm)	C_r (1-D)
0.5	20	38.0
0.5	24	35.2
0.5	27	31.5
2.5	20	14.9
2.5	24	14.5
2.5	27	13.8

The following primary nuclear reactions can occur in targets containing both D_2 and ^{3}He:

$$\begin{aligned} \mathrm{D} + \mathrm{D} &\rightarrow {}^3\mathrm{He} + n(2.45\ \mathrm{MeV}), \\ \mathrm{D} + \mathrm{D} &\rightarrow \mathrm{T} + p(3.0\ \mathrm{MeV}), \\ \mathrm{D} + {}^3\mathrm{He} &\rightarrow {}^4\mathrm{He} + p(14.7\ \mathrm{MeV}), \end{aligned} \tag{1}$$

where the number in parentheses is the mean birth energy of the second product.

The set of capsules shown in Fig. 109.14 is ideal for studying the nature and extent of turbulent mix in ICF implosions. Whereas implosions of CH capsules will produce D^{3}He protons whenever the fuel gas gets sufficiently hot, heating alone is not sufficient for D^{3}He production in CD and CD offset capsules. To produce measurable D^{3}He yields, these capsules require in addition the mixing of the fuel and shell on an atomic scale. Measurement or absence of the D^{3}He yield in implosions of CD offset capsules can be used to ascertain the extent into the shell that turbulent mixing processes reach.

Fuel–shell mix is not a requirement to produce DD-n yields in CD and CD offset implosions, but measurement of the DD-n yield provides a useful way to determine if the CD layer was heated to temperatures near 1 keV.

The primary diagnostics for this study were wedged-range-filter (WRF) spectrometers,[16] to measure the D^3He proton yield and spectrum, and neutron time-of-flight (nTOF) scintillator detectors,[17] to measure the DD-*n* yield. On a given shot, up to six WRF spectrometers were used simultaneously to improve the estimate of the D^3He yield.[16] The D^3He proton spectrum measured from implosions of D^3He-filled CH capsules often shows two distinct components, corresponding to D^3He proton emission shortly after the collapse of the converging shock and to emission during the deceleration phase, about 300 ps later.[10,18]

Experimental Results

1. Yield Measurements

Turbulent mixing of the fuel and shell is demonstrated by measurements of finite D^3He yields (Y_p) in ^3He-filled, CD capsules (see Fig. 109.15 and Ref. 6). The shock component, apparent in the spectrum of the CH capsule implosion above 14 MeV, is absent in the CD capsule. All D^3He yields reported in this section for CH capsules will include only the compression component; the shock component will be considered in the following section.

The D^3He yields from CD capsules are at least two orders of magnitude higher than would be expected by the interaction of thermal ^3He ions penetrating through the CD layer surface,[6] even with enhanced surface area resulting from a RT-perturbed surface. The D^3He yields are at least three orders of magnitude higher than the maximum that would be expected if some ^3He had diffused into the CD layer between the times of fabrication and implosion.[6] For yields as high as have been observed, there must be a region that has been heated to at least 1 keV and where the fuel and shell have experienced atomic mix.

Significant D^3He yield from CD-offset implosions demonstrates that there is substantial mixing of the fuel with the "second" 1-μm layer of the shell (Fig. 109.16). Thermal ^3He ions cannot penetrate through the first micron of the shell to produce

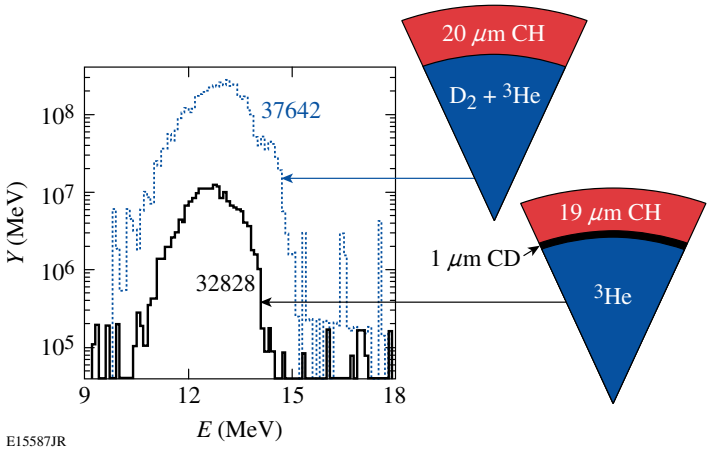

Figure 109.15
D^3He proton spectra from a CH capsule (shot 37642) and from a CD capsule (shot 32828) with 2.5-mg/cm^3 initial fill density. The high D^3He yield from CD implosions demonstrates the existence of fuel–shell mix. The CD implosion yield, although substantially less than the yield from the CH implosion, is much higher than what would be expected in the absence of turbulent fuel–shell mix.

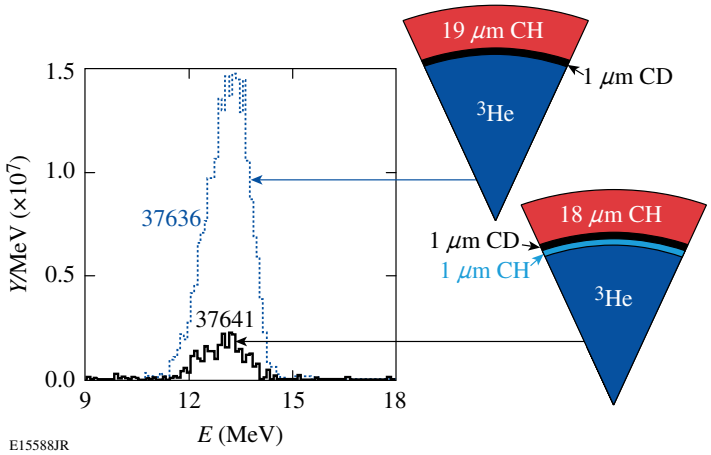

Figure 109.16
D^3He proton spectra from a CD capsule (shot 37636) and from a CD offset capsule (shot 37641) with 0.5-mg/cm^3 initial fill density. The D^3He yield drops by only a factor of 5 to 10 when the CD layer is offset from the inner surface by 1 μm, demonstrating that a substantial amount of the second micron of the shell is mixed with the fuel.

these yields, so the second micron must be exposed to the fuel by bubble growth and then mixed through turbulent processes.

The decreasing yields for increasing ρ_0 in CD capsules contrast strongly with the increasing yields for increasing initial ρ_0 in the reference CH capsules (see Fig. 109.17). This is evidence that the extent of mix is reduced for increasing initial fill density, since Y_p in CD implosions is lower, even though the core conditions are more favorable for nuclear production, as seen by the higher value of Y_p for CH implosions. Y_p in CD-offset implosions decreases by an additional factor of 5 and 10 compared to inner CD capsule implosions for 0.5 and 2.5 mg/cm^3 fills, respectively.

The lower DD-*n* yield (Y_n) for CD implosions with higher ρ_0 indicates that less heating of the CD layer occurred in these implosions. Additional heating of the inner surface of the shell can occur through thermal conduction from and turbulent mix with the hot fuel. The lower Y_n supports the picture of reduced mix for higher-density fills.

Yields in both CH and CD implosions decrease with increasing shell thickness (Fig. 109.18). Thicker shells decrease Y_p by a larger factor in CD capsules compared to CH capsules, which suggests that the effects of mix are diminished. However, Y_n decreases by a smaller factor in CD capsules, which may be due to temperature effects dominating mix effects for the neutron yield in such implosions.

2. Areal Density Measurements

Evidence for a delay in nuclear production can be found through measurement of the compression of the target at bang time by

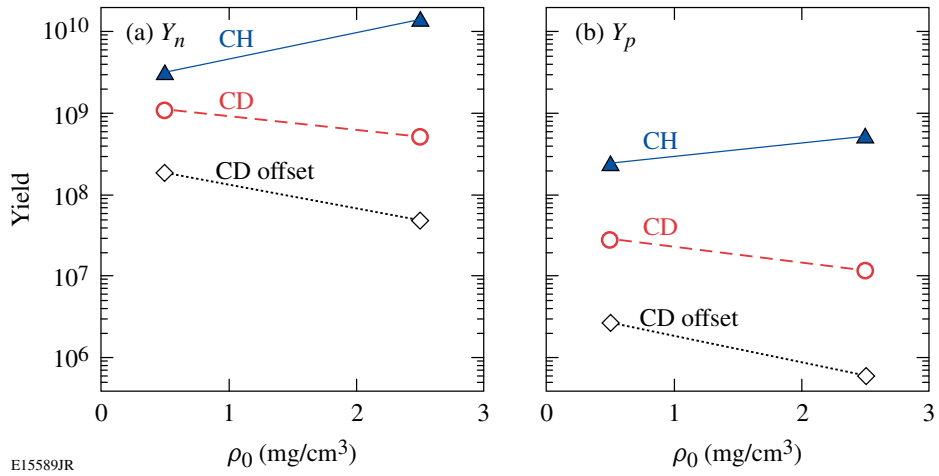

Figure 109.17
(a) DD-*n* and (b) D^{3}He yields from CH (solid triangles), CD (open circles), and CD-offset (open diamonds) implosions as a function of initial fill density for 20-μm-thick shells. Yields from CD and CD-offset implosions decrease with increasing fill density, in contrast to the increasing yields from CH implosions. Points show the mean of each shot ensemble, where the standard error in the mean is smaller than the size of the markers.

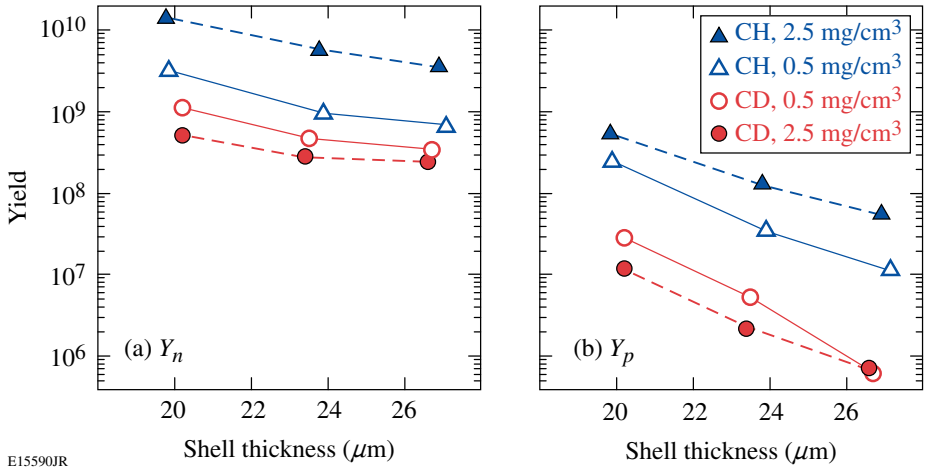

Figure 109.18
(a) DD-*n* and (b) D^{3}He yield in CH (triangles) and CD (circles) capsules with low (open markers) and high (solid markers) ρ_0 as a function of shell thickness. Capsules with lower ρ_0 are more susceptible to mix for all shell thicknesses.

means of the areal density ρR. Areal density is inferred from the mean downshift of the D^3He proton spectrum from the birth energy of 14.7 MeV, so the inferred ρR is an average measurement of ρR over the time of nuclear production. Because the capsule continues to compress, and ρR to increase, throughout the deceleration phase, one would expect that if bang time occurs during a later stage of the deceleration phase for an otherwise equivalent implosion, then the average ρR would be higher.[11,18] As seen in Fig. 109.19, the inferred burn-averaged ρR is higher for implosions of CD capsules than for CH capsules. This is qualitatively consistent with the later bang times measured for CD capsules.

The experimental results of these experiments are summarized in Table 109.II. The mean and standard error are shown of

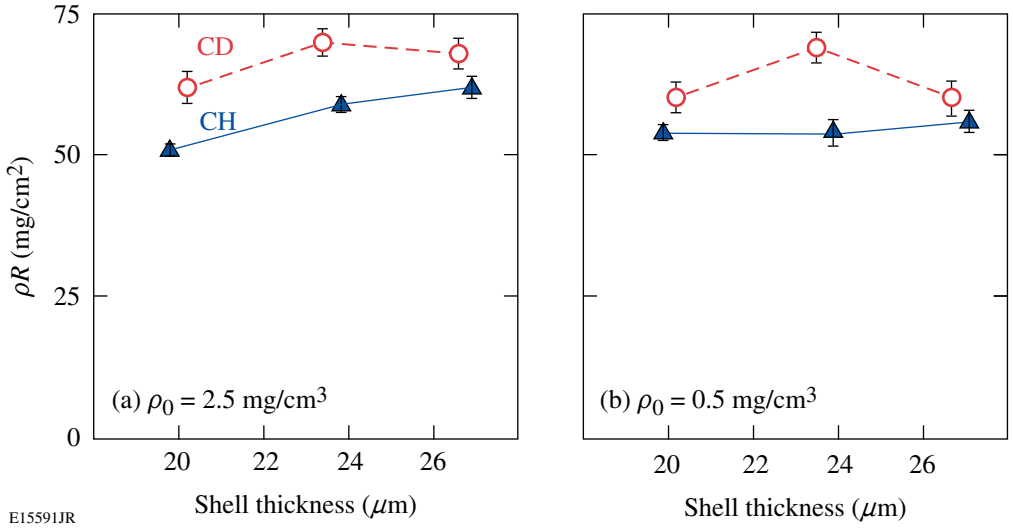

Figure 109.19
Mean and standard error of ρR's for CH (solid markers) and CD (open markers) implosions as a function of shell thickness with (a) high- and (b) low-density fills. The D^3He burn-averaged ρR is consistently higher for CD capsules.

Table 109.II: Experimental yield and areal density results of CH, CD, and CD-offset capsule implosions. The values shown are the mean and standard error of all shots in a particular ensemble, with the yield errors expressed as a percent of the mean. The quoted D^3He yield and areal density for CH capsules include the compression component only.

Type	ρ_0 (mg/cm^3)	Thickness (μm)	Number of shots	Y_n ($\times 10^8$)	Error (%)	Y_p ($\times 10^7$)	Error (%)	ρR (mg/cm^2)	Error
CH	0.5	19.9	17	31.3	6	24.3	11	54	1.5
CH	0.5	23.9	9	9.6	6	3.5	12	54	2.3
CH	0.5	27.1	8	6.7	7	1.13	30	56	2.0
CH	2.5	19.8	61	142	4	54.4	5	51	1.0
CH	2.5	23.8	26	58	5	13.2	8	59	1.3
CH	2.5	26.9	16	35	5	5.6	8	62	2.0
CD	0.5	20.2	7	10.8	10	2.9	10	60	2.4
CD	0.5	23.5	5	4.7	7	0.54	9	69	2.6
CD	0.5	26.7	2	3.4	7	0.06	7	60	3.1
CD	2.5	20.2	11	5.2	8	1.25	13	62	2.8
CD	2.5	23.4	7	2.7	15	0.22	19	70	2.4
CD	2.5	26.6	4	2.4	5	0.07	4	68	2.7
CD-off	0.5	19.2	3	1.9	17	0.28	28	52	1.7
CD-off	0.5	23.7	2	1.2	14	–	–	–	–
CD-off	2.5	18.4	5	0.5	24	0.06	14	55	3.0
CD-off	2.5	22.8	3	1.2	49	–	–	–	–

the DD-*n* and D^3He yields (Y_n and Y_p) and the areal density ρR inferred from the mean downshift of 14.7-MeV D^3He protons for CH, CD, and CD-offset capsules. Also shown is the number of shots of each kind. The mean is the average of measured values within a given shot ensemble, and the standard error is the standard deviation of the measurements divided by the square root of the number of shots.

Constraint on the Possibility of Mix During the Coasting Phase

Comparative analysis of D^3He-*p* spectra from CH and CD implosions can be used to place an upper bound on the possible amount of mix at shock time. For the representative spectrum of a CH capsule shown in Fig. 109.20, the total yield in the region from 14.2 to 14.7 MeV, corresponding to the shock component, is $1.7\pm0.2\times10^7$, or 3.7±0.3% of the total yield. The yield in the same region of the representative spectrum from a CD capsule comes to $2.6\pm2.5\times10^4$, equal to 0.14±0.13% of the total yield, and is consistent with zero.

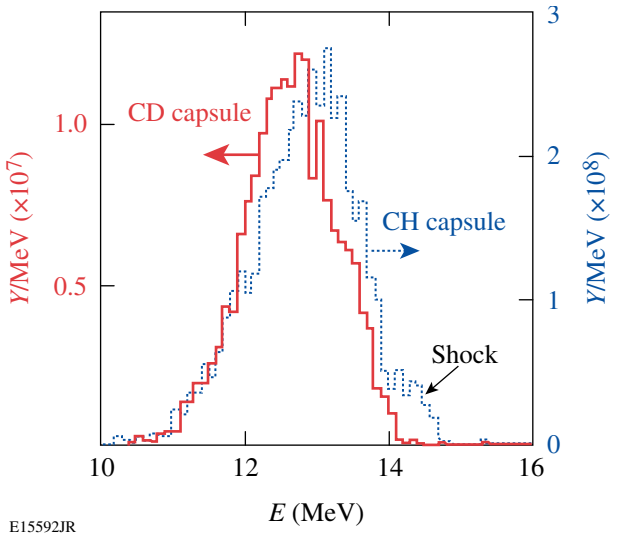

Figure 109.20
D^3He proton spectra from implosions of 20-μm-thick shells filled with 2.5 mg/cm^3 of fuel with CH (shot 37642, dotted) and CD (shot 32828, solid) shell configurations. The shock component of the CH implosions comes to 3.7% of the total yield, whereas the shock component contribution to the CD implosion spectrum is consistent with zero.

The "shock yield" of the CD implosion ($\le2.6\times10^4$) comes to, at most, 0.15% of the shock yield of the corresponding CH implosion (1.7×10^7). This yield ratio can be used to constrain the deuterium fraction by atom $f_D \le 0.05\%$ in the fuel of the CD implosion during shock burn, by application of Eq. (5) in Ref. 14. Equation (5) assumes that f_D is uniform through the fuel region, so it does not preclude the more likely physical situation of deuterium concentrations higher than the above constraint in the outer, cooler region of the fuel.

Summary

The extent of fuel–shell mix has been shown to include a substantial amount of the shell from the inner first and second micron of the original material using ^3He-filled, CD-shell target implosions. The observed yields are higher than is consistent with diffusive mixing, so they must be the result of turbulent mixing down to the atomic scale.

The improved stability of capsules with higher initial fuel density and thicker initial shells has been confirmed by comparing the yield trends of CH, CD, and CD-offset capsules. Increasing the capsule fill density decreased the D^3He and DD-*n* yields for CD capsules and increased the yields for CH capsules, thereby demonstrating that the extent of mix is reduced for increasing initial fill density.

The D^3He shock yield in CD capsules with high initial fill density was constrained to be less than 0.14% of the total D^3He yield, and the average atomic fraction of deuterium in the fuel during the shock burn has been constrained to be less than 0.05% and is consistent with zero.

ACKNOWLEDGMENT

The authors express their gratitude to the OMEGA engineers and operations crew who supported these experiments. This work was supported in part by the U.S. Department of Energy Office of Inertial Confinement Fusion (Grant No. DE-FG03-03NA00058), by the Lawrence Livermore National Laboratory (Subcontract No. B543881), by the Fusion Science Center for Extreme States of Matter and Fast Ignition (Contract No. 412761-G), and by the Laboratory for Laser Energetics (Subcontract No. 412160-001G) under Cooperative Agreement DE-FC52-92SF19460, University of Rochester, and New York State Energy Research and Development Authority.

REFERENCES

1. J. Nuckolls *et al.*, Nature **239**, 139 (1972).
2. S. Atzeni and J. Meyer-ter-Vehn, *The Physics of Inertial Fusion: Beam Plasma Interaction, Hydrodynamics, Hot Dense Matter, International Series of Monographs on Physics* (Clarendon Press, Oxford, 2004).
3. P. E. Dimotakis, Annu. Rev. Fluid Mech. **37**, 329 (2005).
4. G. Dimonte, Phys. Plasmas **6**, 2009 (1999).
5. A. J. Scannapieco and B. Cheng, Phys. Lett. A **299**, 49 (2002).
6. C. K. Li, F. H. Séguin, J. A. Frenje, S. Kurebayashi, R. D. Petrasso, D. D. Meyerhofer, J. M. Soures, J. A. Delettrez, V. Yu. Glebov, P. B. Radha, F. J. Marshall, S. P. Regan, S. Roberts, T. C. Sangster, and C. Stoeckl, Phys. Rev. Lett. **89**, 165002 (2002).

7. P. B. Radha, J. Delettrez, R. Epstein, V. Yu. Glebov, R. Keck, R. L. McCrory, P. McKenty, D. D. Meyerhofer, F. Marshall, S. P. Regan, S. Roberts, T. C. Sangster, W. Seka, S. Skupsky, V. Smalyuk, C. Sorce, C. Stoeckl, J. Soures, R. P. J. Town, B. Yaakobi, J. Frenje, C. K. Li, R. Petrasso, F. Séguin, K. Fletcher, S. Padalino, C. Freeman, N. Izumi, R. Lerche, and T. W. Phillips, Phys. Plasmas **9**, 2208 (2002).

8. S. P. Regan, J. A. Delettrez, F. J. Marshall, J. M. Soures, V. A. Smalyuk, B. Yaakobi, V. Yu. Glebov, P. A. Jaanimagi, D. D. Meyerhofer, P. B. Radha, W. Seka, S. Skupsky, C. Stoeckl, R. P. J. Town, D. A. Haynes, Jr., I. E. Golovkin, C. F. Hooper, Jr., J. A. Frenje, C. K. Li, R. D. Petrasso, and F. H. Séguin, Phys. Rev. Lett. **89**, 085003 (2002).

9. D. C. Wilson, C. W. Cranfill, C. Christensen, R. A. Forster, R. R. Peterson, H. M. Hoffman, G. D. Pollak, C. K. Li, F. H. Séguin, J. A. Frenje, R. D. Petrasso, P. W. McKenty, F. J. Marshall, V. Yu. Glebov, C. Stoeckl, G. J. Schmid, N. Izumi, and P. Amendt, Phys. Plasmas **11**, 2723 (2004).

10. R. D. Petrasso, J. A. Frenje, C. K. Li, F. H. Séguin, J. R. Rygg, B. E. Schwartz, S. Kurebayashi, P. B. Radha, C. Stoeckl, J. M. Soures, J. Delettrez, V. Yu. Glebov, D. D. Meyerhofer, and T. C. Sangster, Phys. Rev. Lett. **90**, 095002 (2003).

11. J. R. Rygg, J. A. Frenje, C. K. Li, F. H. Séguin, R. D. Petrasso, V. Yu. Glebov, D. D. Meyerhofer, T. C. Sangster, and C. Stoeckl, "Time-Dependent Nuclear-Measurements of Fuel–Shell Mix in Inertial Confinement Fusion," submitted to Physical Review Letters.

12. T. R. Boehly, D. L. Brown, R. S. Craxton, R. L. Keck, J. P. Knauer, J. H. Kelly, T. J. Kessler, S. A. Kumpan, S. J. Loucks, S. A. Letzring, F. J. Marshall, R. L. McCrory, S. F. B. Morse, W. Seka, J. M. Soures, and C. P. Verdon, Opt. Commun. **133**, 495 (1997).

13. S. Skupsky and R. S. Craxton, Phys. Plasmas **6**, 2157 (1999).

14. J. R. Rygg, J. A. Frenje, C. K. Li, F. H. Séguin, R. D. Petrasso, J. A. Delettrez, V. Yu. Glebov, V. N. Goncharov, D. D. Meyerhofer, S. P. Regan, T. C. Sangster, and C. Stoeckl, Phys. Plasmas **13**, 052702 (2006).

15. J. Delettrez, R. Epstein, M. C. Richardson, P. A. Jaanimagi, and B. L. Henke, Phys. Rev. A **36**, 3926 (1987).

16. F. H. Séguin, J. A. Frenje, C. K. Li, D. G. Hicks, S. Kurebayashi, J. R. Rygg, B.-E. Schwartz, R. D. Petrasso, S. Roberts, J. M. Soures, D. D. Meyerhofer, T. C. Sangster, J. P. Knauer, C. Sorce, V. Yu. Glebov, C. Stoeckl, T. W. Phillips, R. J. Leeper, K. Fletcher, and S. Padalino, Rev. Sci. Instrum. **74**, 975 (2003).

17. R. A. Lerche and T. J. Murphy, Rev. Sci. Instrum. **63**, 4880 (1992).

18. J. A. Frenje, C. K. Li, F. H. Séguin, J. Deciantis, S. Kurebayashi, J. R. Rygg, R. D. Petrasso, J. Delettrez, V. Yu. Glebov, C. Stoeckl, F. J. Marshall, D. D. Meyerhofer, T. C. Sangster, V. A. Smalyuk, and J. M. Soures, Phys. Plasmas **11**, 2798 (2004).

Measured Magnetic-Field Evolution and Instabilities in Laser-Produced Plasmas

The stability of plasmas with magnetic (B) fields is a critical issue for basic and applied plasma physics; instabilities may lead to important (and sometimes catastrophic) changes in plasma dynamics.[1] Intensive studies of various instabilities have been conducted for a wide range of plasmas and fields, particularly in the areas of magnetic-confinement plasmas[2] and space physics.[3] In laser-produced, high-energy-density (HED) laboratory plasmas, however, experimental studies of B-field–related instabilities have been rare because of limitations in experimental methods. In particular, resistive instabilities, a large category of macroscopic instabilities, have not been observed previously in this regime, partly because they are not important in the hot, low-resistivity plasmas usually studied.[4]

In the experiments described here, monoenergetic proton radiography was used for the first time to study the time evolution of the B-field structure that is generated by the interaction of a long-pulse, low-intensity laser beam with plasma. This work focuses on the qualitative and quantitative study of the physics involved in field evolution and instabilities over a time interval much longer than the laser pulse length, and B fields generated by laser–plasma interactions experience a tremendous dynamic range of plasma conditions. While the laser is on, we study field generation (via $\nabla n_e \times \nabla T_e$),[4–6] growth, and the balance between energy input and losses. After the laser turns off, laser absorption at the critical surface ends and the plasma cools down. Fields start to decay and dissipate, and field diffusion [$\nabla \times (D_m \nabla \times \mathbf{B})$, where D_m is the magnetic diffusion coefficient[4–6]] becomes increasingly important relative to convection [$\nabla \times (\mathbf{v} \times \mathbf{B})$, where $\mathbf{v}$ is the plasma fluid velocity[4–6]] as the cooling plasma becomes more resistive. At these later times, physical processes associated with resistivity tend to dominate over fluid effects, particularly around the bubble edge where the plasma β values, a ratio of thermal to field energies, are smaller than one.

The approach described here allows us to make a direct comparison of proton images recorded at different times, to measure field evolution, to address different physics processes in different regimes, and, most importantly, to identify resistivity-induced instabilities. Most previous work in this field has involved high-intensity, short-pulse lasers[7] or long-pulse lasers with limited diagnostic measurements.[8] Preliminary measurements we made while a laser beam was on have recently been published,[9] but the work described here uniquely covers times extending well past the end of the laser pulse and reveals important new phenomena that were not previously seen and are not predicted by two-dimenstional (2-D) simulation codes. The first observation of repeatable, asymmetric structure around the plasma bubbles at late times provides important insights into pressure-driven magnetohydrodynamic (MHD) instabilities in resistive plasmas,[2] while the first observation of nonrepeatable chaotic structure within the plasma bubble provides likely evidence of the electron thermal instability.[10] Simulations[11] of these experiments with the 2-D hydrodynamic code *LASNEX*[12,13] and hybrid PIC code *LSP*[14] have been performed; they are qualitatively useful for interpreting the observations but diverge from our measurements (particularly after the laser beam is off).

The setup of the experiments performed on OMEGA[15] is illustrated schematically in Fig. 109.21. B fields were generated through laser–plasma interactions on a plastic (CH) foil by a single laser beam (henceforth called the *interaction beam*) with a wavelength of 0.351 μm, incident 23° from the normal

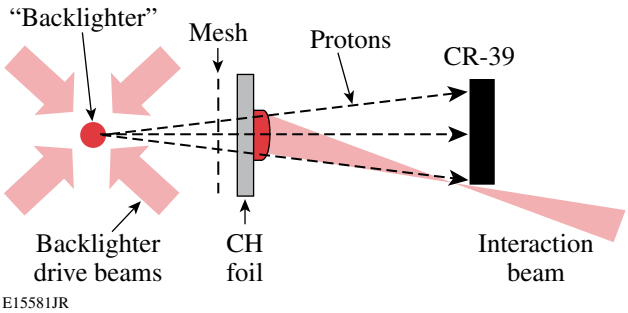

Figure 109.21
Schematic illustration of the experimental setup for face-on proton radiography. Distances from the backlighter are 1.3 cm for the mesh, 1.5 cm for the CH foil (5 μm thick), and 30 cm for the CR-39 detector.

direction. The laser had a 1-ns-long square pulse, an energy of ~500 J, and a spot diameter of 800 μm determined by phase plate SG4 (defined as 95% energy deposition),[16] resulting in a laser intensity of the order of 10^{14} W/cm^2.

The fields were studied with monoenergetic proton radiography, using a backlighter that produced protons at the two discrete energies of 14.7 MeV and 3 MeV (fusion products of the nuclear reactions D + ^{3}He → α + p and D + D → T + p, respectively, generated from D^{3}He-filled, exploding-pusher implosions driven by 20 OMEGA laser beams).[9,17] The duration of the backlighter was ~150 ps, and the timing of the interaction laser was adjusted in different experiments so the arrival of the backlighter protons at the foil would occur with different delays after the laser interaction beam was turned on. Separate radiographs made with the two proton energies were recorded simultaneously using stacked CR-39 detectors arranged with filters so that only one detector was sensitive to each energy.[18] A nickel mesh (60 μm thick with a 150-μm hole-to-hole spacing) was used to divide the backlighter protons into discrete beamlets, and, for the 14.7-MeV protons, the deflections of these beamlets due to fields in laser-induced plasmas on CH foils were measured in the images.

Images made with these monoenergetic-proton backlighters have distinct advantages over images made with broadband sources: measured image dimensions and proton beamlets deflections provide unambiguous quantitative information about fields; detectors can be optimized; and the backlighter is isotropic (simultaneous measurements can be made in multiple directions[17] and the source can be monitored at any angle).

Face-on images made with D^{3}He protons are shown in Fig. 109.22(a). The laser timing was adjusted so that these 14.7-MeV protons arrived at the foil at various times between 0.3 ns and 3 ns after the laser interaction beam was turned on. Since the interaction-beam pulse was 1 ns square with ~0.1-ns rise and decay times, the data covered two time intervals: 0.3 to 0.9 ns when the laser was on, and 1.2 to 3 ns when the laser was off. Each image shows how the proton beamlets are deflected while passing through the magnetic field that formed around the plasma bubble generated by the interaction beam, as described previously.[9,11,17]

While the interaction beam is on, each image has a sharp circular ring where beamlets pile up after passing through the edges of the plasma bubble where the maximum B fields were generated. The deflection of each beamlet is proportional to the integral $\left| \int \mathbf{B} \times d\ell \right|$ (where $d\ell$ is the differential pathlength along the proton trajectory), and this integral is highest at the edge of the bubble. Beamlets in the center of each image undergo less radial deflection, indicating that the integral $\left| \int \mathbf{B} \times d\ell \right|$ is much smaller there. These features are well reproduced by *LASNEX + LSP* simulations, as shown in Fig. 109.22(b) (0.3 to 0.9 ns). Figure 109.23(a) shows the

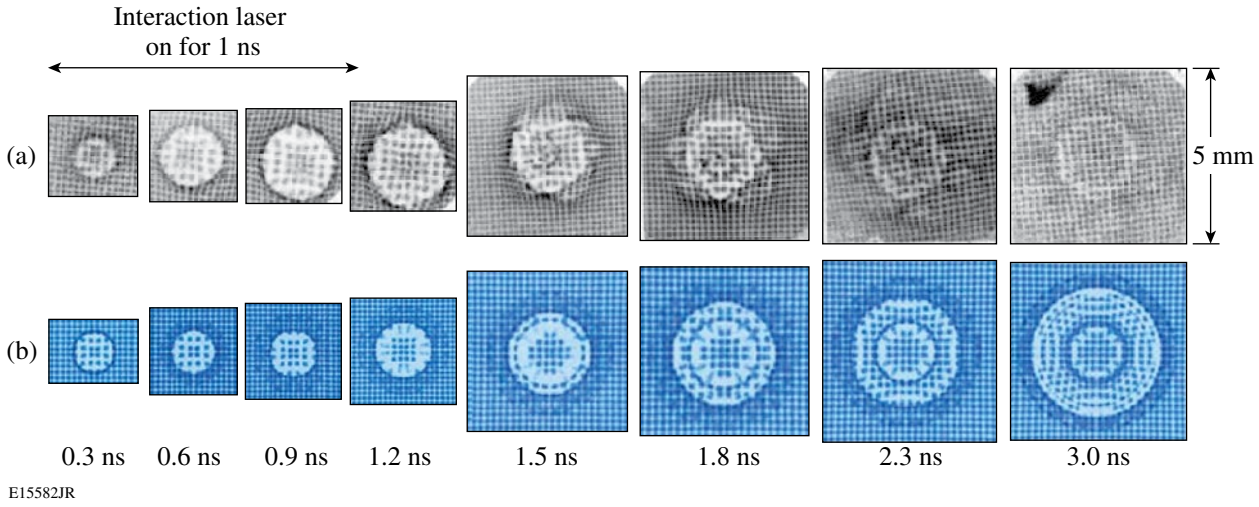

Figure 109.22
(a) Measured face-on D^{3}He proton images showing the spatial structure and temporal evolution of the B fields generated by laser–plasma interactions. Each image is labeled by the time interval between the arrival of the interaction beam at the foil and the arrival of the imaging protons. The images illustrate the transition from 2-D symmetric expansion of magnetic fields, during a 1-ns laser illumination, to a more-asymmetric 3-D expansion after the laser turned off and the plasma cooled and became more resistive; this asymmetry is conjectured to be driven by a resistive MHD interchange instability. (b) Images simulated by *LASNEX + LSP* for the conditions that produced the experimental images shown in (a).

magnetic field predicted in these simulations in a plane perpendicular to the foil at 0.6 ns. The protons would travel from right to left in the plane of this field map, and the maximum line integrals would be at the edges.

At times after the laser beam is off, the simulations do not track the data as well. As shown in Fig. 109.22(b) (1.5 to 3 ns), simulations predict that the proton images have a double ring structure. The outer ring comes from the outer edge of the plasma bubble where large ∇T_e occurred; the inner ring comes from the toroidal magnetic field at the edge of the hole burned into the plastic by the interaction laser, as seen in Fig. 109.23(b) for 1.5 ns. Figure 109.23(b) shows that the simulations also predict a second plasma bubble with a surface B field on the rear face of the foil after the laser has completely burned through; the direction of this field is reversed relative to the field on the front of the foil, but the simulated images show no major feature associated with this field because it is relatively weak.

At 2.3 ns in Fig. 109.22, the data and simulation are generally similar to each other. They each have an inner ring that corresponds to the burnthrough field, as described above, though it is a little smaller in the simulation than in the data. They each show a boundary farther out that corresponds to the outer surface of the bubble, but in the data it is strikingly asymmetric while in the simulation it is round because the code is limited to a 2-D structure.

We believe this is the first direct observation of the pressure-driven, resistive MHD interchange instability in laser-produced HED plasmas at the interface between the bubble and field. This instability, which involves the interchange of field between the inside and outside of the bubble surface, occurs when the plasma is resistive and there is unfavorable field curvature ($\boldsymbol{\kappa} \cdot \nabla p > 0$, where $\boldsymbol{\kappa} = \mathbf{B} \cdot \nabla \mathbf{B}/B^2$ is the field-line curvature and ∇p is the pressure gradient).[2] It makes sense that the instability occurs only after the laser is off, when the cooling plasma becomes more resistive.

There are strong similarities in the angular structure of this region from one image to the next (five to ten cycles over the 360° around the bubble), in spite of the fact that the images are from different shots. It seems that once the power input from the laser disappears, the plasma bubble quickly becomes asymmetric, but something systematic must be seeding the asymmetry. The physics behind this process is conjectured to be highly localized resonance absorption of linearly polarized laser light caused by obliquely incident light (23° from the normal) in an inhomogeneous ($\nabla n_e \neq 0$) plasma.[19] This phenomenon merits future experimental and theoretical investigation.

Another type of instability is apparent during the interval from 1.5 to 2.3 ns, where the distributions of beamlets near the image centers have some chaotic structure. The structures are quite different in each of the three images in this time interval, and since these images are from different shots, it would appear that the structure is random. We note that our earlier work[9] showed that a similar chaotic structure would occur if the laser was on and if no laser phase plates were used; phase plates either prevented the chaotic structure from forming as long as the laser was on or reduced its amplitude sufficiently that it was not visible until it had a chance to grow over a longer time

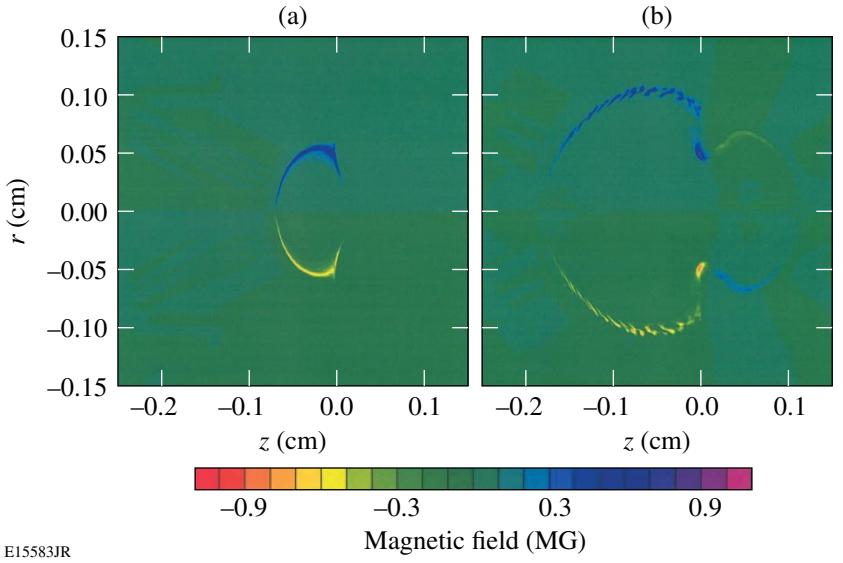

Figure 109.23
Time evolution of *LASNEX*-simulated *B*-field strength on a cross section of the plasma bubble in a plane perpendicular to the foil at (a) ~0.6 ns, when the laser was on, and (b) ~1.5 ns, when the laser was off. In each case, the horizontal coordinate z is the distance from the foil (assuming the laser is incident from the left), and the vertical coordinate r is the distance from the central axis of the plasma bubble. When the laser is on, strong fields occur near the edge of the plasma bubble. After the laser pulse, strong fields also appear near the edge of the hole burned into the foil by the laser and weaker fields (with the opposite direction) appear on the backside of the foil.

period (possibly due to the electron thermal instability when the plasma cools and becomes more resistive, driven by heat flow and leading to a random filamentary structure of n_e and T_e, as well as B fields[10]). The phase plates presumably result in a more-uniform temperature profile and a reduced medium-scale random structure associated with localized regions of strong $\nabla n_e \times \nabla T_e$ (Refs. 9 and 16).

Similar features are seen as late as our last image at 3 ns, although by this time the field strengths have diminished so that the amplitudes of all beamlet displacements are small. Although both simulation and experiment show a continued expansion of the plasma bubble at late times, leading to convective losses, the beamlet displacements in the data are much smaller than those in the simulation, indicating that fields have dissipated much more quickly than predicted. However, since the data reveal a 3-D structure after the laser is off, we have to realize that 2-D computer codes simply cannot model this time interval (although they are still useful for aiding qualitative interpretation of the images, particularly the role of the burnthrough hole in producing a static pattern in the images). Experimental measurements such as those shown here are therefore doubly important since they directly reveal previously unpredicted physical phenomena and also provide invaluable information for benchmarking true 3-D code development in the future.

Quantitative conclusions can be drawn from the images by measuring the sizes of features in the images and the displacements ξ of individual beamlet positions in the images. The displacements ξ of individual beamlet positions in the images result from the Lorenz force $\left| \int \mathbf{B} \times d\ell \right|$ and represent not lateral displacements at the foils but angular deflections from interactions with fields near the foil leading to lateral displacement at the detector. The actual bubble size is thus not determined directly by the apparent size in the image because the image of the bubble is magnified by radial beamlet displacements. The position of the actual bubble edge is inferred by determining the locations that the beamlets in the pileup region would have had in the image without displacement. The result of this analysis is shown in Fig. 109.24(a), where the radius at late times (when the bubble is asymmetric) represents an angular average. We see that the bubble radius grows linearly while the laser is on and then continues to expand after the laser is off. In addition to the radii of the plasma bubble, Fig. 109.24(a) also shows the radius of the burnthrough holes. Once the laser is off, this radius changes very little.

The maximum displacement ξ in each image represents the maximum value of $\left| \int \mathbf{B} \times d\ell \right|$; the values from the images of Fig. 109.22(a) are plotted in Fig. 109.24(b). The maximum value of this integral occurs at the end of the laser pulse, and it decays thereafter; the value predicted by *LASNEX* does not decay as fast. We note that while the laser is on, this maximum occurs at the outside of the plasma bubble, but after the laser is off, the maximum occurs at the edge of the burnthrough hole.

In summary, we have measured the spatial structure and temporal evolution of magnetic fields generated by laser–plasma interactions for the first time over a time interval that is long compared to the laser pulse duration, using monoenergetic proton radiography. Our experiments demonstrated that while a long-pulse, low-intensity laser beam illuminates a plastic foil, a hemispherical plasma bubble forms and grows linearly, surrounded by a symmetric, toroidal B field. After the laser pulse turns off, the bubble continues to expand, but field strengths decay and field structure around the bubble edge becomes asymmetric due, presumably, to the resistive MHD interchange instability. A significant part of that asymmetric structure is repeatable in different experiments, indicating that the asymmetry must have been seeded by some aspect of the experiment, like resonance absorption of obliquely incident, linearly polar-

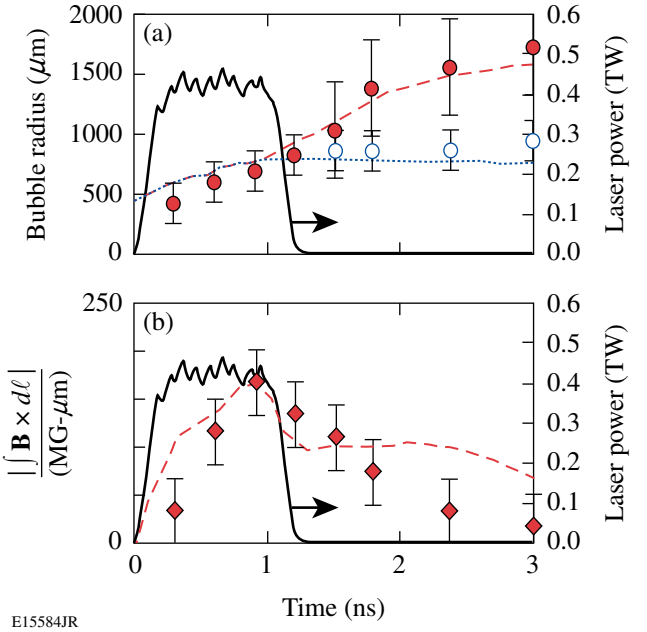

Figure 109.24
(a) Evolution of sizes at the foil, inferred from the images, for the plasma bubble radius (solid circles) and the burnthrough hole (open circles), compared with simulations (dashed and dotted lines, respectively). (b) Evolution of the maximum measured value of $\left| \int \mathbf{B} \times d\ell \right|$ (diamonds), compared with *LASNEX* simulations (dashed line). The solid lines in both (a) and (b) represent the 1-ns OMEGA laser pulse.

ized laser light by an inhomogeneous plasma. Nonrepeatable chaotic structure forms at the center of the plasma bubble after the laser is off, possibly due to a resistivity-induced electron thermal instability. *LASNEX + LSP* simulations agree fairly well with data while the interaction laser is on, aiding the interpretation of the measured images, but the 2-D limitation of these simulations prevents them from predicting some large 3-D structures that develop after the laser is off.

ACKNOWLEDGMENT

The work described here was performed in part at the LLE National Laser Users' Facility (NLUF) and was supported in part by U.S. DOE (Grant No. DE-FG03-03SF22691), LLNL (subcontract Grant No. B504974), and LLE (subcontract Grant No. 412160-001G).

REFERENCES

1. B. B. Kadomstev, in *Reviews of Plasma Physics*, edited by M. A. Leontovich (Consultants Bureau, New York, 1966), Vol. 2, pp. 153–199.
2. J. P. Freidberg, *Ideal Magnetohydrodynamics* (Plenum Press, New York, NY, 1987).
3. W. Baumjohann and R. A. Treumann, *Basic Space Plasma Physics* (Imperial College Press, London, 1996).
4. S. Eliezer, *The Interaction of High-Power Lasers with Plasmas* (Institute of Physics Publishing, Bristol, England, 2002).
5. M. G. Haines, Phys. Rev. Lett. **78**, 254 (1997).
6. S. I. Braginskii, in *Reviews of Plasma Physics*, edited by Acad. M. A. Leontovich (Consultants Bureau, New York, 1965), Vol. 1, p. 205.
7. J. A. Stamper *et al*., Phys. Rev. Lett. **26**, 1012 (1971); D. G. Colombant and N. K. Winsor, Phys. Rev. Lett. **38**, 697 (1977); A. Raven, O. Willi, and P. T. Rumsby, Phys. Rev. Lett. **41**, 554 (1978); M. Borghesi *et al*., Phys. Rev. Lett. **81**, 112 (1998); A. J. Mackinnon, P. K. Patel, R. P. Town, M. J. Edwards, T. Phillips, S. C. Lerner, D. W. Price, D. Hicks, M. H. Key, S. Hatchett, S. C. Wilks, M. Borghesi, L. Romagnani, S. Kar, T. Toncian, G. Pretzler, O. Willi, M. Koenig, E. Martinolli, S. Lepape, A. Benuzzi-Mounaix, P. Audebert, J. C. Gauthier, J. King, R. Snavely, R. R. Freeman, and T. Boehly, Rev. Sci. Instrum. **75**, 3531 (2004); U. Wagner *et al*., Phys. Rev. E **70**, 026401 (2004).
8. M. G. Drouet and R. Bolton, Phys. Rev. Lett. **36**, 591 (1976); M. A. Yates *et al*., Phys. Rev. Lett. **49**, 1702 (1982).
9. C. K. Li, F. H. Séguin, J. A. Frenje, J. R. Rygg, R. D. Petrasso, R. P. J. Town, P. A. Amendt, S. P. Hatchett, O. L. Landen, A. J. Mackinnon, P. K. Patel, V. A. Smalyuk, T. C. Sangster, and J. P. Knauer, Phys. Rev. Lett. **97**, 135003 (2006).
10. M. G. Haines, Phys. Rev. Lett. **47**, 917 (1981).
11. R. P. J. Town *et al*., Bull. Am. Phys. Soc. **51**, 142 (2006).
12. G. B. Zimmerman and W. L. Kruer, Comments Plasma Phys. Control. Fusion **2**, 51 (1975).
13. P. D. Nielsen and G. B. Zimmerman, Lawrence Livermore National Laboratory, Livermore, CA, UCRL-53123 (1981).
14. D. R. Welch *et al*., Nucl. Instrum. Methods Phys. Res. A **464**, 134 (2001).
15. T. R. Boehly, D. L. Brown, R. S. Craxton, R. L. Keck, J. P. Knauer, J. H. Kelly, T. J. Kessler, S. A. Kumpan, S. J. Loucks, S. A. Letzring, F. J. Marshall, R. L. McCrory, S. F. B. Morse, W. Seka, J. M. Soures, and C. P. Verdon, Opt. Commun. **133**, 495 (1997).
16. T. J. Kessler, Y. Lin, J. J. Armstrong, and B. Velazquez, in *Laser Coherence Control: Technology and Applications*, edited by H. T. Powell and T. J. Kessler (SPIE, Bellingham, WA, 1993), Vol. 1870, pp. 95–104.
17. C. K. Li, F. H. Séguin, J. A. Frenje, J. R. Rygg, R. D. Petrasso, R. P. J. Town, P. A. Amendt, S. P. Hatchett, O. L. Landen, A. J. Mackinnon, P. K. Patel, V. Smalyuk, J. P. Knauer, T. C. Sangster, and C. Stoeckl, Rev. Sci. Instrum. **77**, 10E725 (2006).
18. F. H. Séguin, J. L. DeCiantis, J. A. Frenje, S. Kurebayashi, C. K. Li, J. R. Rygg, C. Chen, V. Berube, B. E. Schwartz, R. D. Petrasso, V. A. Smalyuk, F. J. Marshall, J. P. Knauer, J. A. Delettrez, P. W. McKenty, D. D. Meyerhofer, S. Roberts, T. C. Sangster, K. Mikaelian, and H. S. Park, Rev. Sci. Instrum. **75**, 3520 (2004).
19. W. L. Kruer, *The Physics of Laser Plasma Interactions* (Westview Press, Boulder, CO, 2003).

Performance of the 1-MJ, Wetted-Foam Target Design for the National Ignition Facility

Introduction

The primary mission of the National Ignition Facility (NIF)[1] is to demonstrate fusion ignition via inertial confinement fusion (ICF).[2] In the direct-drive[3,4] approach to ICF, a spherical target is illuminated by a number of laser beams arranged symmetrically in a configuration that provides adequate drive symmetry. The target shell is accelerated inward as its outer layers expand due to ablation. After the end of the laser pulse, shock dynamics and compression of the contained gas cause the shell to decelerate. During both the acceleration and deceleration phases of the implosion, the target is subject to Rayleigh–Taylor (RT) instability (see Ref. 3 and references therein)—first on the outer, then the inner surface of the shell. The acceleration-phase instability is seeded by the roughness of the outer surface of the shell, by nonuniformities in the illumination profiles of the individual beams, by beam mispointing, by energy imbalance and mistiming between the various beams, by the drive nonuniformity inherent in the geometric arrangement of the beams, and by the feedout of perturbations to the ablation surface from the inner surface of the shell by means of rarefaction waves. The deceleration-phase RT instability is seeded by the initial roughness of the inner surface of the shell and by nonuniformities that feed through to the inner surface by laser-driven shocks. Target-fabrication techniques have been developed to improve the target-surface smoothness, including the use of β-layering of the DT-ice surface.[5] The single-beam nonuniformities may be reduced through various beam-smoothing methods, such as smoothing by spectral dispersion (SSD),[6] polarization smoothing,[7] or distributed phase plates.[8] Even with these techniques, a target must be designed in such a way as to remain integral during the implosion and uniform enough to produce a hot spot that can initiate a burn wave in the fuel of the shell.

In this article, we present a target design that uses a plastic foam ablator saturated with deuterium–tritium (DT) ice (so-called "wetted foam"). Due to the dependence of inverse bremsstrahlung absorption on the atomic number ($\kappa \sim \langle Z^2 \rangle / \langle Z \rangle$ see Ref. 9), the wetted foam has a higher laser-coupling efficiency than pure DT. Plastic foam shells were originally proposed as a matrix for liquid DT fuel.[10] Others[11,12] proposed the use of foam as an ablator, in conjunction with a high-atomic-number material. In these designs, radiation from the high-atomic-number material preheats the foam, increasing the ablation velocity and reducing outer-surface instability. In the design presented here, the wetted foam is used primarily because of the increase in laser absorption.[13] Other proposed uses of foam include target designs for inertial fusion energy,[14] as well as for reduction of laser imprint.[15]

The stability of this design with respect to the primary sources of target and drive nonuniformity has been determined using two-dimensional (2-D) simulations with the hydrocode *DRACO*.[16] To weigh the effects of these different sources, a nonuniformity-budget analysis is performed in the manner of McKenty *et al.*[17] This analysis maps nonuniformity from different sources to a parameterization of the inner-shell-surface spectrum at the end of the acceleration phase, which in turn allows prediction of target performance. Following a description of the design in the next section, the tolerance of the design to nonuniformity sources is presented; the results from integrated simulations including ice and surface roughness, multiple-beam nonuniformity (primarily due to port geometry and power imbalance between beams), and imprint are shown; and, finally, the conclusions from the nonuniformity-budget analysis and the integrated simulations are presented.

The 1-MJ, Wetted-Foam Design

The 1.5-MJ, all-DT, direct-drive point design for symmetric drive on the NIF, shown in Fig. 109.25(a), consists of a DT shell surrounded by a thin layer of plastic (CH; see Ref. 17). The same design, scaled to an incident energy of 1 MJ, and the 1-MJ wetted-foam design are shown in Figs. 109.25(b) and 109.25(c). An incident energy of 1 MJ has been chosen to match energy restrictions to reduce the risk of damage to the NIF's optical elements. Table 109.III shows that the laser absorption, averaged over the length of the laser pulse, is ~60% to 65% for the all-DT designs. When part of the DT shell is replaced by a $CH(DT)_4$ wetted-foam ablator, the higher-average atomic number of the ablator results in an absorption of 86%

(Table 109.III). This allows a greater fraction of the incident laser energy to be converted to shell kinetic energy, allowing a thicker shell to be driven. The resulting 1-D gain for the 1-MJ, wetted-foam target is ~10% higher than that of the 1.5-MJ, all-DT design.

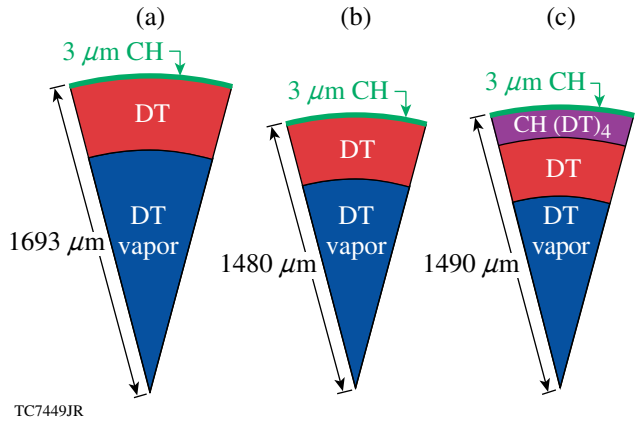

Figure 109.25
(a) The 1.5-MJ, all-DT, direct-drive target design for the NIF, (b) the same design scaled for an incident laser energy of 1 MJ, and (c) the 1-MJ, wetted-foam design. The wetted-foam shell is 326 μm thick, with 216 μm of pure DT fuel.

Table 109.III: Properties of the 1.5-MJ, all-DT; 1-MJ, all-DT; and 1-MJ, wetted-foam designs. Here A is the rms bubble amplitude at the end of the acceleration phase and ΔR is the in-flight shell thickness.

	All-DT	Scaled, All-DT	Wetted-foam
Energy (MJ)	1.5	1	1
Target radius (μm)	1695	1480	1490
Absorption (%)	65	59	86
$A/\Delta R$ (%)	30	33	11
Gain	45	40	49

The density of $CH(DT)_4$ is 304 mg cm^{-3}, corresponding to a dry-foam density of 120 mg cm^{-3}, given that during the freezing process the liquid DT contracts in volume by 17%, leaving voids in the wetted-foam layer. This is only 22% greater than the density of pure DT ice. This dry-foam density provides higher absorption, while not generating enough radiation to appreciably raise the fuel isentrope (as measured by the adiabat α, given by the ratio of the pressure to the cold Fermi-degenerate pressure). The wetted-foam-layer thickness ensures that the foam is entirely ablated by the end of the laser pulse. In an ignition design such as this, the first laser-driven shock, whether steady or, for picket designs, decaying, determines the shell adiabat. This is the only strong laser-driven shock, and it is the only shock to encounter unmixed foam and DT. High-resolution hydrodynamic simulations modeling the wetted-foam mixture have shown that after the initial undercompression behind the first shock,[18] the flow variables asymptote to within a few percent of the Rankine–Hugoniot values for ICF-relevant shock strengths.[19] These simulations demonstrate that the fluctuation decay scale length behind the shock is less than 2 μm, where this scale length is defined for a quantity q as $Lq = dr/d\ln\langle q\rangle$, and $\langle q\rangle$ is the average of q in the shock frame in the direction perpendicular to the shock [see Eq. (1) of Ref. 19]. These findings allow the wetted-foam layer to be modeled as a homogeneous mixture in the simulations described here.

Assuming an ICF shell remains intact during the acceleration phase, the most dangerous modes during deceleration are those that feed through from the outer to the inner surface. Modes feed through attenuated by a factor $\exp(-k\Delta R)$, where k is the wave number and ΔR is the shell thickness; the long-wavelength modes with $k \sim 1/\Delta R$ feed through most effectively. The number N of e-foldings of growth experienced by these modes during acceleration may be approximated by $N \sim \gamma\Delta t \sim (kgt^2)^{1/2}$, where γ is the growth rate over the time period Δt during which the shell is accelerated by the laser pulse, which is proportional to the classical growth rate for long-wavelength modes. Writing this in terms of the distance traveled by the shell, which is proportional to the initial outer shell radius R_0, $N \sim \left(R_0/\Delta R\right)^{1/2} \equiv (\mathrm{IFAR})^{1/2}$, where IFAR is the in-flight aspect ratio of the imploding shell. This is related to the implosion velocity v and the average shell adiabat by $\mathrm{IFAR} \sim v^2/\langle\alpha\rangle^{3/5}$ (Ref. 3). These relations show that the integrity of the shell during acceleration depends on the IFAR. The shell stability can be improved by lowering the implosion velocity or lowering the IFAR by increasing the shell thickness, which is equivalent to raising the average adiabat, since $\Delta R \sim \langle\alpha\rangle^{3/5}$. For a target where the adiabat is a constant function of shell mass, increasing the adiabat reduces the fuel compressibility and target gain. For a design such as this one, which has a shaped adiabat, N is reduced by a term proportional to $v\left(\alpha_{\mathrm{out}}/\langle\alpha\rangle\right)^{0.6}$, where α_{out} is the ablator adiabat.[20] The shell instability of the wetted-foam design is reduced from that of a 1-MJ-scaled, all-DT design by lowering the shell velocity by ~60 μm/ns (see Table 109.IV). As a result, the shell is less unstable during the acceleration phase, and the rms bubble amplitude divided by the shell thickness $A/\Delta R$, computed from 1-D simulations using a postprocessor,[21] is lower by a factor of 3 for the 1-MJ, wetted-foam design.

The increase in shell mass has the added benefit of raising the areal density of the shell at the time of ignition, making the shell more robust to deceleration-phase instabilities. Any RT growth on the inner edge of the shell during deceleration delays the onset of ignition, effectively lowering the shell velocity.[22] The inward motion of the shell at the time of ignition is necessary to offset the tremendous pressure the expanding burn wave exerts on the shell. If left unimpeded, the pressure of the burn wave would decompress the shell prematurely, quenching any possibility of high gain. In addition, decreasing the implosion velocity decreases the work done compressing the hot spot and reduces the hot-spot temperature. Further, a reduction in hot-spot temperature reduces the effects of ablative stabilization of the deceleration-phase RT instability. Due to these effects, the minimum energy needed for ignition scales with IFAR as $E_{ign} \sim (\text{IFAR})^{-3}$ (Ref. 20). The margin, defined as the inward-moving kinetic energy at ignition divided by the peak inward kinetic energy, is a measure of the additional kinetic energy of the shell above that needed for ignition. As seen in Table 109.IV, the decrease in IFAR and increase in shell mass have the effect of lowering the margin for the wetted-foam design. As will be shown in the following section, this design tolerates 1.75 μm of ice roughness, suggesting sufficient margin.

The laser pulse shape, shown in Fig. 109.26, uses an initial high-intensity picket to generate a decaying shock. As this shock propagates through the shell, its strength decreases to that supported by the foot, causing the level of shock heating to decrease from the ablator to the inner edge of the shell. This shapes the adiabat,[23] producing a high-ablator adiabat of ~10 while retaining a low-fuel adiabat of ~2. (Other adiabat-shaping techniques include the use of a relaxation picket where the

Table 109.IV: The wetted-foam design's shell is thicker than that of the all-DT design scaled to 1 MJ. This reduces shell instability and increases the areal density, but at the cost of a lower margin.

	V (μm/ns)	ΔR (μm)	IFAR	$A/\Delta R$ (%)	Areal density ρR (g/cm^2)	Margin (%)
1-MJ, all-DT	430	285	69	33	1.1	45
Wetted-foam	372	323	28	11	1.4	30

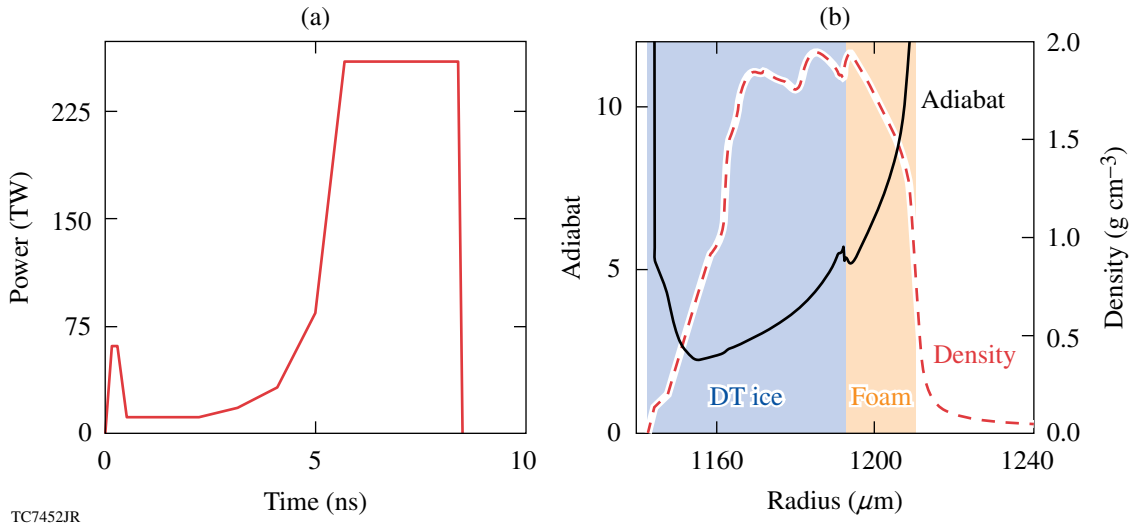

Figure 109.26
(a) The laser pulse and (b) the adiabat and mass density of the shell shortly after shock breakout. The laser pulse consists of an initial intensity spike or "picket" followed by a foot of low constant intensity and a rise to a high-power drive pulse.

laser intensity is zero between the picket and the foot pulse,[24] and a series of such isolated picket pulses preceding the main drive pulse.[12]) This technique reduces the shell instability and laser imprint during the acceleration phase since the ablation velocity is proportional to $\alpha^{3/5}$ (see Ref. 3). At the same time, it maintains the low-fuel adiabat needed to compress the fuel and achieve ignition. The picket also lowers imprint by decreasing the duration of the period of acceleration due to the outer CH layer and by increasing the rate of growth of the conduction zone between the ablation and critical surfaces.[25]

This design is robust to shock mistiming, critical for a successful ICF target design. The shock timing depends on accurate modeling of the equation of state (EOS) of the wetted-foam mixture and the DT. The effect on 1-D gain of changing either the foot length or power is shown in Fig. 109.27. These simulations show a reduction in gain of less than 10% for a variation in the foot-pulse length of ±250 ps, well within the NIF specification[26] of 100 ps. A change in power of ±4%, comparable to the NIF specification, produces a gain reduction of ~8%. It is anticipated that the shock timing will be verified experimentally using the materials of interest.

Nonuniformity-Budget Analysis

Four sources of nonuniformity contribute to the RT instability during the implosion. These include inner-surface DT-ice roughness, outer-surface roughness, and single-beam and multiple-beam nonuniformity. To gauge their relative importance and estimate their effects on target gain in an integrated simulation incorporating all four, a nonuniformity budget has been developed.[17,27] McKenty *et al.*[17] found that target gain may be approximated as a function of a weighted average of the inner-surface ice spectrum at the end of the acceleration phase,

$$\overline{\sigma} = \sqrt{a\sigma^2_{\ell<10} + \sigma^2_{\ell>9}},$$

regardless of the source of the ice perturbations. The low-mode weighting factor is $a = 0.06$. (The end of the acceleration phase is taken as the time when the ablation-front acceleration changes sign, shortly after the end of the laser pulse.) In 2-D simulations of the wetted-foam design incorporating various levels and spectral indices of ice roughness, it was found that this weighting factor provides reasonable scaling for this design as well.

This spectral weighting is based on the different effects that short-wavelength modes have on the hot spot. Any mode growth increases the hot-spot surface area, enhancing the cooling due to thermal conduction with the shell. For short wavelengths, the spikes of a single-mode perturbation on the inner surface of the shell lie close enough together that they cool below the temperatures at which they can contribute to α-particle generation. For these modes, the hot-spot size is effectively reduced by the physical extent of the perturbation.[28] Gain reduction becomes independent of wavelength for these high modes depending only on mode amplitude. Kishony and Shvarts[28] show that this behavior occurs for modes with $\ell > 9$. Because the dependence of yield on $\overline{\sigma}$ is independent of the source of the nonuniformity, the target gain may be estimated by adding the contributions to $\overline{\sigma}$ in quadrature and using the gain as a function of $\overline{\sigma}$ found, for instance, from simulations of just initial ice roughness.

Each of the sources of nonuniformity was simulated in 2-D. The laser-energy deposition was modeled using a straight-line ray-trace algorithm. To incorporate the reduction of coupling due to refraction, the absorbed energy determined from a 1-D simulation was used as the incident energy in 2-D simulations. This method provides a drive that closely replicates the adiabat

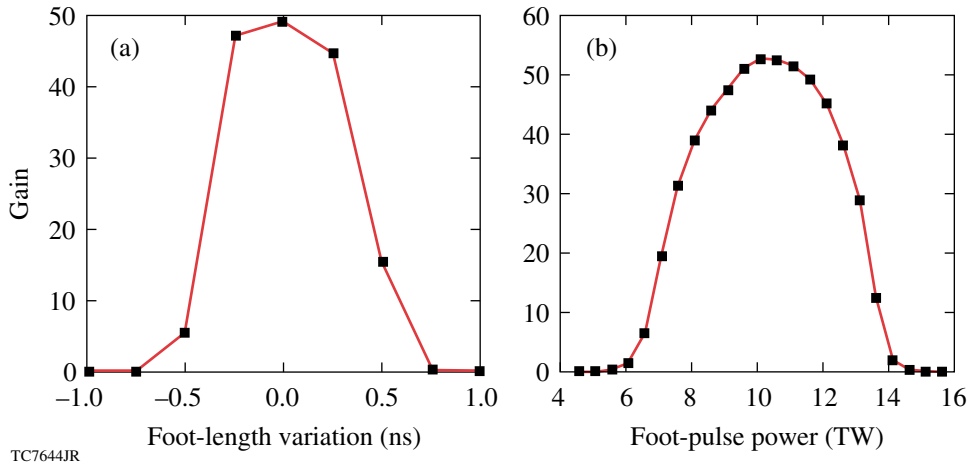

Figure 109.27
Sensitivity of the wetted-foam design's 1-D target gain to (a) deviation in the foot-pulse length and (b) foot-pulse power.

in the 1-D simulation. The pulse was truncated to ensure that the acceleration-phase stability, as determined using a 1-D postprocessor,[21] and the shell areal density at the time of ignition remained the same, and the implosion velocity differed by only 3%. Without refraction, however, the conduction zone is smaller, leading to more-efficient imprint.[29] It is expected that when these simulations are repeated using refractive laser-energy deposition, the target will be somewhat less sensitive to single-beam nonuniformity.

1. Initial DT-Ice Surface Roughness

The amplitude spectrum of initial inner-surface ice roughness has been found for cryogenic D_2 targets fabricated at LLE and is approximated here by a power law in mode number $A_\ell = A_0 \ell^{-\beta}$, where $\beta \sim 2$. The power for these modes lies primarily in $\ell < 50$. A series of 2-D simulations of ice-surface roughness were performed for various spectral amplitudes A_0 and power-law indices β, including modes 2 to 50. The resolution used for these simulations was about eight zones per wavelength for $\ell = 50$. The target gain as a function of initial rms ice roughness for $\beta = 2$ is shown in Fig. 109.28(a). This target was found to withstand 1.75 μm of initial ice roughness with little degradation in performance. When a power-law index of 1.5 was used, this design showed greater tolerance to ice roughness than the 1.5-MJ design presented in Ref. 17. This is most likely because of the higher areal density, 1.4 g cm^{-2}, of the wetted-foam design.

Figure 109.28(b) shows the shell at the time of ignition, when the hot-spot ion temperature has reached 10 keV. The density contours show that the hot spot is primarily distorted by modes 2 to 6. The dependence of gain on $\overline{\sigma}$ is shown in Fig. 109.29. It can be seen that this 1-MJ design can tolerate a $\overline{\sigma}$ of slightly less than 1 μm, compared with ~2 μm for the 1.5-MJ design of Ref. 17. For $\overline{\sigma} \gtrsim 0.8$ μm in the wetted-foam design, the RT

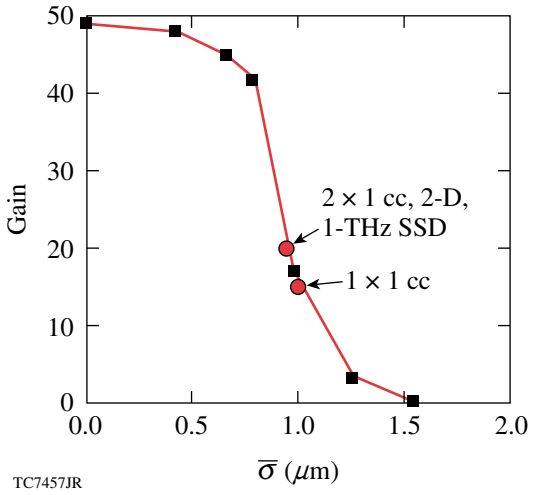

Figure 109.29
The dependence of gain on the parameter $\overline{\sigma}$ is shown, determined from simulations of initial ice-layer roughness for an ice spectrum with a power-law index of $\beta = 2$.

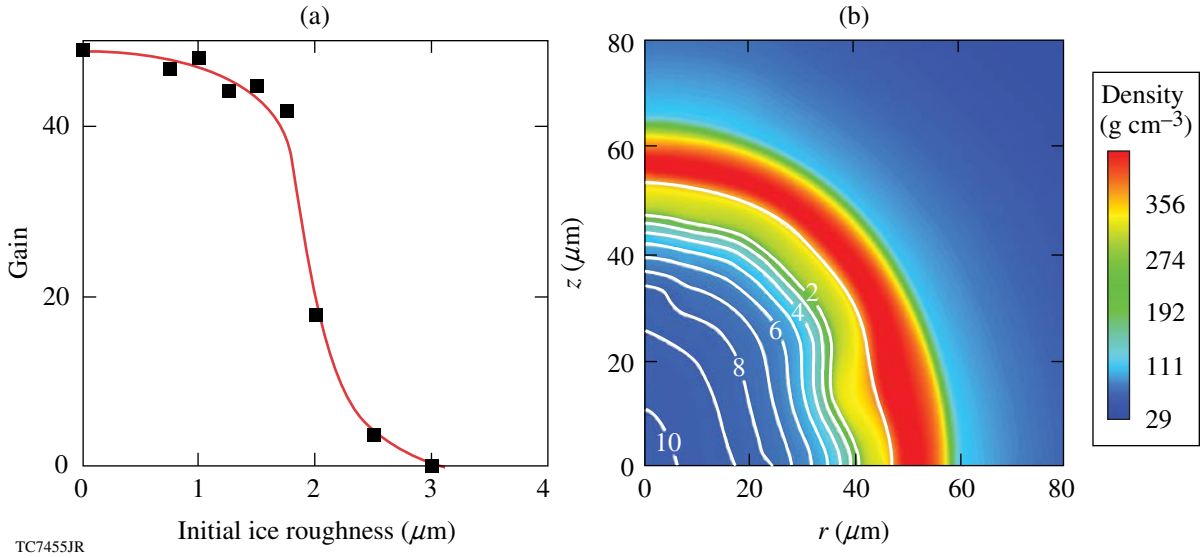

Figure 109.28
(a) The gain as a function of initial ice roughness for a power-law index of 2. This target tolerates an rms ice roughness of ~1.75 μm before deviation from the 1-D gain. (b) The shell at the time of ignition for the case of 1.75-μm-rms ice roughness is also shown. The gray scale shows mass density, and contour lines indicate ion temperature in keV. Note that the hot spot is primarily distorted by modes 2 to 6.

growth delays the onset of ignition, which consumes part of the margin leading to a lower burnup fraction at ignition.[22] The lower tolerance of this design compared to the 1.5-MJ design is due to the reduction in margin caused by the lowering of the incident laser-driver energy.

2. Outer-Surface Roughness

Foam-target fabrication at General Atomics has made significant strides in the past few years. Resorcinol-formaldehyde foam shells with submicron pore sizes (less than 0.25 μm) and thin (~5-μm) CH overcoats have been diagnosed using atomic-force microscopy.[30] The measured mode-amplitude spectrum shows spectral dependence roughly proportional to ℓ^{-2}, with most of the power in modes less than ten. The overall rms roughness for these foam shells has been shown to be as low as ~450 nm, about four times larger than that of the NIF's CH-surface standard roughness (Ref. 17 and references therein).

A 2-D simulation incorporating this surface spectrum, modeled as ribbon modes, resulted in a $\overline{\sigma}$ value of 0.38 μm and demonstrated negligible reduction in target gain. By comparison, a simulation using the NIF standard with an rms of ~115 nm produced a $\overline{\sigma}$ of 0.08 μm.

3. Multiple-Beam Nonuniformity

Multiple-beam nonuniformity, often referred to as beam-to-beam power imbalance, is caused by at least five sources of drive nonuniformity: variations in the power between the different laser beams, drive asymmetry caused by the geometry of the beam port locations and beam overlap, beam-pointing errors, and variations in beam timing. The nonuniformity spectrum has been determined as a function of time for the first four of these contributions for the wetted-foam laser pulse by spherical-harmonic decomposition of the illumination pattern of the beams projected onto the surface of the target. A harmonic modal spectrum is produced by combining all m modes in quadrature for each mode number ℓ. The symmetric NIF direct-drive port geometry contributes a constant perturbation, primarily in mode $\ell \le 6$. Beam mistiming, which is expected to have an rms value of 30 ps on the NIF,[26] produces perturbations in modes ℓ = 1 to 3, primarily during the rise and fall of the picket. Despite these perturbations, the mistiming of the picket was found to have a small effect on target performance.[31] The imbalance in energy between beams is expected to be ~8% rms on the NIF. The resulting perturbations are dominated by modes 2 to 12, with an amplitude of ~1%. The 2-D simulations described here include the effects of power imbalance between beams, beam overlap, and port geometry.

A series of six 2-D power-balance runs were performed. These simulations included modes 2 to 12, with 44 zones per wavelength of mode 12. They were performed using power-balance histories[17] adapted to the wetted-foam-design laser pulse. They produced an average reduction in gain of ~6%, with a $\overline{\sigma}$ of about 0.11 μm.

4. Single-Beam Nonuniformity

Single-beam nonuniformity or imprint is the source of nonuniformity capable of causing the greatest reduction in target yield, depending on the level of beam smoothing used. Illumination perturbations contribute to imprint through the perturbation in the laser-drive shock front and the acceleration perturbation in the post-shock region, which causes lateral flow in the shock-compressed material.[32] These produce secular growth during the foot pulse that seeds RT growth during the drive pulse. Several methods have been developed for reducing imprint. On the NIF these include SSD, distributed phase plates, and polarization smoothing. In the 2-D imprint simulations, we have modeled the effects of all three smoothing techniques. The DPP spectrum is modeled using an analytical fit for the laser speckle,[33] with amplitudes reduced to account for the effects of polarization smoothing and 40-beam overlap for the NIF's 192-beam system.

Two-dimensional SSD is modeled using a nondeterministic algorithm where the phase of each mode is assigned randomly every modal coherence time. The coherence time is given by a 2-D generalization of the formula $t_c = \left[\Delta\nu \sin\left(n_c \pi \ell / \ell_{\max}\right)\right]^{-1}$ (Ref. 34), where $\ell_{\max} = 2\pi R_0 / \delta$ is the mode number corresponding to half the speckle size δ, $\Delta\nu$ is the SSD bandwidth, and n_c is the number of color cycles on the laser system. The randomly chosen phases for each mode repeat after a number of coherence times, which depends on the mode number and the angular divergence in each dimension, implementing the asymptotic level of smoothing achievable by SSD. This asymptotic limit is much larger for 1-D SSD than for 2-D, resulting in much greater imprint, as will be seen below. For long-wavelength modes the number of statistically independent speckle patterns is small enough that a single simulation does not fully sample the ensemble of possible phase choices. For this reason, many of the runs here were repeated several times.

The reduction in growth rate due to ablative stabilization means the ablation-front mode spectrum due to imprint decreases with increasing mode number (see, e.g., Fig. 4 of Ref. 32). When this spectrum feeds through to the inner surface of the ice, there is an additional reduction in amplitude for increasing mode number due to the attenuation factor

exp(–$k\Delta R$). The ice spectrum at the end of the acceleration phase is shown in Fig. 109.30 for a simulation modeling the effects of imprint from modes ℓ = 2 to 200. Due to the initial mode-number dependence in the imprint spectrum and the feedthrough attenuation, modes above ℓ = 100 contribute less than 1% to the overall rms. For this reason, additional 2-D imprint runs were performed including only modes up to 100. To reduce the simulation time, only even modes are modeled in these simulations, with the amplitudes of the odd modes added in quadrature. These simulations use a resolution of 14 zones per wavelength at ℓ = 100, which has been found to be sufficient to resolve the smallest perturbation wavelengths.

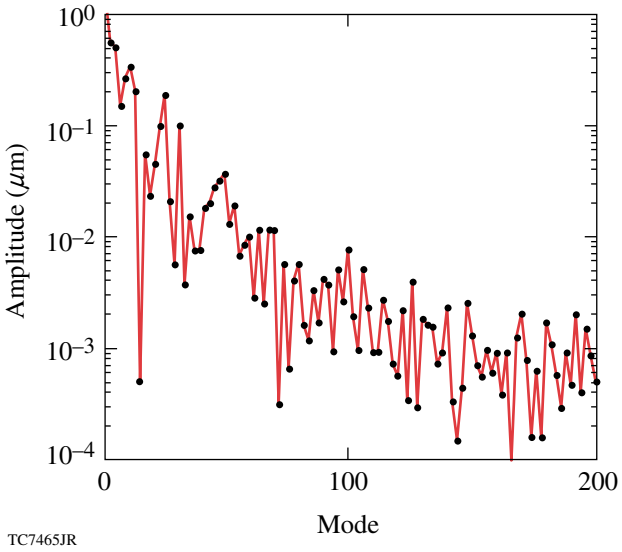

Figure 109.30
The DT-ice-roughness spectrum on the inner surface of the shell at the end of the acceleration phase for a simulation modeling the effects of imprint in modes up to ℓ = 200. Due to the mode-number dependence on the imprint spectrum and feedthrough attenuation, modes above ℓ ~ 100 contribute negligibly to the total rms.

The characteristic smoothing time T for SSD, given by the inverse of the smoothing rate, is related to the key SSD parameters by $T \sim (\nu_m n_c \delta)^{-1} \sim (\Delta\nu n_c)^{-1}$, where ν_m is the modulator depth. To determine the dependence of target performance on smoothing time, we have performed simulations for four different levels of SSD bandwidth: 1.33 THz, 0.89 THz (referred to here and elsewhere as "1-THz" SSD), 590 GHz, and 295 GHz. These all use one color cycle in each direction and modulator frequencies of 15.4 GHz and 2.81 GHz. The shell at the end of the acceleration phase is shown for each of these simulations in Fig. 109.31. The dependence of imprint on the bandwidth is clearly seen in the level of perturbation on the outer shell surface: whereas the shell from the 1.3-THz simulation is intact and relatively unperturbed, that from the ~0.3-THz simulation is completely broken up. The $\overline{\sigma}$ values for imprint alone are shown in Fig. 109.31: 0.37 μm, 0.86 μm, 0.96 μm, and 2.3 μm for 1.3 THz, 0.9 THz, 0.6 THz, and 0.3 THz, respectively. For comparison, the $\overline{\sigma}$ value from a simulation with 2-D, 1-THz SSD with two color cycles in one direction and one in the other is just 0.43 μm, half of that found with one color cycle in each direction and the same bandwidth. When the $\overline{\sigma}$ values from the simulations shown in Fig. 109.31 are combined in quadrature with those due to energy imbalance, port geometry and beam overlap, foam surface roughness, and 1-μm initial ice roughness, they are increased to 0.74 μm, 1.07 μm, 1.15 μm, and 2.43 μm. The projected gain factors from these sums are 39, 12, 8, and 0.008, respectively.

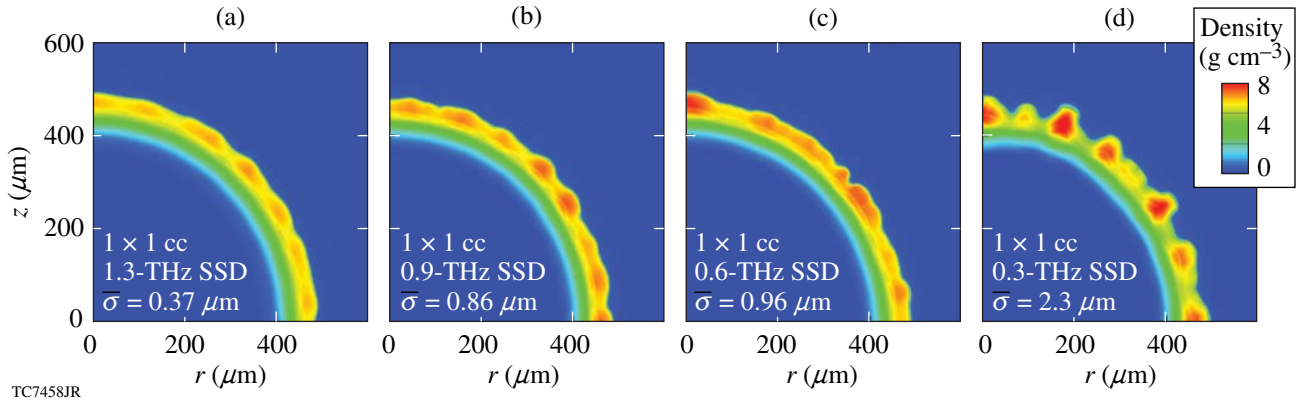

Figure 109.31
The shell is shown at the end of the acceleration phase for 2-D simulations of imprint modes 2 to 100, with one color cycle of SSD in each dimension and descending levels of bandwidth, showing the reduction in smoothing and the performance parameter $\overline{\sigma}$ just from imprint.

The SSD parameters that are currently anticipated for the NIF are much different from those required for an all-DT, direct-drive target at 1.5 MJ (Ref. 17), which we will refer to here as "2 × 1 SSD." The 2 × 1 SSD parameters are 2 and 1 color cycles in each direction, modulator frequencies of 15.4 GHz and 2.81 GHz, and a total UV bandwidth of 0.89 THz found by summing the individual bandwidths in quadrature. The anticipated NIF parameters for use with indirect-drive ignition (IDI) are 1-D SSD with 1.35 color cycles, a modulator frequency of 17 GHz, and a UV bandwidth of 185 GHz. These two sets of parameters have been simulated in 2-D, along with two intermediate levels of SSD: the 2 × 1 parameters but with just one color cycle in each direction ("1 × 1" SSD), and 2 × 1 SSD reduced to one dimension with two color cycles ("2 × 0" SSD). The shells at the end of the acceleration phase from multimode imprint simulations incorporating these levels of SSD are shown in Fig. 109.32. These simulations include all four sources of nonuniformity. The values of $\overline{\sigma}$ for these four simulations are 0.94 μm for the 2 × 1 SSD case, 1.0 μm for 1 × 1 SSD, 2.0 μm for 2 × 0 SSD, and 7.3 μm for IDI SSD. The projected gain factors for these integrated simulations are 21, 16, 0, and 0, respectively.

Integrated Simulations

Three integrated simulations were performed. The first two include drive asymmetry due to power imbalance and port geometry, surface roughness (370 nm), 0.75-μm initial ice roughness with a power-law index of $\beta = 2$, and single-beam imprint. The third uses a different initial ice spectrum with 2-D, 2 × 1 SSD beam smoothing and is discussed below.

The smoothing modeled in the first two simulations was polarization smoothing and either 2-D, 2 × 1 or 1-D, 2 × 0 SSD. The targets from these simulations, at the end of the acceleration phase and near the time of peak compression, are shown in Fig. 109.33. The 2-D SSD case has a much less perturbed shell at the end of acceleration than the 1-D SSD simulation. As a result, its hot spot is much more uniform at peak compression, showing primarily distortions with modes less than or equal to 6. The hot spot at this time (9.4 ns) is approximately 40 μm in size, and the neutron-averaged areal density is 1.31 g/cm^3. By comparison, the 1-D SSD simulation shows large perturbations at the end of acceleration that produce distortions over a wide spectral range at peak compression (9.3 ns). These distortions in the shell produce a more-distorted inner shell surface and lower ion temperatures at stagnation than in the 2-D SSD case and prevent the target from achieving gain greater than 1.

Smoothing levels due to 2-D and 1-D SSD are very different, even for long-wavelength modes. The shortest mode that can be smoothed by SSD is given by $\ell_{\min} = 2\pi R_0 / (2F\Delta\theta) \sim 4$ (Ref. 35), where F is the focal distance (7.7 m for the NIF) and $\Delta\theta^2 = \Delta\theta_1^2 + \Delta\theta_2^2$ is the effective far-field divergence, approximated by summing the contributions from each direction in quadrature. For 2 × 1, 2-D SSD, smoothing is effective above mode 4, and above mode 6 for 2 × 0, 1-D SSD. This is demonstrated in Fig. 109.34(a), which shows the smoothing due to SSD at 1 ns for modes up to 50. Note that even though the difference between 1-D and 2-D smoothing is small for modes less than 10, these modes also see less thermal smoothing[29] and a greater decoupling time than shorter-wavelength modes. Both 1-D and 2-D SSD smooth at the same rate prior to asymptoting. The difference in smoothing between 1-D and 2-D SSD is due to the difference in the asymptotic level. This is shown for mode number 22 in Fig. 109.34(b). For this

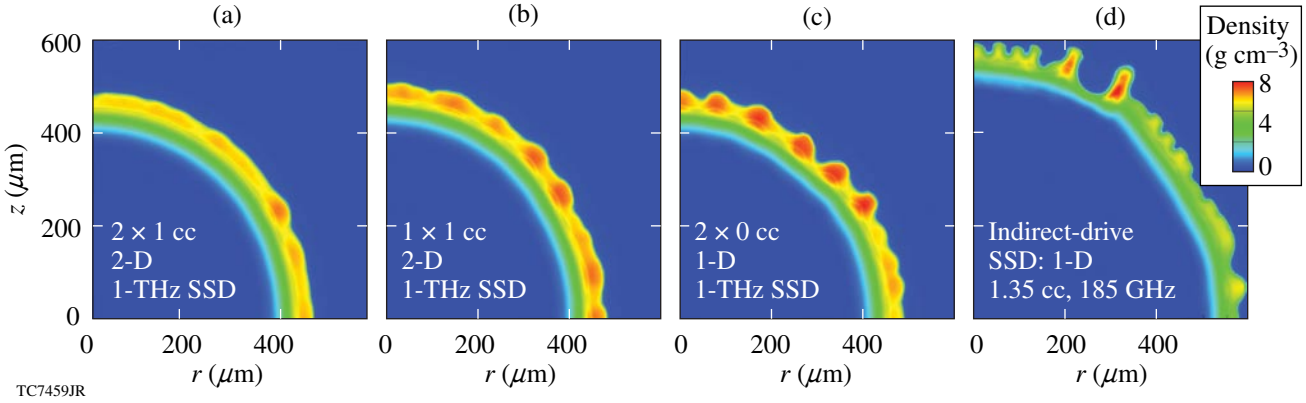

Figure 109.32
The shell at the end of the acceleration phase is shown for four 2-D simulations incorporating different sets of SSD parameters. These are integrated simulations that also include the effects of energy imbalance, foam-surface nonuniformity, and 1 μm of ice roughness.

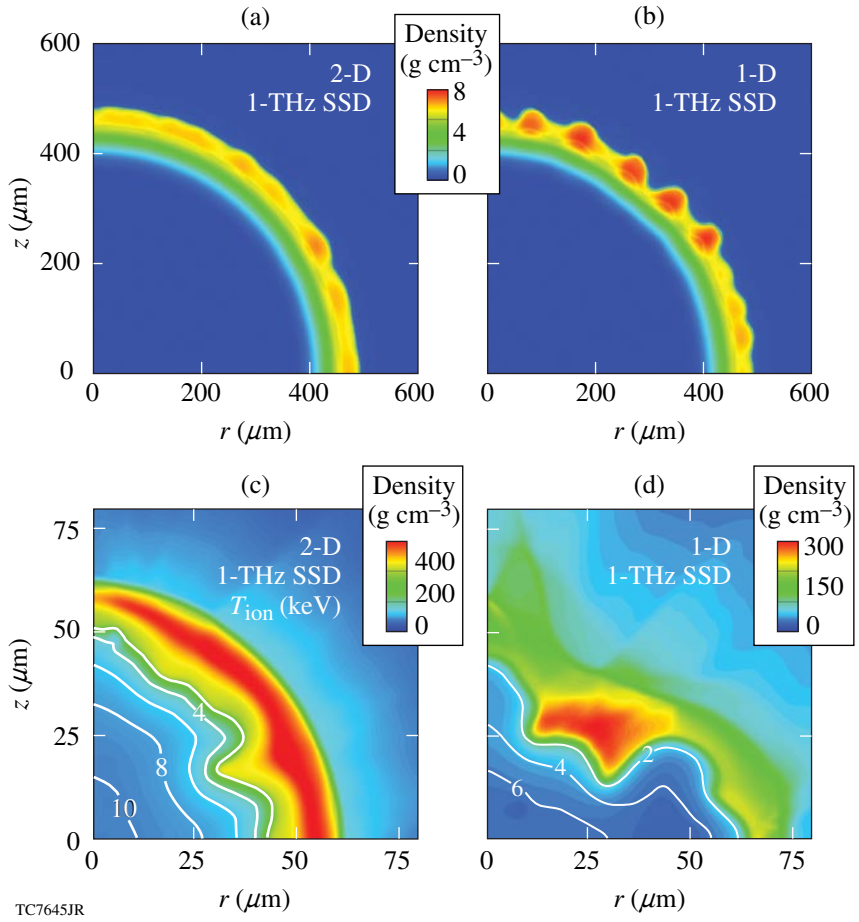

Figure 109.33
The shell is shown at the end of the acceleration phase [(a) and (b)] and near the time of peak compression [(c) and (d)] for the 2×1 and 2×0 SSD configurations, including all sources of nonuniformity. Unlike the integrated simulations shown in Fig. 109.32, these were run to completion. The high level of nonuniformity at the end of the acceleration phase and the highly distorted hot spot in the 2×0 case demonstrate the importance of 2-D SSD smoothing for target performance. The 2×1 simulation achieved a gain of 20, compared to a gain of less than 1 for the 2×0 case.

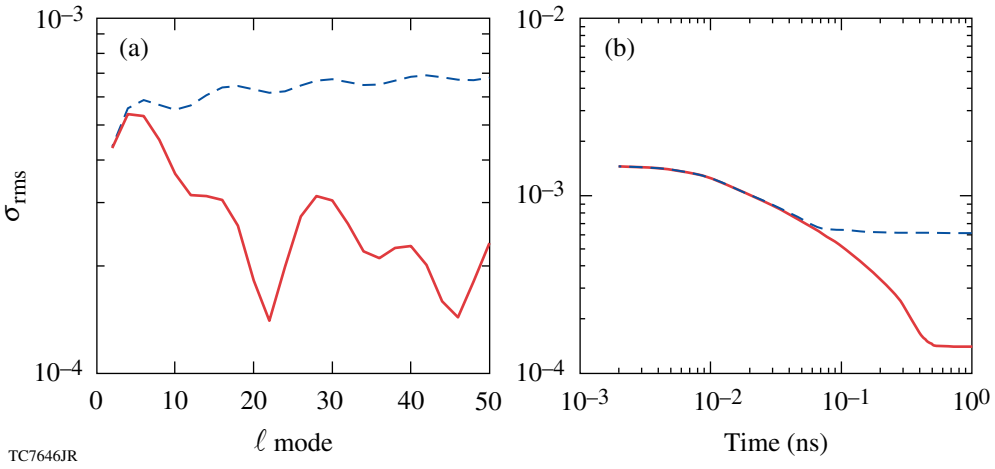

Figure 109.34
The smoothing due to SSD is shown in terms of (a) the mode number at 1 ns and (b) the perturbation for mode $\ell = 22$ as a function of time. Solid lines are 2-D SSD and dashed lines are 1-D SSD. These demonstrate the difference in the asymptotic level of smoothing for 1-D and 2-D SSD, as well as the level of smoothing for low mode numbers.

mode, the asymptotic level is reached at 70 ps for 1-D SSD and at 0.5 ns for 2-D SSD.

The third completed integrated simulation had the same nonuniformity levels and beam smoothing as the 2 × 1 just discussed, with an initial ice roughness of 1 μm and an ice power-law spectral index of $\beta = 1$. This was chosen to approximate the spectra of cryogenic DT capsules produced at LLE, which have less power in the low modes because of the different layering process. While the ice roughness was higher for this simulation than for the integrated 2-D SSD simulation described above, the lower power-law index reduces the spectral power in the low modes relative to the high modes. The combined effect is to produce a hot spot at peak compression, shown in Fig. 109.35, which is similar to that of the 2 × 1 SSD integrated simulation shown in Fig. 109.33(c), although with a smaller and more distorted hot spot. The gain factor of this simulation was 27. This shows that, for a smaller power-law index, the target can tolerate a greater ice roughness with little reduction in gain.

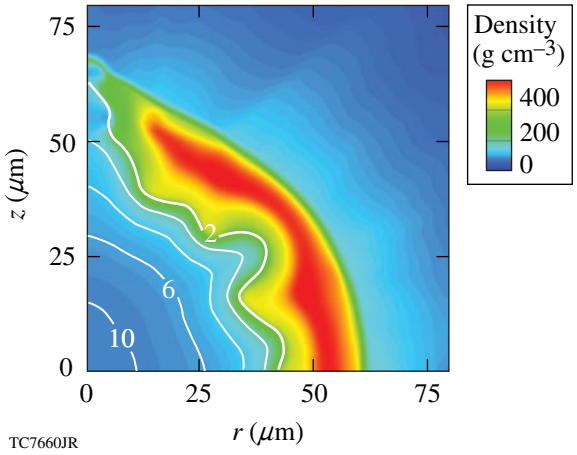

Figure 109.35
The shell is shown at peak compression for a simulation using 2-D, 2 × 1, 1-THz SSD with 1-μm initial ice roughness and an ice spectral index of 1. The resulting 2-D gain is 27.

Conclusions

An ignition target design using a wetted-foam ablator to couple greater laser energy into the target has been presented for use on the NIF with 1 MJ of incident laser energy. This design makes use of a thicker shell and lower implosion velocity to reduce the effects of imprint. A nonuniformity-budget analysis indicates that imprint, with 2-D, 2 × 1 color-cycle, 1-THz SSD smoothing, produces an effective nonuniformity $\overline{\sigma}$ that is slightly larger than that of the other sources of nonuniformity, namely, power imbalance, outer-surface roughness, and ice roughness. With 1 × 1 SSD the effective nonuniformity is more than twice that from other sources.

Simulations suggest that this design will ignite and achieve gain only if 2-D SSD is used to smooth single-beam illumination nonuniformities. The need for 2-D SSD has been found in other target-design performance studies as well.[17,36] Integrated simulations including imprint, surface and ice roughness, and beam-to-beam power imbalance were completed for two levels of SSD: 2 × 1 and 2 × 0, and 0.75-μm initial ice roughness with a power-law index of $\beta = 2$. The former achieved a gain of 32 compared to less than 1 for the latter. The difference in performance is due primarily to the difference in the asymptotic level of smoothing for 2-D and 1-D SSD. A third integrated simulation was completed using 1-μm initial ice roughness with a power-law index of $\beta = 1$, meant to approximate the ice spectra found in DT cryogenic targets at LLE. This simulation also ignited, achieving a gain factor of 27. This indicates that greater ice nonuniformity may be tolerated if combined with a smaller spectral index.

ACKNOWLEDGMENT

This work was supported by the U.S. Department of Energy Office of Inertial Confinement Fusion under Cooperative Agreement No. DE-FC52-92SF19460, the University of Rochester, and the New York State Energy Research and Development Authority. The support of DOE does not constitute an endorsement by DOE of the views expressed in this article.

REFERENCES

1. J. Paisner *et al.*, Laser Focus World **30**, 75 (1994).
2. J. Nuckolls *et al.*, Nature **239**, 139 (1972).
3. J. D. Lindl, Phys. Plasmas **2**, 3933 (1995).
4. S. Atzeni and J. Meyer-ter-Vehn, *The Physics of Inertial Fusion: Beam Plasma Interaction, Hydrodynamics, Hot Dense Matter*, International Series of Monographs on Physics (Clarendon Press, Oxford, 2004).
5. A. J. Martin, R. J. Simms, and R. B. Jacobs, J. Vac. Sci. Technol. A **6**, 1885 (1988); J. K. Hoffer and L. R. Foreman, Phys. Rev. Lett. **60**, 1310 (1988).
6. S. Skupsky, R. W. Short, T. Kessler, R. S. Craxton, S. Letzring, and J. M. Soures, J. Appl. Phys. **66**, 3456 (1989).
7. T. R. Boehly, V. A. Smalyuk, D. D. Meyerhofer, J. P. Knauer, D. K. Bradley, C. P. Verdon, and D. Kalantar, in *Laser Interaction and Related Plasma Phenomena*, edited by G. H. Miley and E. M. Campbell (American Institute of Physics, New York, 1997), Vol. 406, pp. 122–129.
8. Y. Lin, T. J. Kessler, and G. N. Lawrence, Opt. Lett. **20**, 764 (1995).

9. T. W. Johnston and J. M. Dawson, Phys. Fluids **16**, 722 (1973).

10. L. M. Hair *et al*., J. Vac. Sci. Technol. A **6**, 2559 (1988); R. A. Sacks and D. H. Darling, Nucl. Fusion **27**, 447 (1987).

11. D. G. Colombant *et al*., Phys. Plasmas **7**, 2046 (2000).

12. M. Tabak, *ICF Program Annual Report 1989 (U)*, Lawrence Livermore National Laboratory, Livermore, CA, UCRL-LR-116901-88/80, 141 (1989).

13. S. Skupsky, R. Betti, T. J. B. Collins, V. N. Goncharov, D. R. Harding, R. L. McCrory, P. W. McKenty, D. D. Meyerhofer, and R. P. J. Town, in *Inertial Fusion Sciences and Applications 2001*, edited by K. Tanaka, D. D. Meyerhofer, and J. Meyer-ter-Vehn (Elsevier, Paris, 2002), pp. 240–245.

14. J. D. Sethian *et al*., Nucl. Fusion **43**, 1693 (2003).

15. M. Desselberger *et al*., Phys. Rev. Lett. **74**, 2961 (1995).

16. P. B. Radha, V. N. Goncharov, T. J. B. Collins, J. A. Delettrez, Y. Elbaz, V. Yu. Glebov, R. L. Keck, D. E. Keller, J. P. Knauer, J. A. Marozas, F. J. Marshall, P. W. McKenty, D. D. Meyerhofer, S. P. Regan, T. C. Sangster, D. Shvarts, S. Skupsky, Y. Srebro, R. P. J. Town, and C. Stoeckl, Phys. Plasmas **12**, 032702 (2005).

17. P. W. McKenty, V. N. Goncharov, R. P. J. Town, S. Skupsky, R. Betti, and R. L. McCrory, Phys. Plasmas **8**, 2315 (2001).

18. G. Hazak *et al*., Phys. Plasmas **5**, 4357 (1998).

19. T. J. B. Collins, A. Poludnenko, A. Cunningham, and A. Frank, Phys. Plasmas **12**, 062705 (2005).

20. R. Betti, K. Anderson, T. R. Boehly, T. J. B. Collins, R. S. Craxton, J. A. Delettrez, D. H. Edgell, R. Epstein, V. Yu. Glebov, V. N. Goncharov, D. R. Harding, R. L. Keck, J. H. Kelly, J. P. Knauer, S. J. Loucks, J. A. Marozas, F. J. Marshall, A. V. Maximov, D. N. Maywar, R. L. McCrory, P. W. McKenty, D. D. Meyerhofer, J. Myatt, P. B. Radha, S. P. Regan, C. Ren, T. C. Sangster, W. Seka, S. Skupsky, A. A. Solodov, V. A. Smalyuk, J. M. Soures, C. Stoeck, W. Theobald, B. Yaakobi, C. Zhou, J. D. Zuegel, J. A. Frenje, C. K. Li, R. D. Petrasso, and F. H. Séguin, Plasma Phys. Control. Fusion **48**, B153 (2006).

21. V. N. Goncharov, P. McKenty, S. Skupsky, R. Betti, R. L. McCrory, and C. Cherfils-Clérouin, Phys. Plasmas **7**, 5118 (2000).

22. W. K. Levedahl and J. D. Lindl, Nucl. Fusion **37**, 165 (1997).

23. V. N. Goncharov, J. P. Knauer, P. W. McKenty, P. B. Radha, T. C. Sangster, S. Skupsky, R. Betti, R. L. McCrory, and D. D. Meyerhofer, Phys. Plasmas **10**, 1906 (2003); K. Anderson and R. Betti, Phys. Plasmas **10**, 4448 (2003).

24. K. Anderson and R. Betti, Phys. Plasmas **11**, 5 (2004); R. Betti, K. Anderson, J. Knauer, T. J. B. Collins, R. L. McCrory, P. W. McKenty, and S. Skupsky, Phys. Plasmas **12**, 042703 (2005).

25. T. J. B. Collins and S. Skupsky, Phys. Plasmas **9**, 275 (2002).

26. O. S. Jones *et al*., in *NIF Laser System Performance Ratings*, Supplement to Third Annual International Conference on Solid State Lasers for Application to Inertial Confinement Fusion (SPIE, Bellingham, WA, 1998), Vol. 3492, pp. 49–54.

27. V. N. Goncharov, S. Skupsky, P. W. McKenty, J. A. Delettrez, R. P. J. Town, and C. Cherfils-Clérouin, in *Inertial Fusion Sciences and Applications 99*, edited by C. Labaune, W. J. Hogan, and K. A. Tanaka (Elsevier, Paris, 2000), pp. 214–219.

28. R. Kishony and D. Shvarts, Phys. Plasmas **8**, 4925 (2001).

29. S. E. Bodner, J. Fusion Energy **1**, 221 (1981).

30. J. Hund and A. Nikroo, General Atomics, private communication (2006).

31. R. Epstein, T. J. B. Collins, J. A. Delettrez, V. N. Goncharov, J. P. Knauer, J. A. Marozas, P. W. McKenty, P. B. Radha, and V. A. Smalyuk, Bull. Am. Phys. Soc. **50**, 114 (2005).

32. V. N. Goncharov, S. Skupsky, T. R. Boehly, J. P. Knauer, P. McKenty, V. A. Smalyuk, R. P. J. Town, O. V. Gotchev, R. Betti, and D. D. Meyerhofer, Phys. Plasmas **7**, 2062 (2000).

33. R. Epstein, J. Appl. Phys. **82**, 2123 (1997).

34. J. E. Rothenberg, J. Opt. Soc. Am. B **14**, 1664 (1997).

35. S. Skupsky and R. S. Craxton, Phys. Plasmas **6**, 2157 (1999).

36. S. V. Weber, S. G. Glendinning, D. H. Kalantar, M. H. Key, B. A. Remington, J. E. Rothenberg, E. Wolfrum, C. P. Verdon, and J. P. Knauer, Phys. Plasmas **4**, 1978 (1997).

High-Intensity Laser Interactions with Mass-Limited Solid Targets and Implications for Fast-Ignition Experiments on OMEGA EP

Introduction

Picosecond laser–solid interaction at relativistic intensities has generated a high level of experimental[1–5] and theoretical[6–9] interest in recent years. This is due to its relevance to the fast-ignitior (FI) scheme for achieving inertial confinement fusion (ICF)[10,11] and to backlighter development for the x-ray radiography of dense materials.[12,13]

The interaction of high-intensity, $I \sim (10^{18}$ to $10^{21})$ W/cm^2, picosecond laser pulses with solid targets produces copious energetic electrons. Remarkable conversion efficiencies of up to 40% of the incident laser energy have been reported,[1,14] with characteristic electron energies ranging from ~100 keV up to several MeV.[14–16]

When these energetic electrons propagate into the bulk of a solid target, hard-x-ray bremsstrahlung and characteristic inner-shell line emission are produced [the first observations of K_α radiation from picosecond laser–produced plasmas were presented as early as 1979 (Ref. 17)]. The brightness of this radiation, either continuous or line emission, makes it valuable for x-ray radiography of ICF implosions, a primary motivation for the recent experiments of Theobald *et al.*, reported in Ref. 18. This article investigates, using semi-analytic and implicit-hybrid particle-in-cell (PIC) modeling,[19,20] the K-shell line emission from mass-limited targets and compares the predictions with these experiments.

The inner-shell line emission provides information on the energetic electrons produced in the interaction and its subsequent transport and heating of the target.[1,4,21–37] The main conclusion is that mass-limited targets of mid-Z elements provide an excellent "test bed" for FI physics due to simplifications afforded by the near-perfect hot-electron refluxing and by the effects on the line emission caused by the target heating.

Electron "refluxing" within the target, due to reflection from the surface sheath fields, is well known[9,28,29] and is connected to the generation of fast protons and ions.[30,31] When considering the generation of secondary radiation, this effect has not always been taken into account, e.g., Refs. 32–34. Unlike the case of proton acceleration,[9,28] the effect of hot electrons refluxing on the K-shell production efficiency has not been described, rather the emphasis has been placed on the energy dependence of the K-shell ionization cross section[34] and the competition with penetration depth and reabsorption of the characteristic radiation,[26,35] which is appropriate for massive targets.

It is shown here that the K-shell yields, per joule of hot electrons, of mass-limited targets are insensitive to the hot-electron spectrum and laser intensity. This is valid as long as the hot-electron stopping is classical and arises because of the energy dependence of the K-shell ionization cross section and electron range. It requires that relativistic corrections to the K-shell ionization cross section are accounted for.[36] The intensity dependence of K-shell production efficiency, expressed per joule of incident laser energy, is sensitive to the hot-electron conversion efficiency $\eta_{L\to e}(I)$. The experimental K_α yields from Ref. 18 are found to be consistent with the model if an intensity-independent hot-electron conversion efficiency of $\eta_{L\to e} = 10\%$ is assumed over the range $10^{18} < I < 10^{20}$ W/cm^2.

Volumetric heating of reduced-mass targets[18] is predicted to be sufficient that ionization of the copper M shell will strongly affect the ratio of K_β to K_α emission.[21] Three-dimensional *LSP* calculations,[19,20] including the relevant atomic processes,[27] have been performed for parameters of the RAL (Rutherford Appleton Laboratory) experiments and spatially resolved images of both K_α and K_β emission have been produced. It is shown that these measurements can be used to infer the degree of bulk heating and provide a *consistency check* on the hot-electron conversion efficiency obtained by fitting the absolute K_α-photon yields. A comparison between the predicted ratio of K_β- to K_α-photon production, for $\eta_{L\to e} = 10\%$, with the experimentally observed ratios is not conclusive. Rather, it suggests the usefulness of the technique, which will be pursued in future experiments on OMEGA EP currently under construction at LLE.[38]

The following sections (1) summarize the Theobald *et al.*[18] experiments, (2) describe a semi-analytic model for K-shell line emission in mass-limited targets, (3) compare the modeling pre-

dictions with the RAL experiments, (4) present the *LSP* calculations of volumetric heating, and (5) present the conclusions.

RAL PW and 100-TW Experiments

Pulses of 1.06-μm laser light from either the RAL Petawatt (PW) or the 100-TW Facility were focused with an *f*/3 off-axis parabola to ~10- to 100-μm spots onto Cu foil targets, achieving laser intensities between 3×10^{18} to 4×10^{20} W/cm^2. The foil thicknesses ranged between $d = 1$ to 75 μm, and the areas from $A = 0.01$ to 8.0 mm^2, resulting in target volumes of $V = 10^{-5}$ to 10^{-1} mm^3. The pulse durations ranged from 0.4 to 10 ps. Inner-shell emission and resonance-line emission occurred in these experiments. The K_α and K_β lines are emitted by the inner-shell transitions when an L- or M-shell electron fills a vacancy in the K shell, respectively, and the corresponding excess energy is radiated away by a photon in competition with Auger decay. Both x rays and energetic electrons may produce K-shell vacancies, assuming that the radiation has sufficient energy to excite above the K edge (for Cu, $h\nu > 9$ keV). Indirect inner-shell emission due to absorption of continuous x-ray radiation that is produced while suprathermal electrons decelerate in the target is negligible for elements with an atomic number $Z < 30$ (Refs. 37 and 39). Energetic electrons are the main contribution to K_α and K_β production in high-intensity, ultrashort, laser–solid interaction with low- and mid-Z materials.[24,26] X-ray spectra were collected, and the total number of K_α and K_β photons emitted, per unit laser energy, were obtained as described in Theobald *et al.*[18] The resonance-line emission is not discussed here.

In contrast with previous experiments using massive targets, absorption of the characteristic x rays is modest. As a result, the mechanism controlling the intensity dependence of the K_α yield is no longer the interplay between the electron penetration depth relative to the K-photon attenuation length as in earlier experiments.[26,40] A different model is required to predict the K-shell yield and its dependence on interaction parameters.

Description of a Semi-Analytic Model

The absolute K-shell photon yield N_k is the sum of the yield from two hot-electron populations: (1) electrons that escape from the target after losing only part of their energy (l), and (2) electrons that reflux, losing all of their energy to the target (r), i.e., $N_k = (N_k)_l + (N_k)_r$. The distinction is of significance only for targets thinner than the expected electron range in the material. For copper, this corresponds to targets thinner than a few millimeters for interaction intensities of ~10^{19} W/cm^2.

A simple estimate of the "refluxing efficiency," which is the ratio of the number of electrons stopped in the target to the total, $\eta_r = \left(N_e - N_l\right)/N_e$, can be given roughly by estimating the capacitance of the target. Assuming the target is a perfectly conducting thin disk in vacuum, $C = 8\,\epsilon_0 r \sim 70.8 \times 10^{-12}\,r$ farads, where r is the radius of the disk in meters, then a loss of $N_l = 4.42 \times 10^{11}$ (r/1 mm) (V/1 MV) electrons is required to produce a potential drop V in a target of radius r. This will be modified if the target is not isolated, for example, by a conducting target stalk. The required potential is determined self-consistently so that, for Boltzmann-distributed electrons at a temperature T, the potential satisfies $N_l = N_e \exp(-\mathrm{eV}/T)$. This leads to the equation $\exp(-\Phi) = \kappa\Phi$, where $\Phi = \mathrm{eV}/T$ and κ is given by $\kappa = 7.08 \times 10^{-2} rT^2/\left(\eta_{L\to e}\,E_L\right)$, where r is in mm, T is in MeV, and E_L is in joules. This can be solved for Φ, giving the refluxing efficiency $\eta_r = 1 - \exp(-\Phi)$, with the results for varying laser intensity and foil radius shown in Fig. 109.36. Note that the efficiency is extremely high for the parameters of the RAL experiments, $\eta_r > 90\%$.

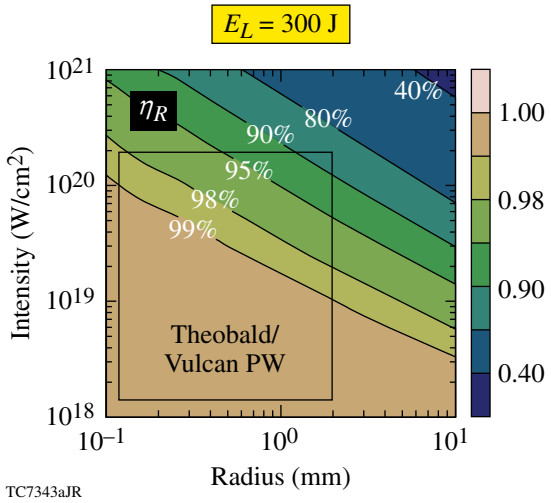

Figure 109.36
Refluxing efficiency obtained from the capacitance model. The hot-electron temperature is assumed to depend on laser intensity according to the ponderomotive scaling.[6]

The refluxing electrons are prevented from escaping by the self-consistent electromagnetic fields, so that the electron stopping can be treated as if the electrons were propagating in an infinite medium. The K-photon yield $(N_k)_r$ is computed by integrating along the path of electrons whose initial energies are described by an energy distribution $f(E_0)$ as long as (1) energy loss is accurately described with a continuous slowing-down formula ($\mathrm{d}E/\mathrm{d}s$), and (2) cold cross sections $\sigma_K(E)$ for K-shell ionization are appropriate (note that for copper $Z = 29$, only direct K-shell ionization is significant[37]). The contribution to the total yield N_k due to refluxing electrons $(N_k)_r$ is then given by

$$\left(N_k\right)_r = \left(\eta_r N_e\right)\int_0^\infty \mathrm{d}E_0 f\left(E_0\right)\int_{E_0}^0 \mathrm{d}E\omega_k n_{\mathrm{Cu}}\sigma_k\left(\frac{\mathrm{d}E}{\mathrm{d}s}\right)^{-1} \quad (1)$$

$$= \left(\eta_r N_e\right) n_{\mathrm{Cu}}\omega_k\int_0^\infty \mathrm{d}E_0 f\int_0^{s\left(E_0\right)} \mathrm{d}s\sigma_k\left[E\left(E_0,s\right)\right], \quad (2)$$

where N_e is the total number of hot electrons, ω_k is the fluorescence yield (ω_k = 0.44 for Cu)[41] (the fraction of K-ionization events resulting in K-quantum emission), and n_{Cu} is the number density of copper atoms in the target. The contribution from the "loss" electrons $(N_k)_l$ is similarly obtained to the above but by replacing η_r with $1–\eta_r$ and truncating the electron path length s in the integral Eq. (2) whenever it exceeds the target thickness $s\left(E_0\right) \rightarrow s_{\max} = \min\left[s\left(E_0\right), d\right]$ (if the target is thick enough so that multiple scattering is important, an accurate calculation of this term would require a Monte Carlo calculation). To distinguish between the K-emission lines, e.g., K_β, $K_{\alpha 1}$, $K_{\alpha 2}$, etc., of corresponding energies ϵ_{K_i} = 8.906, 8.048, and 8.028 keV, respectively, the relative emission probabilities p_i are introduced, defined according to $N_{K_i} = p_i N_k$, where "i" stands for either "β," "α_1," or "α_2." The probabilities are taken to be $p_a\left(= \Sigma_{i=\alpha_1,\alpha_2} p_i\right)$, p_β = 0.88, 0.12, respectively, whose values correspond to cold Cu at solid density.[42] From this model the electron-to-K-photon generation efficiency $\eta_{e\rightarrow k}$ is determined. This is defined as $E_k = \eta_{e\rightarrow k}E_e$, where the energy in electrons is given by $E_e = N_e\langle E_e\rangle$, and in K photons by $E_k = \epsilon_k N_k$. Here ϵ_k is the average fluorescence energy $\epsilon_K = \sum_i p_i\epsilon_{K_i}$ (8.14 keV for copper) and $\left\langle E_e\right\rangle = \int \mathrm{d}EEf(E)$ is the average electron energy, resulting in

$$\eta_{e\rightarrow k} = n_{\mathrm{Cu}}\omega_k\frac{\epsilon_k}{\left\langle E_e\right\rangle}$$

$$\times\left\{\eta_r\int_0^\infty \mathrm{d}E_0 f\left(E_0\right)\int_0^{s\left(E_0\right)} \mathrm{d}s\sigma_k\left[E\left(E_0,s\right)\right]\right.$$

$$\left.+\left(1-\eta_r\right)\int_0^\infty \mathrm{d}E_0 f\int_0^{s_{\max}} \mathrm{d}s\sigma_k\left[E\left(E_0,s\right)\right]\right\}. \quad (3)$$

A direct comparison between the experimental production efficiency (yield/laser joule) and the calculated generation efficiency is not straightforward. The experimentally observable quantity $N_{k,\mathrm{obs}}$ requires a knowledge of the detector solid angle, the filter, and detector efficiency.[18] Given this, the efficiency

$$\eta_{e\rightarrow k} = \frac{\epsilon_k\left(N_{k,\mathrm{obs}}/f_{\mathrm{abs}}\right)}{\eta_{L\rightarrow e}E_L} \quad (4)$$

may be computed only if the K-shell photon reabsorption fraction f_{abs} and the hot-electron production efficiency $\eta_{L\rightarrow e} = E_e/E_L$ are known. E_L is the energy in the laser pulse. The absorption fraction f_{abs} can be easily computed,[43] but the electron-production efficiency is subject to a great deal of uncertainty.[1] In principle, this could depend on many factors, $\eta_{L\rightarrow e} = \eta_{L\rightarrow e}(I_L, E_L, \nabla\log n, \ldots)$, where, for example, I_L is the laser intensity, E_L is the laser energy, and $\nabla\log n_e$ is the electron-plasma density scale length.[31,44] For current purposes it is either treated as a free "fitting" parameter, or taken to be a function of laser intensity only, with the dependence as given by Ref. 27, a fit to data obtained on the Nova Petawatt.[1] The predicted efficiency, obtained using Eq. (3), requires further specification of the hot-electron spectrum $f(E)$. Exponentially distributed electron energies are assumed, $f(E)\mathrm{d}E = (1/T)\exp(–E/T)\mathrm{d}E$, and the laser intensity connected to the temperature T, equal to the average energy for an exponential distribution, $\langle E\rangle = T$, using the "ponderomotive scaling" of Wilks,[6,45] $T = 0.511\left[\left(1 + I_{18}\lambda_{\mu\mathrm{m}}^2/1.37\right)^{1/2} - 1\right]$ MeV. Different intensity-temperature scalings have been proposed in the literature.[46,47] The calculations have also been performed with a relativistic Maxwellian (Jüttner) distribution,[48] leading to no change in the overall conclusions.

Equation (3), using ITS (Integrated Tiger Series) data for hot-electron stopping power and K-shell ionization cross sections,[49,50] the fluorescence probability, and the relative emission probabilities, taken together with the absorption fraction, the refluxing fraction, the hot-electron conversion efficiency, the hot-electron distribution function, and hot-electron temperature scaling as described in the text fully defines the model. From this the conversion efficiency of laser energy to K photons $\eta_{L\rightarrow k}$ can be computed with no free parameters.

Comparison Between the Modeling and RAL Experimental Results

Figure 109.37 shows K_α-photon yield, per joule of laser energy, as a function of laser intensity from the model described above with constant hot-electron conversion efficiencies of $\eta_{L\rightarrow e}$ = 10% and 20% (solid curves). The predicted K_α production efficiency is almost independent of laser intensity over the range $I = 2\times10^{18}$ to 2×10^{20} W/cm^2 and takes the value $(\eta_{L\rightarrow k})_{\mathrm{model}} \sim 4\times10^{-4}$ for $\eta_{L\rightarrow e}$ = 10%. This is consistent with experimental data taken from shots with 200 to 500 J of laser energy on a 20-μm-thick target (black triangles). Although not the case in Fig. 109.38, the experimental data are usually corrected for absorption and not the model predictions. The independence of efficiency on hot-electron temperature (laser intensity) over the experimental range of intensities can

be understood if perfect refluxing is assumed: the number of K-shell photons per electron is essentially given by the product of the range $s_0 \equiv s(E_0) = \int_{E_0}^{0} dE(dE/ds)^{-1}$ and the probability of K-shell emission per unit path $\omega_k n_{Cu} \sigma_k(E_0)$ [Eq. (1)]. When normalized by E_0, this product is a very weak function of the electron energy, provided that the relativistic corrections to the cross section $\sigma_k(E)$ are properly taken into account.[51] If the refluxing is ignored, $\eta_r \to 0$, then the dashed curves result. The *LSP* predictions, shown as circles in Fig. 109.37, are very similar to the semi-analytic model. This is to be expected because *LSP* uses the same cross sections as the model and the stopping is found to be due to classical collisions and not anomalous mechanisms. The discrepancies are a result of the approximations in the *LSP* collision model.[20]

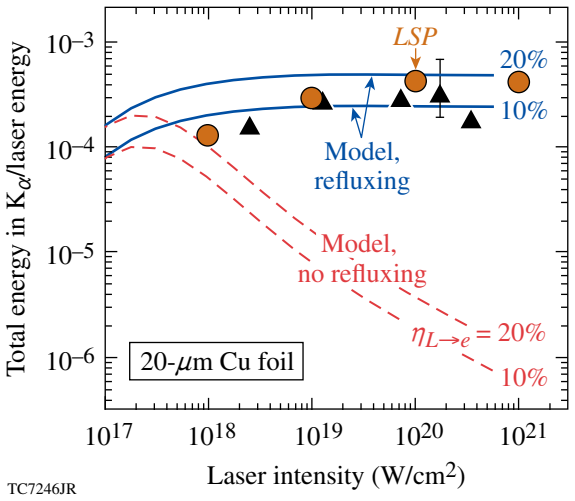

Figure 109.37
K_α production efficiency versus laser intensity for 20-μm-thick foils. The semi-analytic model with refluxing and a 10% hot-electron conversion efficiency (lower solid line) agrees with the *LSP* calculation (circles) and the experimental data (triangles). Also shown are the model predictions with no refluxing (dashed lines). The predictions, and not the data, have been corrected for reabsorption in the target.

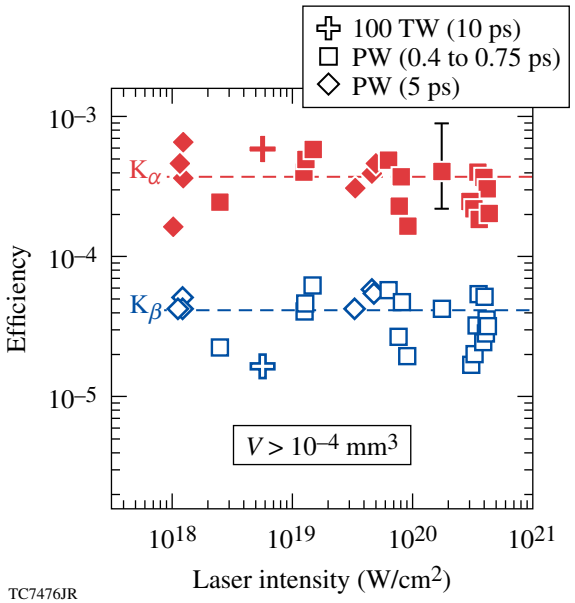

Figure 109.38
Experimental K_α (solid markers) and K_β (open markers) production efficiency as a function of laser intensity for both the 100-TW laser system (crosses) and the PW laser for short pulses (squares) and long pulses (diamonds). Only targets having a volume greater than 10^{-4} mm^3 are shown.

Agreement can be obtained only for high refluxing efficiency, $\eta_r \sim 100\%$, leading to the broad conclusion that reduced-mass targets produce the same number of K photons as targets of infinite thickness (but without the reabsorption). It follows that the K-shell yield is independent of the target geometry (volume). As Fig. 109.38 shows, this is actually observed.

Figure 109.38 shows both the K_α- (solid markers) and K_β-photon production efficiencies (open markers) from both the 100-TW system (crosses) and the RAL PW (squares and diamonds) as a function of laser intensity for a range of target geometries having volumes $10^{-4} < V < 10^{0}$ mm^3. (The target thicknesses employed were 20 μm for the 100-TW shots, 5 to 75 μm for the PW shots with 5-ps pulses, and 5 to 25 μm for the PW shots with 0.4- to 0.75-ps pulses.) The yields are essentially constant and the ratio of K_β/K_α is consistent with the expected cold matter value $N_{K_\beta}/N_{K_\alpha} = 0.14$. The predictions of the semi-analytic model with $\eta_{L\to e} = 10\%$ are shown as dashed lines.

A hot-electron conversion efficiency of 10% is lower than the $\eta_{L\to e} \sim (20\%–40\%)$ quoted in the literature for these intensities, e.g., in Ref. 15. Reference 1 suggests that the conversion efficiency $\eta_{L\to e}$ rises significantly with laser intensity with efficiencies of $\eta_{L\to e} \sim 40\%$ for laser intensities of 10^{20} W/cm^2. Figure 109.39 shows the predicted K_α yield from the model as a function of laser intensity when the functional form of $\eta_{L\to e}$ is fit to the Nova PW data.[1,27] The solid lines are lines of constant conversion efficiency $\eta_{L\to e}$ and the shaded area, bounded by the dashed curves, is the prediction of the model with a reasonable allowance made for scatter in the data of Ref. 1. With the conversion efficiency prescribed in this way, there are no free parameters in the model.

The discrepancy between the simple model and the experiment at high, $I \gtrsim 1 \times 10^{19}$ W/cm^2, and low, $I \sim 10^{18}$ W/cm^2, intensities might have several causes. Additional energy-loss

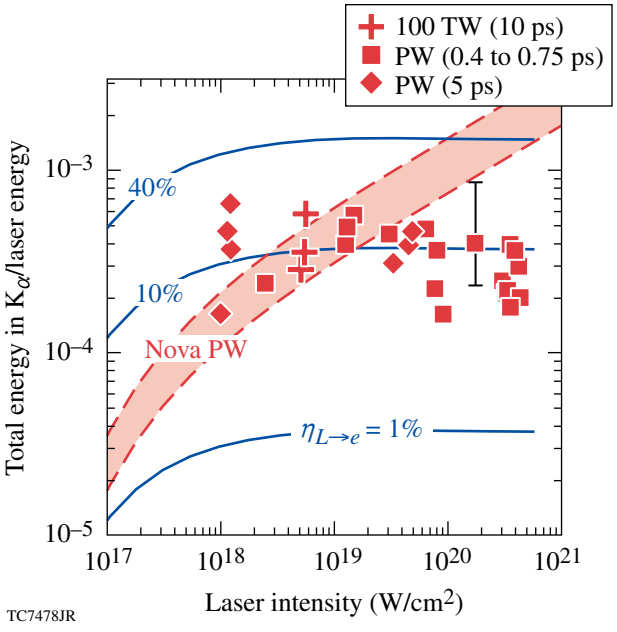

Figure 109.39
Experimental K_α production efficiency from the 100-TW system (crosses) and PW laser system with short pulses (squares) and long pulses (diamonds) as a function of laser intensity. The predictions of the semi-analytic model with hot-electron conversion efficiencies taken from a fit to Nova PW data are indicated by the shaded area bounded by dashed lines. The solid curves are lines of constant hot-electron conversion efficiency.

channels for the hot electrons such as the acceleration of protons (or ions) from the back side of the target, "anomalous" stopping mechanisms such as resistive inhibition,[52] or current filamentation instabilities, presumably becoming more important at higher intensities[9] are potential candidates. Large magnetic fields could bottle energy up at the surface,[53] where the plasma is too hot to produce K photons.

An experimentally verifiable consistency check on the inferred hot-electron conversion efficiencies, computed by fitting the absolute K_α yields, can be made by considering the volumetric heating created by the hot electrons. The collisional dissipation of the fast electrons, or the return current of the slower electrons, will volumetrically heat the foil on the picosecond time scale. The heating on this time scale, the same time scale as the K-shell emission, can be due only to the hot electrons and will be a measure of their energy content. The target heating can be quantified by measuring the ratio of K_β to K_α emission N_{K_β}/N_{K_α} because for the expected temperature rise $T \gtrsim 100$ eV, significant ionization of the M shell is expected[21] (Fig. 109.40). Smaller-mass targets are expected to achieve higher temperatures since an equal amount of energy is deposited in a smaller volume.[21]

Figure 109.40 shows the ionization degree Z^* for solid-density copper as a function of temperature according to the Thomas–Fermi model.[54] The main part of the figure shows an estimate of the line ratio as a function of temperature based on this ionization (the cold ratio has been weighted by the relative population of the M shell). It is not straightforward to estimate the ratio of the absolute K_α and K_β yields because the heating rate is a function of time and space, as is the hot-electron population. To take this properly into account we have performed *LSP* calculations.

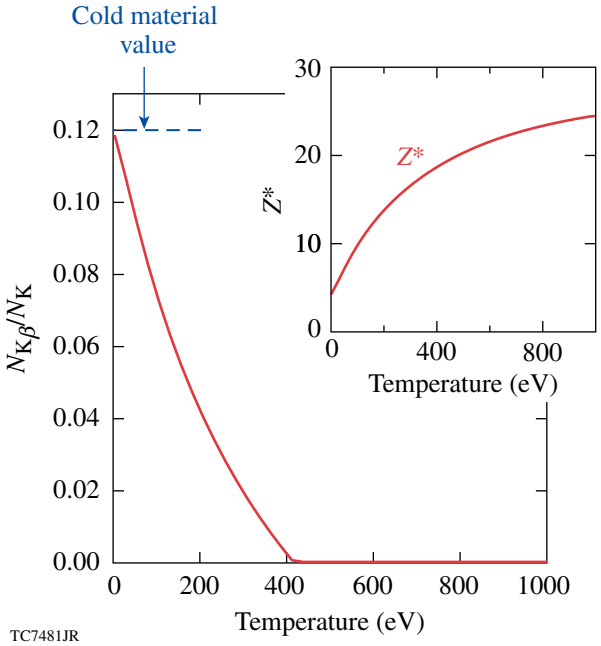

Figure 109.40
Reduction in the ratio of K_β to total K-emission probability as a function of plasma temperature, based on the Thomas–Fermi average ionization state Z^* (inset).

LSP Calculations of Volumetric Target Heating

Three-dimensional numerical calculations of target heating and K-shell emission were performed using *LSP*.[19,20] The targets were square copper foils of either (80×80) μm^2 or (160×160) μm^2 area, and either 10 μm or 20 μm in thickness. The hot-electron source was prescribed, as is usual in MC and implicit-hybrid calculations.[26,53] Electrons from the cold bulk were promoted in energy inside a region defined laterally by the laser spot and extending to a depth of 0.5 μm into the target. The rate of promotion was defined so that the power translated into the electrons was a constant fraction $\eta_{L\to e}$ of the assumed incident laser power. The energy spectrum of the promoted electrons was an isotropic Maxwellian with an average energy defined according to the local laser intensity on the surface of

the foil (assuming the ponderomotive scaling). A realistic laser spot shape was assumed, taken from Ref. 55, where 50% of the energy is contained within a characteristic diameter, $a_0 \sim 16\ \mu$m. A radial temperature dependence of the hot electrons resulted from the assumed axial symmetry of the spot, similar to that of Ref. 26. The total injected hot-electron kinetic energy was taken to be either 10 or 30 J, with a pulse duration of 0.5 or 1.5 ps, respectively. This held the average laser intensity over the central spot constant at $I = 1.2 \times 10^{19}$ W/cm^2. The total duration of the simulations was 15 ps and the targets were either 10 or 20 μm thick. Inter- and intra-species collisions are included in the calculation,[19,20] the effect of which is to slow the hot particles and to heat the initially cold target. It was observed that ≳90% of the hot-electron energy was converted into thermal energy of the target primarily as a result of direct *e*–*e* collisions, with only a few percent being either lost or converted into electromagnetic-field energy.

Figure 109.41 shows the peak temperatures attained by 20-μm-thick targets that have been taken on a slice transverse to the target normal at a depth of 5 μm. In the left (right)-hand column, 10 (30) J of energy was introduced into hot electrons. The target volume was 1.28×10^{-4} (5.12×10^{-4}) mm^3 in the first (second) row. The smallest target reaches a peak temperature of ~500 eV, while the most massive ~100 eV. Only one quadrant of each foil was modeled, the remainder completed by assuming symmetry about the *x* and *y* axes. *LSP* assumes an ideal equation of state (EOS) for the various particle species. Here, the temperatures have been renormalized assuming a Thomas–Fermi EOS.

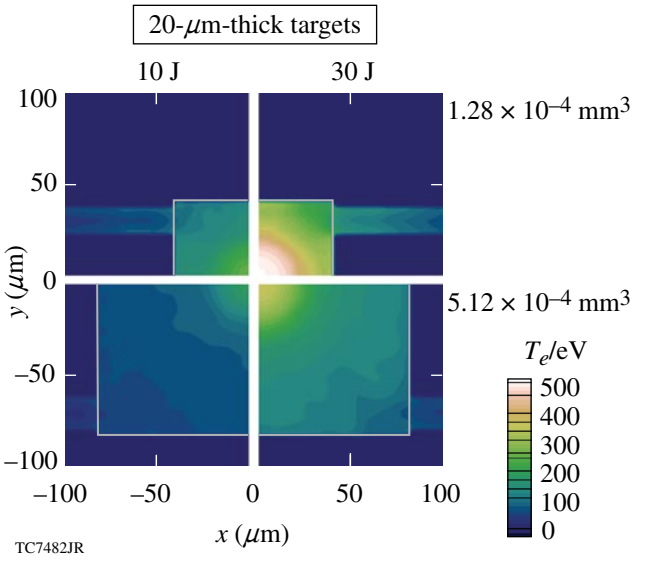

Figure 109.41
The images show target heating from four 3-D *LSP* calculations on a slice perpendicular to the target normal taken at a depth of 5 μm from the target surface. The heating was computed with 10 J and 30 J of energy in hot electrons (columns) and for target volumes of $V = 1.28 \times 10^{-4}$ and 5.12×10^{-4} mm^3 (rows). Only one quadrant of each foil was modeled, the remainder completed by assuming symmetry about the *x* and *y* axes.

1. Reasons for the Absence of Enhanced Stopping in the *LSP* Calculations

The stopping power of hot electrons can be increased above that due to particle collisions by the presence of resistive electric fields.[8,52] The current carried by the hot, laser-produced electrons far exceeds the Alfvén-limiting current for vacuum propagation, $I_A = 17\gamma_b\beta_b$kA,[56] where β_b is the beam velocity normalized to the speed of light, $\beta_b = v_b/c$, and γ_b is the relativistic gamma factor $\gamma_b = (1+\beta_b^2)^{-1/2}$. Estimating the current according to $I \sim \eta_{L\to e}\, eI_L A/T_{\rm hot} = 25$ MA for $I_L = 10^{19}$ W/cm^2, $A = \pi \times (20)^2\ \mu$m^2, $\eta_{L\to e} = 0.2$, and $T_{\rm hot} = 1$ MeV. This is several hundred times larger than the Alfvén limit $I_{\rm hot} \sim 560\left[2.7/(\gamma_b\beta_b)\right]I_A$.

Such beams cannot propagate unless there is a compensating return current. In metals and plasmas, the return current is naturally provided by cold electrons. The cold current represents a drag on the hot component through the resistive electric field $\vec{E} = \vec{j}/\sigma$, where σ is the electrical conductivity (assuming scalar conductivity and neglecting the Hall term). The resistive electric field $E \cong j/\sigma$ may be estimated to be ~2×10^5 kV/cm for the above parameters. This would stop a 1-MeV electron in ~50 μm. In making this estimate, a conductivity of $\sigma = 1 \times 10^6\ \Omega^{-1}$m^{-1} has been assumed. This value is representative of the minimum conductivity of copper (other mid-*Z* metals are similar). Typically this minimum occurs at a few 100 eV, thereafter increasing with temperature $\sigma \sim T_e^{3/2}$ according to the Spitzer value.

Resistive inhibition would be expected to be dominant, if the characteristic range due to the resistive electric field is small compared with the range due to binary collision events s_0. The range estimated above is shorter than the range in copper of $s_0 =$ 700 (3800) μm for 1.0 (5.0)-MeV electrons, respectively. In the current experiments, this is not the full story. In the thin-foil case, $d < s_0$, the "resistive" range should instead be compared with the foil thickness *d*. This is because refluxing hot electrons can contribute significantly to the return current for times greater than a hot-electron transit time. For this reason the *LSP* calculations indicate that resistive inhibition is not an important effect for the parameters of the experiments of Ref. 18. This is further borne out by the predictions of the semi-analytic model that are consistent with the usual stopping power.

Sources of plasma resistivity that are not currently modeled by *LSP*, such as ion-acoustic turbulence, possibly resulting from instability of the return current, have the potential to modify this picture. If the anomalous resistivity were to be a few times larger than the maximum resistivity quoted above, then the resistive range would become smaller than the typical target thickness. This could substantially reduce the contribution of hot electrons to the return current.

2. Effect of Target Heating on K-Shell Line Ratios

The effect of target heating on the relative emission probability of the K_β line has been estimated by adjusting the emission probability p_{K_β} in the *LSP* calculations, according to Fig. 109.40, using the local temperature at the time when the emission process took place. The *LSP* predictions for the line ratio N_{K_β}/N_{K_α}, for three target volumes and 10 (30) J of hot-electron energy, are shown by the light upper (dark lower) open diamonds in Fig. 109.42. Figure 109.42 also shows the experimentally determined ratio of K_β to K_α yield N_{K_β}/N_{K_α} from the RAL 100-TW (crosses) and RAL PW (squares, diamonds, and circles) as a function of target volume.

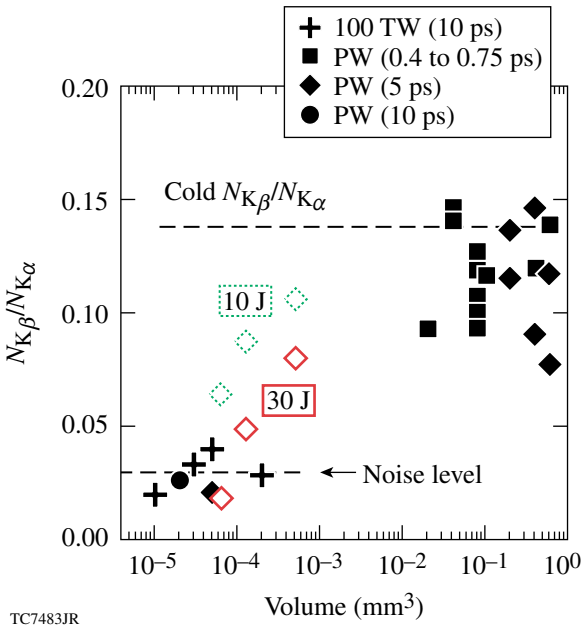

Figure 109.42
Experimental ratio of K_β to K_α yield N_{K_β}/N_{K_α} from the RAL 100-TW (crosses) and RAL PW (squares, diamonds, and circles) as a function of target volume. The open diamonds show *LSP* predictions in the cases of 10 J of energy in hot electrons (upper light) and 30 J (lower dark).

The scatter in the experimental data is too large for the consistency check to be conclusive, especially considering that the experimental K_β signals, for target volumes $V \lesssim 10^{-4}$ mm, are very close to the noise level of the detector at ~3%. It can be said, however, that the PW data are not inconsistent with a hot-electron conversion efficiency of 10%. For example, the close agreement of the 30-J calculations with the experimental data point (shot 5021803) at $V = 5 \times 10^{-5}$ mm^3, where the energy in the central spot was ~150 J.

3. Spatially Resolved K-Shell Emission

The spatial distribution of the K-shell emission reflects the trajectories of the hot electrons[57] and also the volumetric heating profile. Although the K-shell emission was not imaged in Ref. 18, images of the K_α emission from the *LSP* calculation can be produced (Fig. 109.43).

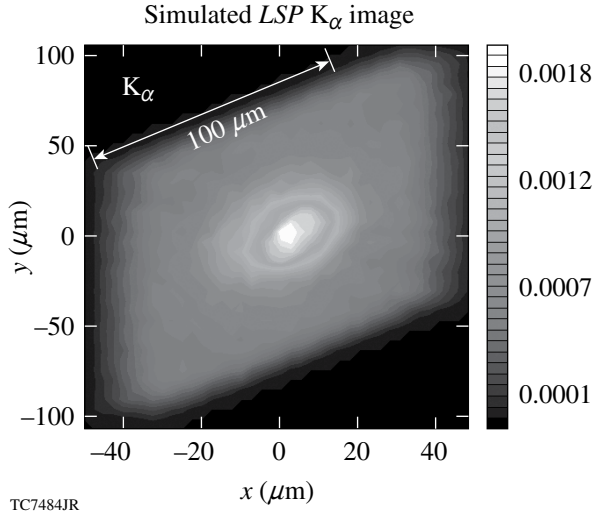

Figure 109.43
Image of K_α emission obtained from 3-D *LSP* calculations.

Conclusions

A semi-analytic model has been developed, and implicit-hybrid particle-in-cell code simulations (*LSP*)[19,20] have been performed to study fast-electron propagation, inner-shell x-ray photon production, and heating of mid-*Z*, mass-limited targets.

For the conditions considered, motivated by RAL experiments,[18] hot-electron flow within the target is dominated by refluxing at the electrostatic sheath at the target surface. This effect is responsible for the observed absolute x-ray yield. The semi-analytic model has been used to demonstrate the insensitivity of the yield to target geometry and hot-electron temperature under the conditions of hot-electron refluxing and classical stopping.

The experimental K_α yields are consistent between both models and experiment for an intensity-independent electron

conversion efficiency of ~10%. This result raises some concerns since 15% to 50% conversion efficiencies have been reported in the literature, e.g., Refs. 1, 6, 7, and 15. Surface fields[18] or anomalous stopping mechanisms, e.g., Ref. 58, might prevent hot electrons from penetrating to the cold interior of the target where they can efficiently produce K_α photons. If this were the case, a higher hot-electron conversion efficiency would be required to produce the observed K_α yields.[18] Target expansion is not a likely explanation for the discrepancy because it is responsible for only a few-percent decrease in the target density over the period of K_α emission. The ratio of K_β to K_α line emission is related to the degree of target heating that may be used as a consistency check on the hot-electron conversion efficiency.

Three-dimensional *LSP* calculations of volumetric target heating have been performed giving predictions for line ratios as a function of hot-electron conversion efficiency. At present, the experimental data set is not sufficiently precise to conclusively choose between the predictions; however, it does suggest the usefulness of the technique, which will be pursued in future experiments on OMEGA EP.

ACKNOWLEDGMENT

This work was supported by the U.S. Department of Energy Office of Inertial Confinement Fusion under Cooperative Agreement No. DE-FC52-92SF19460, the University of Rochester, and the New York State Energy Research and Development Authority. The support of DOE does not constitute an endorsement by DOE of the views expressed in this article.

REFERENCES

1. M. H. Key, M. D. Cable, T. E. Cowan, K. G. Estabrook, B. A. Hammel, S. P. Hatchett, E. A. Henry, D. E. Hinkel, J. D. Kilkenny, J. A. Koch, W. L. Kruer, A. B. Langdon, B. F. Lasinski, R. W. Lee, B. J. MacGowan, A. MacKinnon, J. D. Moody, M. J. Moran, A. A. Offenberger, D. M. Pennington, M. D. Perry, T. J. Phillips, T. C. Sangster, M. S. Singh, M. A. Stoyer, M. Tabak, G. L. Tietbohl, M. Tsukamoto, K. Wharton, and S. C. Wilks, Phys. Plasmas **5**, 1966 (1998).
2. P. A. Norreys *et al*., Phys. Plasmas **6**, 2150 (1999).
3. K. A. Tanaka *et al*., Phys. Plasmas **7**, 2014 (2000).
4. J. A. Koch *et al*., Phys. Rev. E **65**, 016410 (2001).
5. R. B. Stephens *et al*., Phys. Rev. E **69**, 066414 (2004).
6. S. C. Wilks *et al*., Phys. Rev. Lett. **69**, 1383 (1992).
7. B. F. Lasinski *et al*., Phys. Plasmas **6**, 2041 (1999).
8. L. Gremillet *et al*., Phys. Plasmas **9**, 941 (2002).
9. Y. Sentoku *et al*., Phys. Rev. Lett. **90**, 155001 (2003).
10. M. Tabak *et al*., Phys. Plasmas **1**, 1626 (1994).
11. N. G. Basov, S. Yu. Gus'kov, and L. P. Feokistov, J. Sov. Laser Res. **13**, 396 (1992).
12. O. L. Landen *et al*., Rev. Sci. Instrum. **72**, 627 (2001).
13. H.-S. Park *et al*., Rev. Sci. Instrum. **75**, 4048 (2004).
14. K. Yasuike *et al*., Rev. Sci. Instrum. **72**, 1236 (2001).
15. K. B. Wharton *et al*., Phys. Rev. Lett. **81**, 822 (1998).
16. R. Kodama *et al*., Phys. Plasmas **8**, 2268 (2001).
17. J. D. Hares *et al*., Phys. Rev. Lett. **42**, 1216 (1979).
18. W. Theobald, K. Akli, R. Clarke, J. Delettrez, R. R. Freeman, S. Glenzer, J. Green, G. Gregori, R. Heathcote, N. Izumi, J. A. King, J. A. Koch, J. Kuba, K. Lancaster, A. J. MacKinnon, M. Key, C. Mileham, J. Myatt, D. Neely, P. A. Norreys, H.-S. Park, J. Pasley, P. Patel, S. P. Regan, H. Sawada, R. Shepherd, R. Snavely, R. B. Stephens, C. Stoeckl, M. Storm, B. Zhang, and T. C. Sangster, Phys. Plasmas **13**, 043102 (2006).
19. D. R. Welch *et al*., Nucl. Instrum. Methods Phys. Res. A **464**, 134 (2001).
20. D. R. Welch *et al*., Phys. Plasmas **13**, 063105 (2006).
21. G. Gregori *et al*., Contrib. Plasma Phys. **45**, 284 (2005).
22. F. Pisani *et al*., Phys. Rev. E **62**, R5927 (2000).
23. E. Martinolli *et al*., Phys. Rev. E **73**, 046402 (2006).
24. H. Chen, B. Soom, B. Yaakobi, S. Uchida, and D. D. Meyerhofer, Phys. Rev. Lett. **70**, 3431 (1993).
25. A. Rousse *et al*., Phys. Rev. E **50**, 2200 (1994).
26. D. C. Eder *et al*., Appl. Phys. B **70**, 211 (2000).
27. R. P. J. Town *et al*., Nucl. Instrum. Methods Phys. Res. A **544**, 61 (2005).
28. A. J. Mackinnion *et al*., Phys. Rev. Lett. **88**, 215006 (2002).
29. H. Chen and S. C. Wilks, Laser Part. Beams **23**, 411 (2005).
30. S. P. Hatchett, C. G. Brown, T. E. Cowan, E. A. Henry, J. S. Johnson, M. H. Key, J. A. Koch, A. B. Langdon, B. F. Lasinski, R. W. Lee, A. J. MacKinnon, D. M. Pennington, M. D. Perry, T. W. Phillips, M. Roth, T. C. Sangster, M. S. Singh, R. A. Snavely, M. A. Stoyer, S. C. Wilks, and K. Yasuike, Phys. Plasmas **7**, 2076 (2000).
31. R. A. Snavely, M. H. Key, S. P. Hatchett, T. E. Cowan, M. Roth, T. W. Phillips, M. A. Stoyer, E. A. Henry, T. C. Sangster, M. S. Singh, S. C. Wilks, A. MacKinnon, A. Offenberger, D. M. Pennington, K. Yasuike, A. B. Langdon, B. F. Lasinski, J. Johnson, M. D. Perry, and E. M. Campbell, Phys. Rev. Lett. **85**, 2945 (2000).
32. U. Teubner, I. Uschmann, P. Gibbon, D. Altenbernd, E. Föster, T. Feurer, W. Theobald, R. Sauerbrey, G. Hirst, M. H. Key, J. Lister, and D. Neely, Phys. Rev. E **54**, 4167 (1996).
33. D. Salzmann *et al*., Phys. Rev. E **65**, 036402 (2002).

34. F. Ewald, H. Schwoerer, and R. Sauerbrey, Europhys. Lett. **60**, 710 (2002).

35. Ch. Reich *et al*., Phys. Rev. Lett. **84**, 4846 (2000).

36. H. Kolbenstvedt, J. Appl. Phys. **38**, 4785 (1967).

37. M. Green, Solid-State Electron. **3**, 314 (1961).

38. C. Stoeckl, J. A. Delettrez, J. H. Kelly, T. J. Kessler, B. E. Kruschwitz, S. J. Loucks, R. L. McCrory, D. D. Meyerhofer, D. N. Maywar, S. F. B. Morse, J. Myatt, A. L. Rigatti, L. J. Waxer, J. D. Zuegel, and R. B. Stephens, Fusion Sci. Technol. **49**, 367 (2006).

39. M. Green and V. E. Cosslett, J. Phys. D **1**, 425 (1968).

40. T. Feurer, W. Theobald, R. Sauerbrey, I. Uschmann, D. Altenbernd, U. Teubner, P. Gibbon, E. Förster, G. Malka, and J. L. Miquel, Phys. Rev. E **56**, 4608 (1997).

41. W. Bambynek *et al*., Rev. Mod. Phys. **44**, 716 (1972).

42. S. M. Seltzer, in *Monte Carlo Transport of Electrons and Photons*, edited by T. M. Jenkins, W. R. Nelson, and A. Rindi (Plenum Press, New York, 1988), Chap. 7, pp. 153–181.

43. Assuming that the hot-electron density within the foil is uniform, we can estimate the absorption fraction by $f_{\text{abs}} = (L_a/d)\left[1 - \exp\left(-d/L_a\right)\right]$ with the linear attenuation length $L_a = 22.3$ μm for K_α photons.

44. M. I. K. Santala *et al*., Phys. Rev. Lett. **84**, 1459 (2000).

45. G. Malka and J. L. Miquel, Phys. Rev. Lett. **77**, 75 (1996).

46. D. W. Forslund, J. M. Kindel, and K. Lee, Phys. Rev. Lett. **39**, 284 (1977).

47. F. N. Beg *et al*., Phys. Plasmas **4**, 447 (1997).

48. F. Juettner, Ann. Phys. **34**, 856 (1911).

49. M. J. Berger, in *Methods in Computational Physics: Advances in Research and Applications*, edited by B. Alder, S. Fernbach, and M. Rotenberg, Volume 1: Statistical Physics (Academic Press, New York, 1963), pp. 135–215.

50. The total K-shell ionization cross section is from Ref. 36, and, unlike the cross section in Refs. 37 and 39, it is good for relativistic electron energies.

51. C. Hombourger, J. Phys. B, At. Mol. Opt. Phys. **31**, 3693 (1998).

52. A. R. Bell *et al*., Plasma Phys. Control. Fusion **39**, 653 (1997).

53. R. J. Mason, E. S. Dodd, and B. J. Albright, Phys. Rev. E **72**, 015401(R) (2005).

54. R. M. More, Adv. At. Mol. Phys. **21**, 305 (1985).

55. P. K. Patel, M. H. Key, A. J. Mackinnon, R. Berry, M. Borghesi, D. M. Chambers, H. Chen, R. Clarke, C. Damian, R. Eagleton, R. Freeman, S. Glenzer, G. Gregori, R. Heathcote, D. Hey, N. Izumi, S. Kar, J. King, A. Nikroo, A. Niles, H.-S. Park, J. Pasley, N. Patel, R. Shepherd, R. A. Snavely, D. Steinman, C. Stoeckl, M. Storm, W. Theobald, R. Town, R. Van Maren, S. C. Wilks, and B. Zhang, Plasma Phys. Control. Fusion **47**, B833 (2005).

56. H. Alfvén, Phys. Rev. A **55**, 425 (1939).

57. Ch. Reich *et al*., Phys. Rev. E **68**, 056408 (2003).

58. M. Honda, J. Meyer-ter-Vehn, and A. Pukhov, Phys. Rev. Lett. **85**, 2128 (2000).

Three-Dimensional Characterization of Spherical Cryogenic Targets Using Ray-Trace Analysis of Multiple Shadowgraph Views

Introduction

In the laser-driven direct-drive approach to inertial confinement fusion (ICF), energy from many individual high-power lasers is delivered to a spherical target, causing a spherically symmetric implosion.[1] The 60-beam, 30-kJ OMEGA Laser System[2] is used to study direct-drive ignition (DDI), where the laser energy is deposited directly onto the target. For indirect-drive ignition (IDI), the laser energy is directed onto a metal container (a *hohlraum*) surrounding the target, creating x rays that deposit the energy onto the target.[3,4] IDI is inherently less efficient than DDI but has less-restrictive symmetry requirements on the laser illumination.

Current designs for both DDI and IDI high-gain ICF targets require a layer of condensed hydrogen fuel that adheres to the inner surface of a spherical shell ablator. Photon energy delivered to the target ablates its outer surface, and the ablation pressure drives the fuel layer inward, compressing both it and the gaseous fuel at the target's center. The drive pressure is varied in time such that the fuel density is compressed by a factor of as much as 4000 while remaining relatively cold. Shock waves resulting from the drive-pressure history, along with compressive work, heat the gaseous-core "hot spot" to the high temperatures needed to initiate burning the fuel.

As the fuel layer is compressed and decelerates, perturbations on the inner ice surface act as amplitude seeds for the Rayleigh–Taylor instability[5,6] on the inner surface. The nonlinear growth of this deceleration-phase instability mixes the cold compressed fuel layer with the hot-spot fuel vapor, reducing fusion yield or preventing ignition.[7–10] Asymmetry-induced hydrodynamics can reduce the performance of ICF targets to well below that predicted by 1-D modeling.[11] Ignition requirements impose strong constraints on the illumination uniformity and on the sphericity of the target.[12]

The degrading effect of an inner-ice-surface perturbation on implosion performance depends on the perturbation's mode number, which is the ratio of the capsule's circumference to the wavelength of the perturbation. The surface roughness is characterized in terms of a mode spectrum analogous to Fourier analysis. Since the target geometry is spherical, spherical harmonics $Y_{\ell m}(\theta,\varphi)$ form the basis functions used for the mode spectrum. Accurate surface characterization of ice layers requires reliable measurement of the layer's surface with submicron resolution at many points distributed over the surface of a target. Hydrodynamic codes then calculate capsule implosion performance using the measured surface mode power spectrum. The benchmarking of calculated target performance with experimental results is essential for designing ignition-scale targets and specifying their allowable surface roughness with confidence.

The DDI specifications[12] for the National Ignition Facility (NIF)[13] require a total root-mean-square (rms) deviation of less than 1 μm for an ice layer with less than 0.25-μm rms from Fourier modes higher than $n = 10$. An ice-layer rms deviation of less than 1 μm is also required for successful IDI on the NIF.[14] Measurement of the ice-layer radius over the entire surface with submicron resolution is required to verify success or failure at achieving the required specifications.

This article describes the optical backlit shadowgraphic 3-D characterization of cryogenic direct-drive-target ice layers at LLE using ray-trace analysis of the shadowgrams. The following sections (1) briefly describe the principles and equipment used to record a cryogenic-target shadowgram at LLE; (2) analyze the resolution of shadowgram measurements; (3) describe three-dimensional ice-layer reconstruction from multiple target views using the conventional assumption that the shadowgram bright ring can be directly related to the ice thickness based on spherically symmetric calculations; and (4) present a shadowgram analysis to which nonspherically symmetric ray tracing is added, thereby improving the 3-D ice-layer reconstruction by self-consistently calculating the effects of ice-layer asymmetries and roughness on the position of the bright ring in each view. The conclusions are presented in the final section.

Shadowgraphic Characterization of Ice Layers

Optical backlit shadowgraphy is the primary diagnostic used to measure ICF target ice-layer roughness.[15–25] A shadow-

graph records the image of the light rays passing through a backlit target. The rays are reflected and refracted at the shell wall and ice-layer surfaces. Some rays are focused into characteristic rings. Ray-trace modeling of a typical cryogenic target using the *PEGASUS* code[26] has identified the specific reflections/refractions responsible for the brightest rings (see Fig. 109.44). The most-prominent ring or "bright ring" is the result of a single internal reflection off the inner solid/vapor interface of the ice layer. The position of the bright ring in the shadowgraph is directly correlated with the position of the inner surface of the ice layer and allows the nonuniformity of the inner surface to be characterized.

A high-magnification, high-fidelity backlit optical shadowgraphy system (see Fig. 109.45) is used to diagnose the ice-layer quality. A 627-nm red-light–emitting diode (LED) provides the backlighting. A 50- to 100-μs pulse drives the LED to illuminate (~*f*/5) the target. Imaging optics (~*f*/6) magnify the target image on a DALSA charge-coupled-device (CCD) camera (12 bit, 1024 × 1024) (Ref. 27) such that the camera typically images about 1.2 μm per pixel. The camera is triggered by the same pulse that drives the LED.

A sample shadowgram of an LLE cryogenic D_2 target suspended from a beryllium "C-mount" by four threads of spider silk is shown in Fig. 109.46. The strong unbroken bright ring and mostly featureless central spot are indicative of the high quality of this ice layer. Two inner rings are also clearly visible.

Resolution of Shadowgram Rings

The analysis of the target image in an individual shadowgram consists of accurately determining the target center, unwrapping the image into polar coordinates, and measuring the radial positions of both the target edge and the bright ring's peak intensity. Details of this procedure are published elsewhere.[21] Here, the accuracy and resolution of these measurements are discussed.

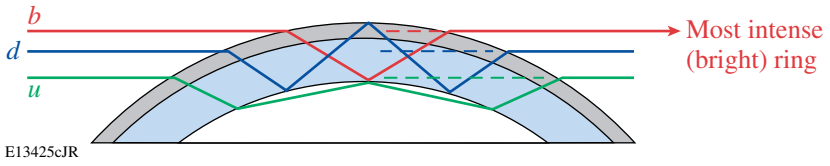

Figure 109.44
Ray-trace modeling of a cryogenic target has identified the sources of the most-intense rings. The bright ring (b) is by far the most intense.

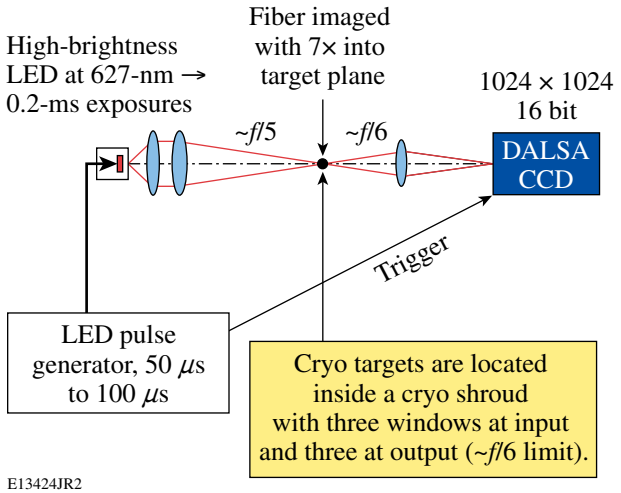

Figure 109.45
The LLE Cryogenic Target Characterization Stations are based on a diffuse *f*/5 source and *f*/6 imaging optics.

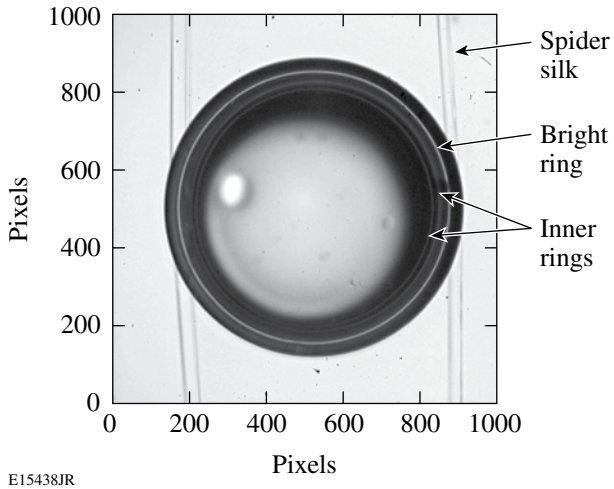

Figure 109.46
Shadowgraph of a cryogenic target (876-μm outer diameter, 4.2-μm shell thickness, 79-μm ice thickness) in a logarithmic scale. The fainter inner rings are clearly visible in the image. The bright-ring signal-to-noise ratio is typically over 20, and the effects of noise are reduced by the shadowgraph analysis routines.[21] The offset of the light rays passing through the center of the target is due to an asymmetry in the spread of the illumination, which has little effect on the position of the bright ring.

Previously, by examining the bright-ring-measurement scatter for very smooth liquid hydrogen layers,[21] the resolution of the measurements was estimated to be about 0.1 pixel (~0.12 μm). The high resolution of the bright-ring measurements has been verified using precision calibration targets as described here. The calibration targets are simulated target images of photolithographed chrome on glass.[28] A simulated image consists of a "perfectly" circular edge along with a bright ring (plus two fainter inner rings) with a known variation in radial position. The radial variation of the rings was calculated, using the linearized formula discussed in the next section, for an ice surface with a surface-deviation, Fourier-mode power spectrum of

$$P_n = Cn^{-2} \tag{1}$$

for Fourier modes n = 1 to 100, where C was chosen such that the spectrum meets the DDI specification. The phase of each Fourier mode was randomized. This power spectrum and the calculated bright-ring position are shown in Fig. 109.47. The precision calibration target was photolithographed with a manufacturing tolerance of 0.1 μm. A shadowgram of this target taken in one of OMEGA's Cryogenic Target Characterization Stations is shown in Fig. 109.48. This image has been analyzed using LLE's standard shadowgram analysis routines, and the results are shown in Fig. 109.47. The measured bright-ring positions have a mean error of less than 0.1 μm (within the manufacturing tolerances of the calibration target), and the total rms error of the ring measurement is about 0.01 μm.

It is clear that the bright-ring position can be very accurately measured in the characterization station shadowgrams. The relationship of that ring position with the radius of the actual ice surface producing the ring is discussed in the next section.

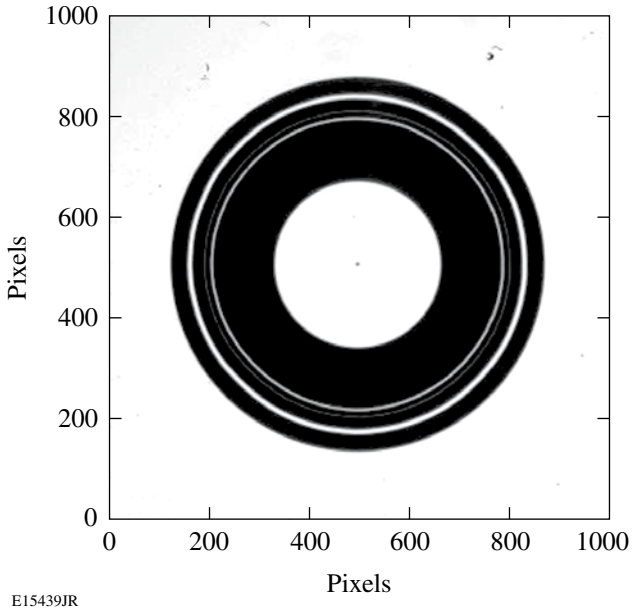

Figure 109.48
Shadowgraph of the photolithographed chrome-on-glass "dot-surrogate" target. The outer edge is a perfect circle to within the manufacturing tolerance (0.1 μm). The rings are simulated by uniform-thickness gaps in the dot. The inner rings are fainter than the bright ring because their gap width is less. The radial positions of the rings vary around the target and are calculated for an ice surface whose roughness meets the DDI requirements.

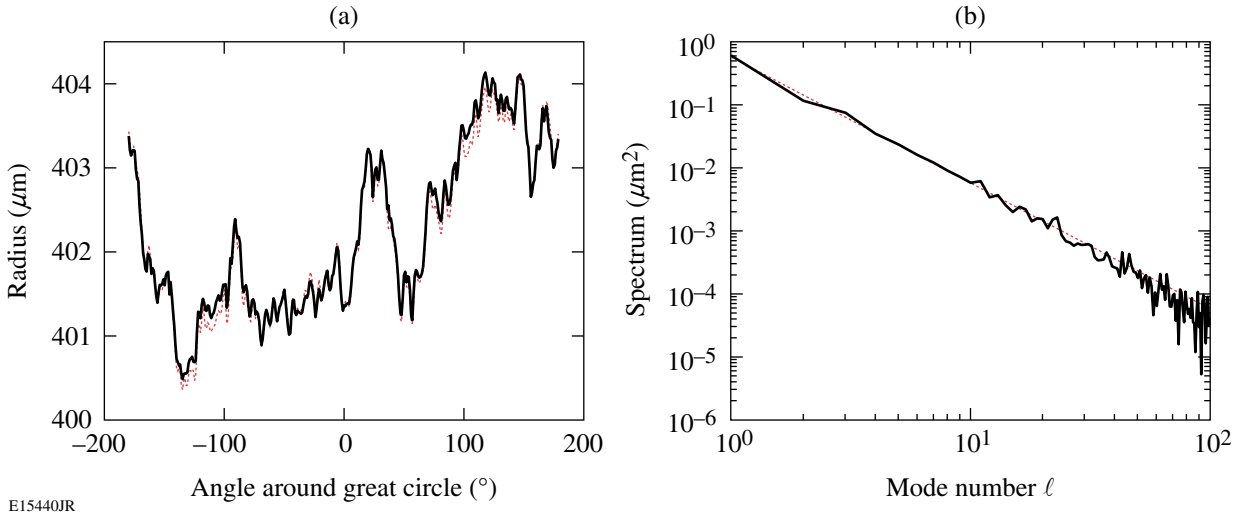

Figure 109.47
The measured (solid) bright ring for the simulated dot-surrogate target is an excellent match to the design specification (dotted) in terms of both (a) radial position and (b) power spectrum.

Three-Dimensional Ice-Layer Reconstruction Using Multiple Shadowgraph Views

An important feature of LLE's Cryogenic Target Shadowgraphy System is the use of multiple views of the target to fully characterize the ice surface. Multiple views allow a far-more-complete surface characterization than is possible from a single view. Even with three mutually orthogonal views, it can be shown that there is only a small chance of detecting many local ice defects.[29]

In the LLE Cryogenic Target Characterization Stations, the targets are rotated to provide a large number of different views for a single camera. The maximum number of views is limited only by the step size of the rotation stepper motor, which is a few tenths of a degree. Shadowgrams are typically recorded at 15° intervals, producing a total of 48 independent views between two cameras in each characterization station. The two cameras have approximately orthogonal views: one camera views the target center from an angle of 26.56° above the equator and the second camera, located 109.96° azimuthally from the first, views the target center from 12.72° above the equator. These view angles are determined by the location of the layering sphere windows that are aligned with the OMEGA target chamber's viewing ports, which are used to center the target at shot time. These views are not optimum for target characterization. An off-the-equator viewing angle always results in unviewable regions surrounding the rotation poles; these unviewable "polar caps" are apparent in Fig. 109.49(a).

The standard method of shadowgram analysis assumes that the ice surface position along a great circle perpendicular to the shadowgraph view can be uniquely determined from the observed bright-ring position for that view[17,22–25] by characterizing the ice-to-bright-ring relationship using a ray-trace study of spherically symmetric targets with varying ice thickness. At LLE, ray-trace modeling of a typical cryogenic target using the *PEGASUS* code[26] has identified how the shadowgram ring positions vary with the target parameters such as the shell outer radius and thickness, the D_2-ice thickness, the shell index of refraction, and the D_2 index of refraction. The *PEGASUS* code is two dimensional and assumes spherical symmetry in the target. A linearized formula derived from this modeling is used to determine the inner-ice-surface radius from the position of the bright ring for given target parameters.

A 3-D representation of the ice layer can be constructed from the ice-surface positions determined from the multiple shadowgram views. Figure 109.49 shows a target's inner ice surface reconstructed from a target rotation of 24 separate views. The surface is dominated by low-mode-number asymmetries, but very different Fourier modes are observed for any given great circle. For this data set, the ice-surface 1-D rms roughness of the individual great-circle observations varies from 2.6 μm to 5.3 μm with an average value of 3.5 μm. This particular data set was selected for the following reasons:

- The outer surface is very smooth and symmetric and should have little effect on the bright ring.
- The optical distortion from collection optics was well minimized for these images.
- The bright ring is smooth and has few breaks.

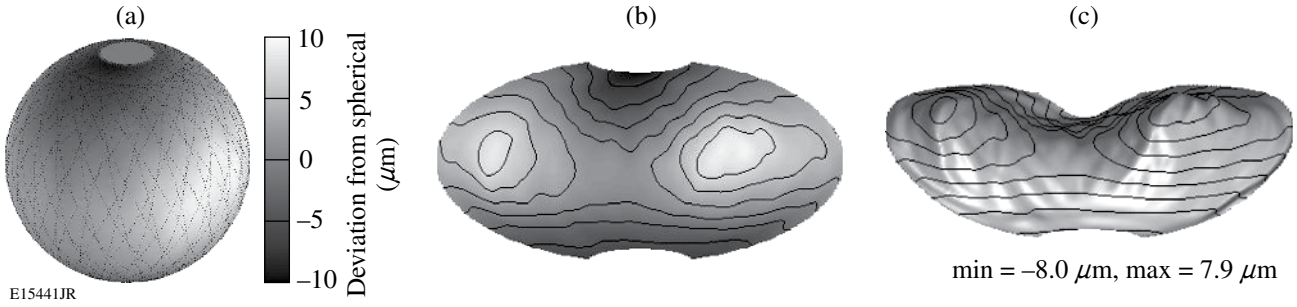

Figure 109.49
Three-dimensional representation of a cryogenic inner ice surface (μm) displayed (a) on a spherical surface, (b) using the Aitoff projection with contour lines, and (c) using the Aitoff projection with surface elevation. These displays are constructed by interpolating all the individual data from the many great-circle observations to an evenly spaced (θ,ϕ) surface grid. The dotted lines in (a) show the location of the actual great circles observed in the individual shadowgraphs. The "polar caps" crossed by none of the great-circle observations are clearly visible.

As mentioned earlier, computer modeling of a spherical implosion, including instability growth, requires an ice-roughness spectrum described in terms of spherical-harmonics-basis functions $Y_{\ell m}(\theta,\phi)$ on the ice surface:

$$R(\theta,\phi) = \sum_{\ell=0}^{\infty} \sum_{m=-\ell}^{\ell} A_{\ell m} Y_{\ell m}(\theta,\phi) \quad (\mu\text{m}). \tag{2}$$

This description gives a Legendre-mode power spectrum and total surface variance of

$$P_\ell = \frac{1}{4\pi} \sum_{m=-\ell}^{\ell} |A_{\ell m}|^2 \quad (\mu\text{m}), \tag{3}$$

$$\sigma_{\text{rms}}^2 = \sum_{\ell=1}^{\infty} P_\ell \quad (\mu\text{m}^2), \tag{4}$$

respectively. The P_ℓ spectrum represents an average over all azimuthal modes.

The P_ℓ spectrum for high mode numbers can be inferred from the Fourier power spectra of the many great circles observed. If one assumes that the surface perturbations are randomly distributed, the great-circle 1-D Fourier-mode power spectrum, averaged over many great circles, can be mapped[30] to an equivalent Legendre-mode power spectrum. The assumption of randomly distributed perturbations limits the applicability of the mapping to higher mode numbers. At LLE the ice-surface positions are directly fit to spherical harmonics to determine the lower mode numbers (up to some ℓ_{max}).[21]

The results of a direct $Y_{\ell m}(\theta,\phi)$ fit are shown in Figs. 109.50 and 109.51 for a fit up to $\ell_{\text{max}} = 10$. The surface reconstruction in Fig. 109.51 based on the low-mode-number fit is a good match to the data shown in Fig. 109.49. The Legendre power spectrum P_ℓ corresponding to this fit along with the higher mode numbers determined by the mapping method is displayed in Fig. 109.50. Target reconstructions using the standard analysis have successfully detected low-mode asymmetries in the ice layer, allowing the identification and correction of the sources of the layering sphere temperature isotherm asymmetries that cause them.[31]

The maximum mode number fit, ℓ_{max}, is limited by the largest space between sampled points on the surface. For typical LLE targets, the largest gap in the surface data occurs at the unviewable polar cap of the target. The maximum mode number that can be reliably fit is also reduced by the many smaller surface gaps between great-circle measurements, noise in the data, uneven surface weighting (sections crossed by several great circles are more heavily weighted), and the fact that the data do not agree

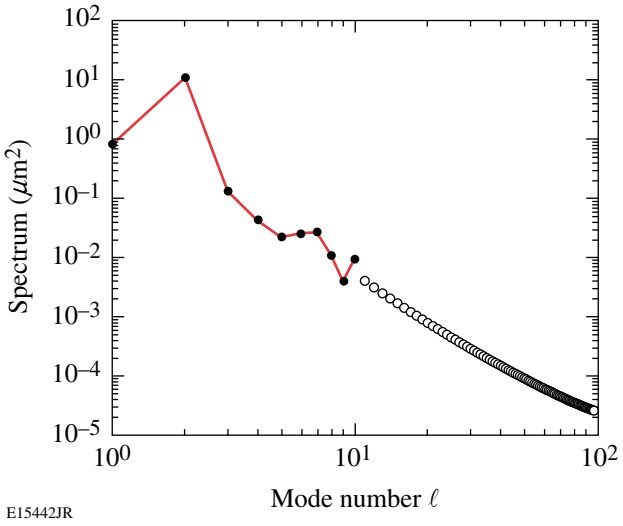

Figure 109.50
Legendre-mode power spectrum P_ℓ of the ice surface. The dots correspond to the low-mode-number (up to $\ell_{\text{max}} = 10$) direct fit. The circles result from mapping the average Fourier-mode spectrum of the many great circles.

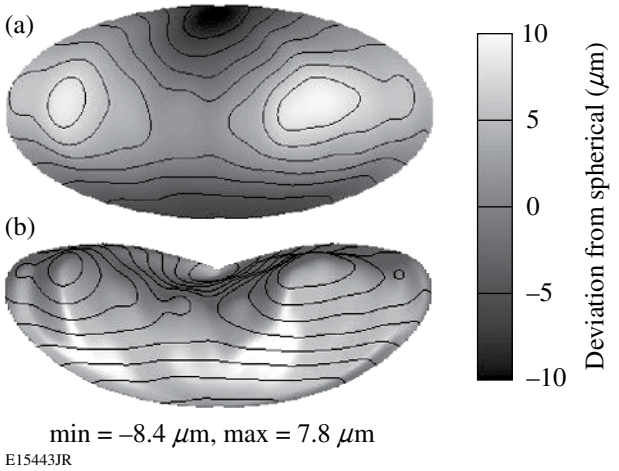

Figure 109.51
Three-dimensional reconstruction of a cryogenic inner ice surface (μm) based on a direct $Y_{\ell m}(\theta,\phi)$ fit to the measured data (up to $\ell_{\text{max}} = 10$) (a) using the Aitoff projection with contour lines and (b) using the Aitoff projection with surface elevation. A comparison with Fig. 109.49 shows that the low-mode features are well matched by the fit. Although the actual great-circle data are used in the fitting, the results are mapped to an evenly spaced (θ,ϕ) surface grid using the $Y_{\ell m}$ coefficients for better display.

at "cross-over" points (see the next section). The sum of these effects typically limits the direct surface fit to mode numbers up to about $\ell_{\text{max}} = 10$. The exact limit varies with each data set. The results of fitting too high an ℓ_{max} are shown in Figs. 109.52 and 109.53, where the fit has been extended to $\ell_{\text{max}} = 16$. The power spectrum in Fig. 109.52 is rising as mode numbers approach

ℓ_{max}, a trend not observed in the Fourier analysis of the bright rings. The combination of a too high ℓ_{max} along with the spaces between data circles and data mismatch at the great-circle cross-over points produces a fit with more structure than seen in the individual bright rings. This increased structure and "crinkling" are evident in Fig. 109.53.

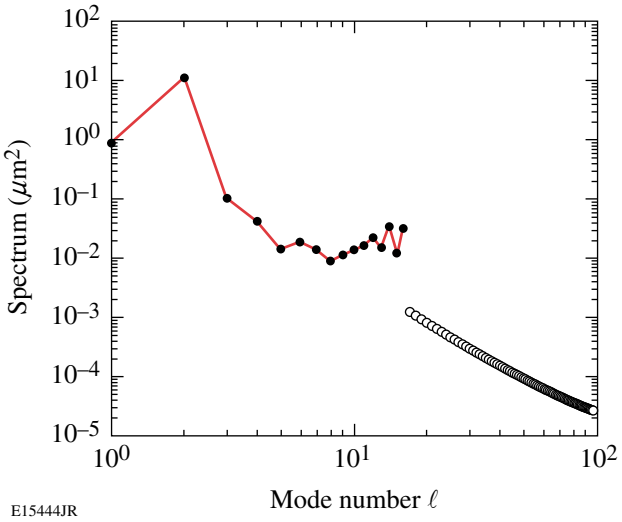

Figure 109.52
Legendre-mode power spectrum P_ℓ of the ice surface. The dots correspond to the low-mode-number (up to ℓ_{max} = 16) direct fit. The circles result from mapping the average Fourier-mode spectrum of the many great circles.

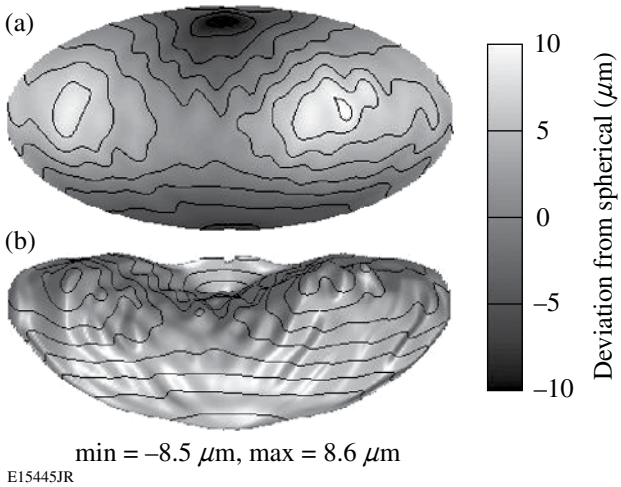

Figure 109.53
Three-dimensional reconstruction of a cryogenic inner ice surface (μm) based on a direct $Y_{\ell m}(\theta,\phi)$ fit to the measured data (up to ℓ_{max} = 16) (a) using the Aitoff projection with contour lines and (b) using the Aitoff projection with surface elevation. A comparison with Fig. 109.49 shows a large amount of mid-mode noise in the fit.

Ray-Trace Analysis

Despite the success of the standard analysis, it is well known[18–20,24] that the assumption that the ice-surface position along a great circle perpendicular to the shadowgraph view can be directly correlated to the observed bright-ring position for that view is valid only for perfectly spherical symmetry. Kozioziemski *et al.*[18] showed that a shift in the ice layer along the viewing axis will alter the bright-ring position and "significantly shift the apparent ice-layer thickness." This effect can be easily seen in Fig. 109.54, which shows the ray path of the bright ring for a target layer shifted along the viewing axis. For imperfect ice layers, Koch *et al.*[19,20] note that "correlation depends on the height and curvature of the imperfection." To illustrate this, the bright-ring radii predicted by 3-D ray tracing of a simulated ice surface constructed from spherical harmonics for opposing views are shown in Fig. 109.55. The predicted bright rings show general similarities in the low-mode structures but differ greatly in the higher-mode detail. This explains why the ice surfaces determined by the standard method do not agree at the cross-over points of the views.

If the shadowgrams were viewed along the equator and exactly opposing views could be measured, the average position of two bright rings would show a good correlation to the ice-surface position along the great circle perpendicular to the views.[32] In this case the standard method can accurately be applied to the averaged bright ring. If one has nonequatorial views, exactly opposing views cannot be recorded. A study of two above-the-equator views in the Cryogenic Target Characterization Stations for OMEGA rotated 180° about the polar

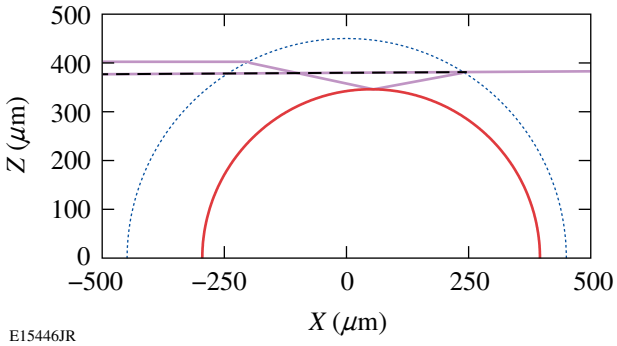

Figure 109.54
The ray path that produces the bright ring in a target where the ice surface is shifted along the line of view shows how asymmetries affect the bright ring. When viewed from the right, the bright ring appears lower than when viewed from the left. The standard analysis would determine a quite-different ice thickness for each view. For an unshifted layer, the rays on both sides would be at the same height and the bright ring would appear the same for both views.

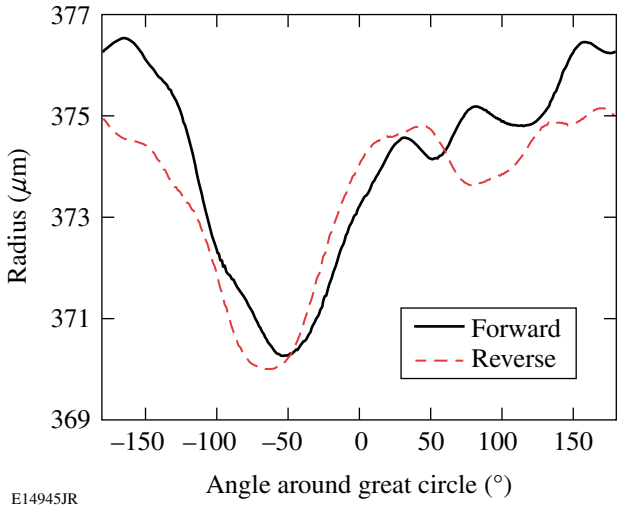

Figure 109.55
Bright-ring radii predicted by 3-D ray tracing of an asymmetric ice surface for opposing views show very different structures. The standard method of shadowgram analysis assumes that both views will be identical and will depend solely on the ice radius at the great circle perpendicular to the view. In fact, the bright-ring radii also depend on the angle of the ice surface relative to each view, and the bright ring may not be centered on rays that strike the ice surface at the great circle.

axis showed that only the lowest modes can be determined with any accuracy by averaging two bright rings.[33]

To self-consistently and accurately determine the 3-D ice surface from shadowgram bright-ring measurements requires the modeling of the effect that the ice-surface asymmetries and defects have on the bright-ring position and including this modeling into the shadowgram analysis. Kozioziemski *et al.*[18] accomplished this in a limited fashion by using interferometry to measure the P1 ice-layer mode along the viewing axis, then correcting the bright-ring position for the effect of the P1 based on a ray-trace study. The ray-trace shadowgram analysis at LLE uses 3-D ray tracing to simultaneously fit the bright-ring measurements for all views (typically 48 different views) to a multimode (up to $\ell = 18$) spherical-harmonic representation of the ice layer.

Producing a simulated full shadowgram for a nonspherically symmetric ice layer can take days of CPU time[20,24] due to the large number of ray-trace calculations required. For this fitting analysis, where many iterations of varying a large number of spherical-harmonic components is required, an alternative was found based on the observation that for spherically symmetric targets, the peak intensity of the bright ring is centered on rays whose paths on both sides of the target are along the viewing axis. This is a poor approximation for asymmetric layers such as a melted layer that is very offset from the view angle, but it is a good approximation for the quasi-symmetrical case of a typical well-layered OMEGA cryogenic target.

With the above assumption, one need only follow one ray for each measured bright-ring position used in the fitting. The rays are launched backward from the measured bright-ring positions along their viewing angles and followed through the target and out the other side where the divergences of the rays' final paths from the view angles are recorded. Nonlinear fitting iterations are employed to adjust the spherical-harmonic description of the ice surface, minimizing the divergence of all the rays from the viewing angles. Typical total fitting times are of the order of several hours to a day, depending on the number of measurements (typically 180 points from each of 48 views) and the number of spherical-harmonic components fit, which varies as $(\ell_{max} + 1)^2$. The nonlinear fitting routine constrains the maximum peak-to-valley variation of the ice surface to be similar to the maximum variation in the bright-ring position, preventing large peak-to-valley structures from occurring on the surface between the data rings or in the polar cap.

An example of the results from the ray-trace analysis with $\ell_{max} = 16$ is shown in Figs. 109.56–109.58. The ice-surface Legendre-mode power spectrum is well behaved up to this ℓ_{max} (Fig. 109.56), and the surface reconstructs show less anomalous structure (Fig. 109.57) than the standard method.

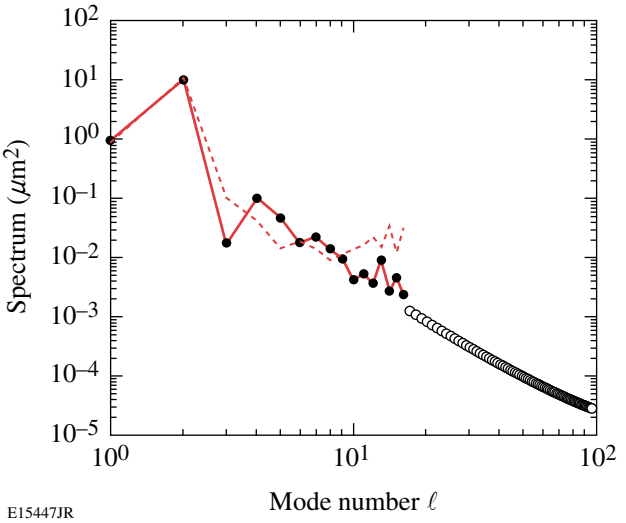

Figure 109.56
Legendre-mode power spectrum P_ℓ of the ice surface. The solid dots correspond to the low-mode-number (up to $\ell_{max} = 16$) ray-trace fit while the dashed line redisplays the standard method fit (up to $\ell_{max} = 16$). The ray-trace analysis is well behaved up to higher mode numbers than the standard method. The circles are the result from mapping the average Fourier-mode spectrum of the many great circles to determine the higher Legendre modes.

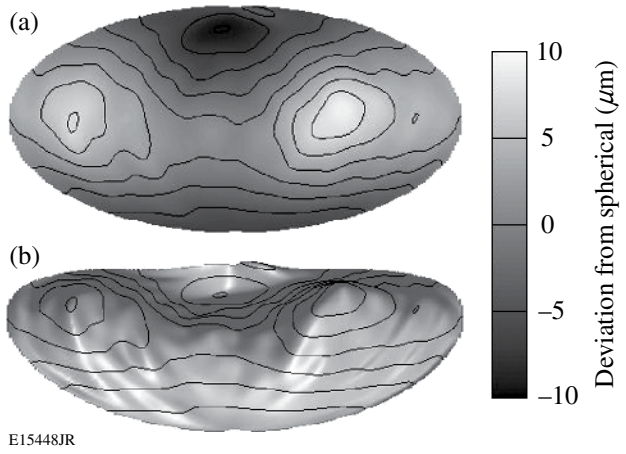

Figure 109.57
Three-dimensional reconstruction of a cryogenic inner ice surface (μm) based on a ray trace $Y_{\ell m}(\theta,\phi)$ fit to the measured data (up to $\ell_{max} = 16$) (a) using the Aitoff projection with contour lines and (b) using the Aitoff projection with surface elevation. This ray-trace fit shows less-artificial structure than the standard fit of Fig. 109.53.

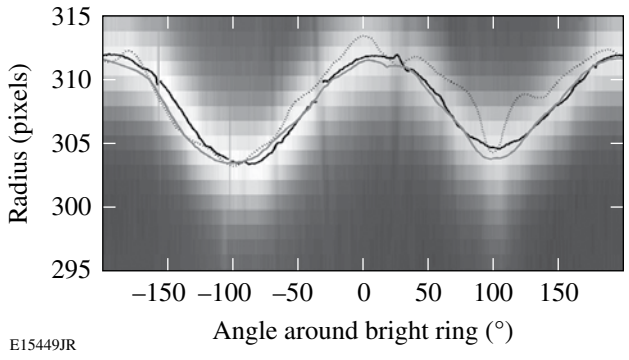

Figure 109.58
Unwrapping of a sample bright ring in polar coordinates shows that the measured bright-ring positions (black line) are much better matched by the predicted bright-ring positions using the ray-trace analysis ice surface (gray line) than by the bright ring predicted using the ice surface determined by the standard method (dotted line).

Figure 109.58 shows a measured bright ring taken from one of the 48 different views of a D_2-ice layer in an OMEGA cryogenic target. The ice surface determined using the standard method with $\ell_{max} = 16$ (Fig. 109.53) would produce the bright ring shown by the dotted line according to ray-trace calculations using that surface. The standard deviation between the measured bright rings for the 48 different views and their standard method predictions is 1.5 μm.

The ice surface determined by the ray-trace analysis (Fig. 109.57) gives the bright-ring prediction shown by the solid gray line in Fig. 109.58. This surface produces a much better match to the observed bright ring. The standard deviation between the measured bright rings for the 48 different views and their ray-trace analysis predictions is 0.8 μm, a reduction of 45% from the standard method.

Summary and Discussion

It has been shown that the bright-ring position can be measured very precisely, but accurately correlating the bright-ring position to an ice-surface position is difficult. The standard method of applying spherically symmetric bright-ring calculations is inaccurate for asymmetric ice layers. Incorporating asymmetric ray tracing directly into the bright-ring analysis allows a self-consistent fitting of the bright rings from multiple views to an ice surface. Ray-tracing analysis reduced the error between the measured bright rings (for 48 different views) and those predicted for the fitted ice surface by 45% in comparison with the ice surface determined by the standard analysis.

It may be possible to further improve the performance of the ray-trace shadowgram analysis by

- modeling the bright-ring position, directly taking into account the uncollimated illumination of the actual shadowgraphy instead of assuming that the ring is centered on rays parallel to the viewing angles,
- fitting the optical differences between the views (magnification, focal position, etc.),
- adding some localized (e.g., spherical wavelet) defects to the ice-surface fitting to account for bright-ring features too localized to be fit by spherical harmonics and a reasonable ℓ_{max}, and
- including the effects of outer-surface perturbations on the bright ring that are believed to be responsible for some sharp features in the bright ring.

It is important to note that as the ice-layer quality improves and becomes more symmetric, the accuracy of the standard method improves. Initial studies of DT cryogenic targets for OMEGA[34] indicate that beta-layered DT targets are very smooth and symmetric and good candidates for accurate standard analyses. These very symmetric layers may still benefit from ray-trace analysis by isolating the effects of outer-surface perturbations on the bright ring that can be even larger than the actual ice-surface effects.

LLE is building a cryogenic fill-tube target station that will allow validation of this ray-trace modeling and shadowgram

analysis. The station will possess target rotation capabilities and equatorial views for both shadowgraphy and x-ray phase-contrast[35] layer diagnostics, allowing a direct comparison of ray-trace shadowgraphic analysis with (1) the standard analysis; (2) the standard analysis using averaged bright rings from opposing views; and (3) x-ray-phase-contrast direct measurements of the ice surface.

ACKNOWLEDGMENT

This work was supported by the U.S. Department of Energy Office of Inertial Confinement Fusion under Cooperative Agreement No. DE-FC52-92SF19460, the University of Rochester, and the New York State Energy Research and Development Authority. The support of DOE does not constitute an endorsement by DOE of the views expressed in this article.

REFERENCES

1. J. Nuckolls *et al*., Nature **239**, 139 (1972).
2. T. R. Boehly, D. L. Brown, R. S. Craxton, R. L. Keck, J. P. Knauer, J. H. Kelly, T. J. Kessler, S. A. Kumpan, S. J. Loucks, S. A. Letzring, F. J. Marshall, R. L. McCrory, S. F. B. Morse, W. Seka, J. M. Soures, and C. P. Verdon, Opt. Commun. **133**, 495 (1997).
3. J. D. Lindl, Phys. Plasmas **2**, 3933 (1995).
4. J. D. Lindl, *Inertial Confinement Fusion: The Quest for Ignition and Energy Gain Using Indirect Drive* (Springer-Verlag, New York, 1998), Chap. 6, p. 61.
5. Lord Rayleigh, Proc. London Math Soc. **XIV**, 170 (1883).
6. G. Taylor, Proc. R. Soc. London Ser. A **201**, 192 (1950).
7. V. Lobatchev and R. Betti, Phys. Rev. Lett. **85**, 4522 (2000).
8. M. C. Herrmann, M. Tabak, and J. D. Lindl, Phys. Plasmas **8**, 2296 (2001).
9. R. Betti, K. Anderson, V. N. Goncharov, R. L. McCrory, D. D. Meyerhofer, S. Skupsky, and R. P. J. Town, Phys. Plasmas **9**, 2277 (2002).
10. R. P. J. Town and A. R. Bell, Phys. Rev. Lett. **67**, 1863 (1991).
11. D. D. Meyerhofer, J. A. Delettrez, R. Epstein, V. Yu. Glebov, V. N. Goncharov, R. L. Keck, R. L. McCrory, P. W. McKenty, F. J. Marshall, P. B. Radha, S. P. Regan, S. Roberts, W. Seka, S. Skupsky, V. A. Smalyuk, C. Sorce, C. Stoeckl, J. M. Soures, R. P. J. Town, B. Yaakobi, J. D. Zuegel, J. Frenje, C. K. Li, R. D. Petrasso, D. G. Hicks, F. H. Séguin, K. Fletcher, S. Padalino, C. Freeman, N. Izumi, R. Lerche, T. W. Phillips, and T. C. Sangster, Phys. Plasmas **8**, 2251 (2001).
12. P. W. McKenty, V. N. Goncharov, R. P. J. Town, S. Skupsky, R. Betti, and R. L. McCrory, Phys. Plasmas **8**, 2315 (2001).
13. W. J. Hogan, E. I. Moses, B. E. Warner, M. S. Sorem, and J. M. Soures, Nucl. Fusion **41**, 567 (2001).
14. S. W. Haan *et al*., Fusion Sci. Technol. **49**, 553 (2006).
15. J. K. Hoffer *et al*., Fusion Technol. **30**, 529 (1996).
16. J. D. Sheliak *et al*., Fusion Technol. **30**, 83 (1996).
17. D. N. Bittner *et al*., Fusion Technol. **35**, 244 (1999).
18. B. J. Kozioziemski *et al*., in *Inertial Fusion Sciences and Applications 2003*, edited by B. A. Hammel, D. D. Meyerhofer, J. Meyer-ter-Vehn, and H. Azechi (American Nuclear Society, La Grange Park, IL, 2004), pp. 762–765.
19. J. A. Koch *et al*., Fusion Technol. **38**, 123 (2000).
20. J. A. Koch *et al*., Fusion Sci. Technol. **43**, 55 (2003).
21. D. H. Edgell, W. Seka, R. S. Craxton, L. M. Elasky, D. R. Harding, R. L. Keck, and M. D. Wittman, Fusion Sci. Technol. **49**, 616 (2006).
22. I. V. Aleksandrova *et al*., J. Phys. D: Appl. Phys. **37**, 1163 (2004).
23. E. R. Koresheva *et al*., Nucl. Fusion **46**, 890 (2006).
24. F. Lamy *et al*., Fusion Sci. Technol. **48**, 1307 (2005).
25. F. Gillot *et al*., Fusion Sci. Technol. **49**, 626 (2006).
26. S. Jin, *2002 Summer Research Program for High School Juniors at the University of Rochester's Laboratory for Laser Energetics*, Rochester, NY, LLE Report No. 329, LLE Document No. DOE/SF/19460-479 (2003).
27. DALSA, Waterloo, Ontario, Canada, N2V 2E9 (http://www.dalsa.com).
28. APPLIED IMAGE, Inc., Rochester, NY 14609, (http://www.applied-imagegroup.biz).
29. R. B. Stephens *et al*., Fusion Sci. Technol. **45**, 210 (2004).
30. S. Pollaine and S. Hatchett, Nucl. Fusion **44**, 117 (2004).
31. D. R. Harding, D. D. Meyerhofer, S. J. Loucks, L. D. Lund, R. Janezic, L. M. Elasky, T. H. Hinterman, D. H. Edgell, W. Seka, M. D. Wittman, R. Q. Gram, D. Jacobs-Perkins, R. Early, T. Duffy, and M. J. Bonino, Phys. Plasmas **13**, 056316 (2006).
32. G. Balonek, *2004 Summer Research Program for High School Juniors at the University of Rochester's Laboratory for Laser Energetics*, University of Rochester, Rochester, NY, LLE Report No. 337, LLE Document No. DOE/SF/19460-590 (2005).
33. R. Wu, *2005 Summer Research Program for High School Juniors at the University of Rochester's Laboratory for Laser Energetics*, University of Rochester, Rochester, NY, LLE Report No. 343 (2006).
34. T. C. Sangster, R. Betti, R. S. Craxton, J. A. Delettrez, D. H. Edgell, L. M. Elasky, V. Yu. Glebov, V. N. Goncharov, D. R. Harding, D. Jacobs-Perkins, R. Janezic, R. L. Keck, J. P. Knauer, S. J. Loucks, L. D. Lund, F. J. Marshall, R. L. McCrory, P. W. McKenty, D. D. Meyerhofer, P. B. Radha, S. P. Regan, W. Seka, W. T. Shmayda, S. Skupsky, V. A. Smalyuk, J. M. Soures, C. Stoeckl, B. Yaakobi, J. A. Frenje, C. K. Li , R. D. Petrasso, F. H. Séguin, J. D. Moody, J. A. Atherton, B. D. MacGowan, J. D. Kilkenny, T. P. Bernat, and D. S. Montgomery, "Cryogenic DT and D_2 Targets for Inertial Confinement Fusion," to be published in Physics of Plasmas (invited).
35. D. S. Montgomery, A. Nobile, and P. J. Walsh, Rev. Sci. Instrum. **75**, 3986 (2004).

Filamentation Analysis in Large-Mode-Area Fiber Lasers

Introduction

Fiber lasers have developed rapidly in recent years,[1,2] with output powers above the kilowatt level.[3,4] Along with the increasing output power, nonlinear effects become important and can ultimately limit the power scalability in the fiber. Two well-known nonlinear effects that have limited the output power of fiber lasers are stimulated Brillouin scattering (SBS) and stimulated Raman scattering (SRS). Several methods can be used to increase the SBS threshold, including increasing the signal bandwidth to decrease the Brillouin gain,[5] using new fiber designs to decrease the overlap between acoustic and optics modes,[6] varying the temperature along the cavity,[7,8] and using low-numerical-aperture, large-mode-area (LMA) fibers.[9] Spectral filtering and LMA fibers are also used to mitigate SRS. In LMA fibers, the large mode area serves to decrease the optical intensity, therefore increasing the nonlinear threshold.

While many methods are being investigated to suppress SBS and SRS, other nonlinear effects, such as self-focusing, also have an impact. In 1987 Baldeck *et al.*[10] observed the self-focusing effect in the optical fiber with picosecond laser pulses. Self-focusing can lead to beam-quality degradation through a process called filamentation. The physical nature of filamentation arises from self-focusing through the nonlinear refractive index. When the light intensity is strong enough for self-focusing to occur, the beam in the laser cavity is focused narrower and narrower. As a result, the laser beam is limited in a small region in the center of the core. Thus the corresponding population inversion is depleted in the center of the core, but undepleted in other areas of the core, i.e., spatial hole burning. With spontaneous emission occurring throughout the core, it is easy to generate other lasing beams, finally resulting in filamentation. Filamentation has been studied extensively in semiconductor lasers in the past two decades;[11–13] however, little work has been done in fiber lasers.

In this article, a theoretical model for the filamentation effect in LMA fiber lasers is presented. Solving the paraxial wave equation and population rate equation in three dimensions, an expression for the filament gain is derived using a perturbation method. This expression includes both spatial and temporal characteristics, the filament spacing, and oscillation frequency. The filament gain also depends on the physical parameters of the optical fiber, the nonlinear refractive index, and the pump and signal power. This model can predict the output-power thresholds at which the filamentation will occur for a given set of optical-fiber parameters, in particular the core diameter. A simplified threshold expression is also provided. The results are shown to be consistent with previous experiments.

Theoretical Model and Steady-State Solution

Starting with Maxwell's equation in a dielectric medium, a wave equation is obtained, assuming an optical field of the form $\widetilde{A} = A_s(r,\phi,z,t)e^{i(kz-\omega t)}$ and using the slowly varying envelope approximation to neglect the second derivatives of the time t and axial coordinate z. After considering the gain, loss, nonlinear refractive index, and the coupling of the pump and the signal light in the optical fiber, the optical field of the signal light can be found to satisfy the paraxial wave equation

$$\frac{\partial A_s}{\partial z} + \frac{1}{v_g}\frac{\partial A_s}{\partial t} = \frac{i}{2k_s}\nabla_T^2 A_s + \left[\frac{1}{2}g_s' + i\left(2\gamma_p P_p + \gamma_s P_s\right)\right]A_s, \qquad (1)$$

where A_s is the slowly varying amplitude of the signal light along z and t, v_g is the group velocity, $k_s = n_{\text{eff}}\,k_0$ is the mode propagation constant of the signal light, n_{eff} is the effective index of the refraction, and k_0 is the free-space propagation constant. $\nabla_T^2 = (1/r)(\partial/\partial r) + (\partial^2/\partial r^2) + (1/r^2)(\partial^2/\partial\phi^2)$ is the transverse Laplacian operator, representing diffraction. $g_s' = g_s - \alpha_{\text{cav}}$ is the net gain of the signal light, where $g_s = N_2\sigma_s^e - N_1\sigma_s^a$ is the local gain of the signal light. The energy-level system of the excitation ion is assumed to be a two-level system,[16] where N_2, N_1 are the upper- and lower-state population densities, respectively. σ_j^a, σ_j^e are the absorption and emission cross sections at frequency ω_j with $j = p, s$ representing pump and signal light. To analyze the optical fiber laser, the mirror losses are distributed throughout the cavity, $\alpha_{\text{cav}} = \alpha_{\text{int}} - \ln(R_1R_2)/2L$, where α_{int} is the internal loss, L is the cavity length, and R_1 and R_2 are the reflectivities of the mirrors. For the case of a fiber ampli-

fier, the cavity loss is the same as the internal loss, $\alpha_{cav} = \alpha_{int}$. $\gamma_j = \bar{n}_2 k_0 / A_{\mathrm{eff}_j}$ is the nonlinear parameter at frequency ω_j, $\bar{n}_2$ is the Kerr coefficient, and A_{eff_j} is the effective cross-section area at frequency ω_j. The nonlinear parameter γ_j represents self-focusing in optical fibers, for $\gamma_j > 0$; $P_j = |A_j|^2$ is the optical power in the core at frequency ω_j.

With the assumption of a two-level system, the rate equation of the excited state is given by[16]

$$\frac{\partial N_2}{\partial t} = -\frac{N_2}{\tau} - \left(N_2\sigma_s^e - N_1\sigma_s^a\right)\phi_s - \left(N_2\sigma_p^e - N_1\sigma_p^a\right)\phi_p, \quad (2)$$

where $\phi_j = P_j / \left(A_{\mathrm{eff}_j} h\nu_j\right)$ is the photon flux at the frequency ν_j, τ is the spontaneous lifetime of the excited state, and $N_t = N_1 + N_2$ is the total population density.

Equation (1) is a nonlinear equation without an exact solution. The waveguide mode is first solved in the absence of gain and loss for low-intensity levels (i.e., no nonlinear effects). The solution in the core can be found:[14]

$$\begin{aligned}\widetilde{A} &= A_s \exp\left[i\left(k_s z - \omega_s t\right)\right] \\ &= A_{s_0} J_m\left(p_s r\right)\exp\left(im\phi\right)\exp\left[i\left(k_s z - \omega_s t\right)\right], \end{aligned} \quad (3)$$

where A_{s_0} is a constant, $p_s^2 = n_1^2 k_0^2 - k_s^2$, and n_1 is the refractive index in the core. The index m can take only integer values, with $m = 0$ for the fundamental mode. Therefore, the optical field in Eq. (1) should have the form $A_s = A_{s_1}(z) J_m(p_s r)\exp(im\phi)$. Substituting the Laplacian term with $\nabla_T^2 A_s = -p_s^2 A_s$, Eq. (1) can be rewritten in the steady state as

$$\frac{\partial A_s}{\partial z} = \left[\frac{1}{2}g_s' - \frac{ip_s^2}{2k_s} + i\left(2\gamma_p P_p + \gamma_s P_s\right)\right]A_s. \quad (4)$$

For simplicity, bi-directional pumping is assumed, so the pump power P_p can be regarded as nearly constant along the cavity, which leads to a constant gain along the cavity. When a laser is above threshold, the gain is clamped to the value of cavity loss at threshold. Since the loss is distributed along the cavity in this unfolded cavity model,[13] net gain g_s' is zero and the signal power $P_s = |A_s|^2$ must therefore be independent of $z\left[\,|A_{s_1}(z)| = A_{s_0}\right]$. Thus, the solution of Eq. (4) has the form $A_s = A_{s_0} J_m(p_s r)\exp(im\phi)\exp(i\Delta k_s z)$, is given by

$$\Delta k_s = \frac{1}{2}g_s' - \frac{ip_s^2}{2k_s} + i\left(2\gamma_p P_p + \gamma_s P_s\right). \quad (5)$$

Equation (5) shows the change for the complex propagation constant due to the gain, loss, nonlinearity, and the waveguide mode.

The modal gain $g_s = \Gamma_s g$ includes the transverse confinement factor $\Gamma_s = A_{\mathrm{effs}} / A_{\mathrm{core}}$ to account for the fact that excited ions are doped only in the core. Substituting the relation $N_1 = N_t - N_2$ into Eq. (2), the upper-state population can be found in the steady state as

$$N_2 = \frac{N_t\left(\dfrac{\sigma_s^a}{\sigma_s^e + \sigma_s^a}\dfrac{P_s}{P_s^{\mathrm{sat}}} + \dfrac{\sigma_p^a}{\sigma_p^e + \sigma_p^a}\dfrac{P_p}{P_p^{\mathrm{sat}}}\right)}{1 + \dfrac{P_s}{P_s^{\mathrm{sat}}} + \dfrac{P_p}{P_p^{\mathrm{sat}}}}, \quad (6)$$

where $P_j = |A_j|^2$, $P_j^{\mathrm{sat}} = \left(A_{\mathrm{eff}_j} h\nu_j\right) / \left[\left(\sigma_j^e + \sigma_j^a\right)\tau\right]$ is defined as saturation power with $j = p, s$. For the case of the fiber laser, with the threshold condition of $g_s = \alpha_{cav}$ and the assumption of constant pump power, the signal power is constant along the z direction in the cavity solved from Eq. (6):

$$\begin{aligned} P_s = \Bigg\{ &-\left(N_t\sigma_s^a + \frac{\alpha_{cav}}{\Gamma_s}\right) \\ &+ \left[\frac{N_t\left(\sigma_p^e\sigma_s^a - \sigma_p^a\sigma_s^e\right)}{\sigma_p^e + \sigma_p^a} + \frac{\alpha_{cav}}{\Gamma_s}\right]\frac{P_p}{P_p^{\mathrm{sat}}}\Bigg\}\frac{\alpha_{cav}P_s^{\mathrm{sat}}}{\Gamma_s}. \end{aligned} \quad (7)$$

Linear Stability Analysis and Filament Gain

The stability of the single-mode solution against nonlinear spatial perturbations must be asserted to determine under what condition beam filamentation will occur. If small perturbations grow with propagation, then the steady-state solution is unstable and the beam can break up under propagation through the fiber. Small perturbations a and n are introduced in the optical field $A_s = \left[\sqrt{P_s} + a(r,\phi,z,t)\exp\left(i\Delta k_s z\right)\right]$ and upper-state population density $N'_2 = N_2 + n(r,\phi,z,t)$. Linearizing Eqs. (1) and (2) in a and n, while using the steady-state solutions, leads to two coupled linear equations:

$$\begin{aligned}\frac{\partial a}{\partial z} + \frac{1}{v_g}\frac{\partial a}{\partial t} &= \frac{i}{2k_s}\left(p_s^2 a + \nabla_T^2 a\right) + \frac{1}{2}g_s' a \\ &+ \frac{1}{2}\Gamma_s n\sqrt{P_s}\left(\sigma_s^e + \sigma_s^a\right) + i\gamma_s P_s\left(a + a^*\right), \end{aligned} \quad (8)$$

$$\begin{aligned} -\tau\frac{\partial n}{\partial t} &= n\left(1 + \frac{P_s}{P_s^{\mathrm{sat}}} + \frac{P_p}{P_p^{\mathrm{sat}}}\right) \\ &+ \left(N_2 - N_t\frac{\sigma_s^a}{\sigma_s^e + \sigma_s^a}\right)\frac{\sqrt{P_s}}{P_s^{\mathrm{sat}}}\left(a + a^*\right). \end{aligned} \quad (9)$$

Due to the cylindrical geometry, the perturbation is assumed to have the form of a Bessel function,

$$a = a_1 J_{k_\phi}(pr)\exp\left[i\left(k_\phi\phi + k_z z - \Omega t\right)\right] + a_2 J_{k_\phi}(pr)\exp\left[-i\left(k_\phi\phi + k_z z - \Omega t\right)\right], \quad (10)$$

$$n = n_0 J_{k_\phi}(pr)\exp\left[i\left(k_\phi\phi + k_z z - \Omega t\right)\right] + n_0^* J_{k_\phi}(pr)\exp\left[-i\left(k_\phi\phi + k_z z - \Omega t\right)\right], \quad (11)$$

where p is a Bessel parameter, k_ϕ has integer value, k_z is the propagation constant of the perturbation, Ω is its oscillation frequency, and n_0, a_1, and a_2 are constants. The two field-perturbation parameters originate from the fact that a represents a complex field, which is determined by two independent variables.[17] The perturbation in population density n is a real number, which can be determined by one variable. Substituting Eqs. (10) and (15) into the coupled equations leads to linear equations about a_1 and a_2^*. In the condition that they have nontrivial solutions, k_z needs to satisfy

$$k_z = \frac{\Omega}{v_g} + i\frac{1}{2}\left[G(1+i\xi) - g_s'\right] \pm \sqrt{\frac{p'^2}{2k_s}\left(\frac{p'^2}{2k_s} - 2\gamma_s P_s\right) - \frac{1}{4}\left[G^2(1+i\xi)^2 + g_s'^2\right]}, \quad (12)$$

where $p'^2 = p^2 - p_s^2$. The factor ξ and the saturated power gain G are defined respectively as

$$\xi = \frac{\Omega\tau}{1 + \dfrac{P_s}{P_s^{\text{sat}}} + \dfrac{P_p}{P_p^{\text{sat}}}}, \quad (13)$$

$$G = \Gamma_s g_s \frac{\dfrac{P_s}{P_s^{\text{sat}}}\left(1 + \dfrac{P_s}{P_s^{\text{sat}}} + \dfrac{P_p}{P_p^{\text{sat}}}\right)}{\left(1 + \dfrac{P_s}{P_s^{\text{sat}}} + \dfrac{P_p}{P_p^{\text{sat}}}\right)^2 + (\Omega\tau)^2}. \quad (14)$$

The steady-state solution is stable provided the perturbation gain (which is the imaginary part of the k_z) is less than the cavity loss, a reflection of the growth of the laser field in the cavity. With the relation $g = -2Im(k_z)$, the perturbation gain can be extracted from Eq. (14), where the factor 2 is added to define the power gain:

$$g = \text{Re}\sqrt{\frac{2p'^2}{k_s}\left(2\gamma_s P_s - \frac{p'^2}{2k_s}\right) + \left[G^2(1+i\xi)^2 + g_s'^2\right]} - (G - g_s'). \quad (15)$$

The negative root from Eq. (12) is selected because the gain needs to be positive for the filamentation to occur. Equation (15) gives a general expression for the filament gain. In a fiber laser, when the population inversion is clamped to the threshold, the net gain g_s' is zero. The filament spacing is defined as $w = \pi/p$, and oscillation frequency $f = |\Omega|/2\pi$.

It is already known that the solution of perturbation must have the form of a Bessel function due to the cylindrical geometry of the fiber. Because the perturbation is also an electromagnetic field, it also needs to satisfy the boundary condition on the interface between the core and cladding, which means for every k_ϕ the Bessel parameter p or filament spacing w has only discrete values. In other words, the perturbation also has mode structure, which is similar to the well-known mode properties of the electromagnetic field in fibers. Equation (15) shows no dependence of k_ϕ to the filament gain, but that does not imply that all the modes can resonate. Mathematically, lower-order modes, especially the fundamental mode of the perturbation, do not have dense enough mode structure for filamentation to occur. Physically, the largest amplitude of the fundamental mode is in the center of the core, where the population is depleted. The amplitudes of higher-order modes are zero at the center and large at the margin where the population is undepleted. Therefore higher-order modes of perturbation are more likely to occur than lower-order modes. The peak-to-peak period of squared higher-order Bessel solutions is approximately equal to π, which accounts for the factor π in the definition of filament spacing.

Spatiotemporal Analysis of Filament Gain in Optical Fiber Lasers

Most high-power fiber lasers are Yb doped, due to high quantum efficiency, high doping density, the absence of excited-state absorption, and a long upper-state lifetime. Therefore the parameters used in this section are for typical Yb-doped fiber lasers and are shown in Table 109.V.

Figure 109.59 shows a 3-D plot of normalized filament gain versus normalized filament spacing and oscillation frequency for the signal peak power P_s = 10 kW and core diameter d_{core} = 100 μm. The figure is symmetric in frequency space; therefore only positive frequency is plotted. To facilitate understanding of Fig. 109.59, normalized gain $g_{\text{norm}} = g/\alpha_{\text{cav}}$ and normalized filament spacing $w_{\text{norm}} = w/a_{\text{core}}$ are used, where a_{core} is the radius of

the fiber core. If perturbation gain is larger than cavity loss ($g_{\text{norm}} > 1$), the filament can grow in the cavity; if filament spacing is less than core radius ($w_{\text{norm}} < 1$), filament can appear in the core. Both of these conditions need to be satisfied for the filament to occur since the gain exists only within the fiber core. In Fig. 109.59 there is a peak in the spatial dimension, which defines the filament spacing at which the perturbation will grow most rapidly, where $g > \alpha_{\text{cav}}$. However, the normalized filament spacing corresponding to the peak region is larger than unity, which means the filament is outside the core, and filamentation cannot occur. In the temporal dimension, the curve is constant with a dip at low frequencies. Since the noise perturbation is dynamic, there is less possibility for the filament to grow statically or in low frequency.

Table 109.V: Parameters for ytterbium-doped optical fiber laser calculations.

Parameter	Value
λ_p	0.976 μm
λ_s	1.053 μm
σ_p^a	2476×10^{-27} m^2
σ_p^e	2483×10^{-27} m^2
σ_s^a	20.65×10^{-27} m^2
σ_s^e	343.0×10^{-27} m^2
N_t	9.4×10^{24} m^{-3}
τ	0.84 ms
Γ_p	0.01
n_{core}	1.46
n_{clad}	1.45562
$\overline{n}_2$	2.6×10^{-20} m^2/W
R_1	1
R_2	0.5
L	0.5 m
α_{int}	0.003 m^{-1}

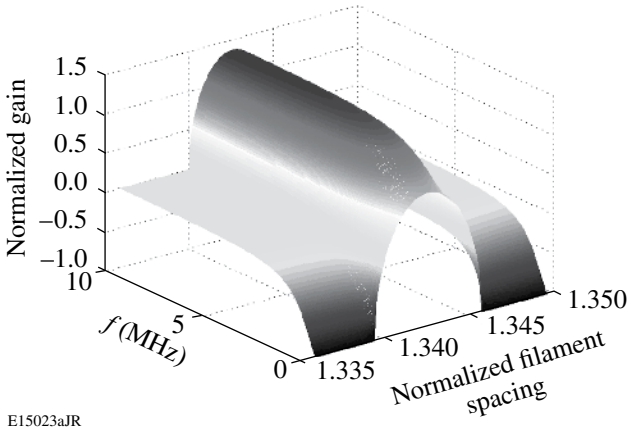

Figure 109.59
Normalized filament gain versus normalized filament spacing and frequency for $d_{\text{core}} = 100$ μm, $P_s = 10$ kW.

In Fig. 109.60, the signal peak power P_s is increased to 10 MW. The gain peak becomes much larger, and the corresponding filament spacing falls into the core. Because both of the thresholds are reached ($g_{\text{norm}} > 1$ and $w_{\text{norm}} < 1$), filamentation can occur. There is no observable feature in the temporal dimension. Thus for signal peak power high above the gain threshold, the temporal modulation of the filamentation can occur at any frequency.

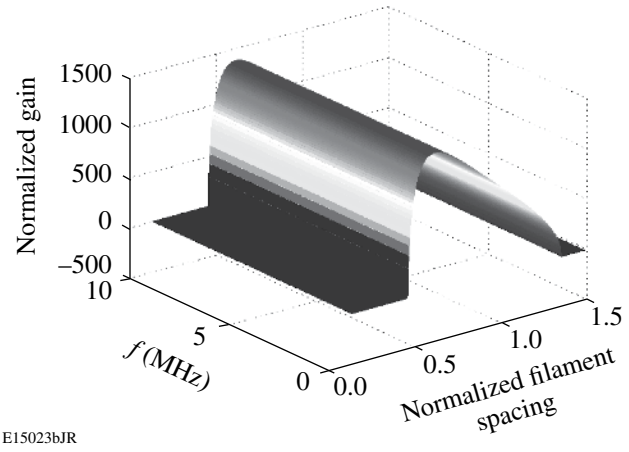

Figure 109.60
Normalized filament gain versus normalized filament spacing and frequency for $d_{\text{core}} = 100$ μm, $P_s = 10$ MW.

Figure 109.61 shows normalized filament spacing and normalized filament gain corresponding to the gain peak as functions of signal peak power for the core diameters ranging from 20 μm to 200 μm, when $f = 10$ GHz. With the increase of the signal peak power, the filament gain peak will move toward the small filament spacing and the filament gain will also increase. This agrees with conventional understanding: the higher the power, the denser the filaments and the larger the possibility for filamentation to occur. From Fig. 109.61 the gain threshold for the filamentation to occur ($g = \alpha_{\text{cav}}$) can also be observed; it is from a magnitude of 100 W to 10 kW for core diameters ranging from 20 μm to 200 μm. The filament spacing threshold, however, is around a few MW, which then determines the filamentation threshold. Self-focusing, and thus filamentation, is determined only by the peak power (highest power) in fiber lasers, regardless of different average powers. Correspondingly, cw (continuous wave) operation is represented by the same curves in Fig. 109.61.

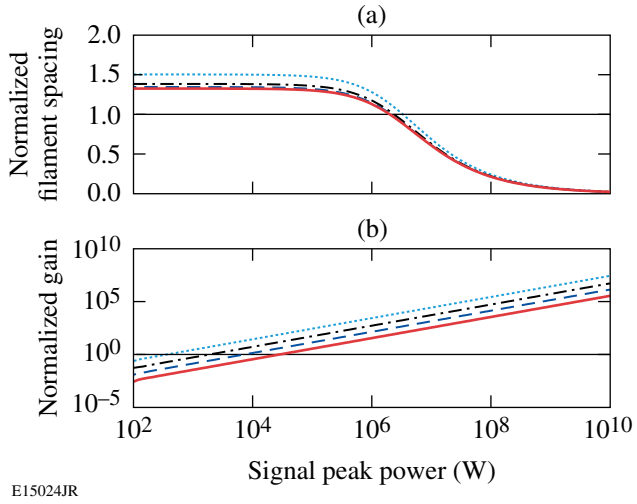

Figure 109.61
(a) Normalized filament spacing and (b) normalized gain as a function of the signal peak power for various core diameters: 20 μm (dotted), 50 μm (dashed–dotted), 100 μm (dashed), and 200 μm (solid) (f = 10 GHz).

The gain peak with respect to the normalized filament spacing can be obtained by solving $\partial g/\partial w = 0$. Correspondingly, the filament spacing and signal peak power have the relation $\pi^2/w^2 = 2\gamma_s k_s P_s + p_s^2$. At spatial threshold $w = a_{\text{core}}$, the spatial threshold power is

$$P_{\text{th}}^{\text{spatial}} = \frac{\left(\pi^2/a_{\text{core}}^2\right) - p_s^2}{2\gamma_s k_s}. \tag{16}$$

At high frequency, saturation gain G and factor ξ can be neglected from Eq. (15), and the filament gain can be simplified at the gain peak as $g = 2\gamma_s P_s$. At gain threshold $g = \alpha_{\text{cav}}$, the gain threshold power is

$$p_{\text{th}}^{\text{gain}} = \frac{\alpha_{\text{cav}}}{2\gamma_s}. \tag{17}$$

Figure 109.62 shows the spatial and gain threshold powers as functions of core diameter. As would be expected from an intensity-dependent process, the gain threshold power increases as the core diameter (and thus mode diameter) increases. Conversely, the spatial threshold power decreases with increasing core diameter. For larger modes, the effects of diffraction and waveguiding are weaker; thus the mode becomes more susceptible to filamentation. For all core diameters below 1000 μm, the spatial threshold dominates.

Figure 109.63 shows the normalized and non-normalized filament gains as functions of the signal peak power for three

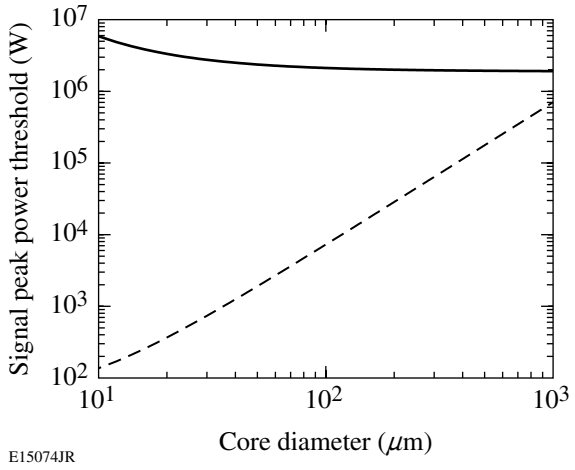

Figure 109.62
Gain threshold power (dashed) and spatial threshold power (solid) as a function of core diameter (f = 10 GHz).

cavity lengths, from 0.5 m to 4 m when d_{core} = 100 μm and f = 10 GHz. It is instructive to see that the normalized gain changes with cavity length since the cavity length relates to the cavity loss in the unfolded cavity model. The non-normalized gain is not affected by the fiber length since it is dependent only on signal peak power. In the laser cavity, light propagates back and forth, and the optical path is effectively infinitely long.

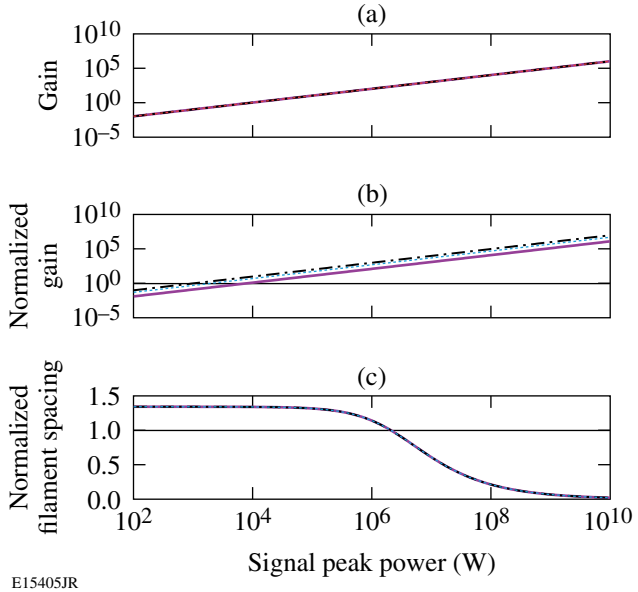

Figure 109.63
(a) Non-normalized filament gain, (b) normalized filament gain, and (c) normalized filament spacing as a function of the signal peak power for three different cavity lengths: 0.5 m (solid), 2 m (dotted), and 4 m (dashed–dotted) (d_{core} = 100 μm, f = 10 GHz).

Thus filamentation can occur as long as the filament gain is larger than cavity loss, and it does not depend on cavity length. Figure 109.63(c) shows a plot of the corresponding normalized filament spacing versus signal peak power. The filament spatial properties do not change with cavity length since they have the same transverse spatial structure. Because spatial threshold determines total threshold here, total threshold is independent of cavity length.

Discussion and Conclusion

Only a single experiment reported self-focusing in multimode optical fibers.[10] In this work, 25-ps pulses were coupled into multimode fiber, and a mode scrambler was used to distribute pulse energy into every mode. The output beam profile was unchanged for pulse energies less than 1 nJ. When the pulse energy was increased beyond 10 nJ, self-focusing occurred. That is to say, the peak power threshold is between 40 W to 400 W. Considering the use of the mode scrambler, the threshold should be much smaller compared to our model, which assumes an unperturbed starting condition of the fundamental mode. Our model gives a gain threshold of around 1 W and a filament spacing threshold of around 0.5 MW. Starting with a set of modes instead of a single mode will lead to a reduction in the filamentation threshold due to the added spatial variations in the initial condition. More recently, an ultrashort Yb-doped fiber laser system was demonstrated with peak power in the fiber of 15 kW (Ref. 4). Since their peak power is still under the filament spacing threshold (~7 MW from our model), no filamentation occurs.

The thresholds of SBS and SRS are around ~20 W and ~1 kW for short-length cw fiber lasers.[7] For short-pulsed fiber lasers, SBS can be neglected for the broadband spectra; the threshold of SRS can be increased to MW using the LMA fibers. Recently, Cheng[18] has reported a 1.56-MW-peak-power laser system using 80-μm-core, Yb-doped LMA fibers. Given the rapid rate of progress in high-peak-power fiber lasers, self-focusing and filamentation will soon become a problem that will need to be addressed in order to retain high-beam-quality output. It is important to note that since these phenomena effectively increase the spatial frequency of the light in the fiber, bend loss will have a beneficial impact on the filamentation threshold.

In summary, an expression for filament power threshold was derived, using a perturbation method, starting from the paraxial wave equation. The spatial and temporal characteristics of the filament gain were analyzed. Two conditions must be satisfied simultaneously for filamentation to occur: filament gain larger than cavity loss and filament spacing less than the core radius. The filamentation also has the mode characteristics of optical fibers, and its threshold is of the order of a few MW.

ACKNOWLEDGMENT

This work was supported by the U.S. Department of Energy Office of Inertial Confinement Fusion under Cooperative Agreement No. DE-FC52-92SF19460, the University of Rochester, and the New York State Energy Research and Development Authority. The support of DOE does not constitute an endorsement by DOE of the views expressed in this article.

REFERENCES

1. B. Ortaç *et al*., Opt. Lett. **28**, 1305 (2003).
2. J. R. Buckley, F. W. Wise, and F. Ö. Ilday, Opt. Lett. **30**, 1888 (2005).
3. Y.-X. Fan *et al*., IEEE Photonics Technol. Lett. **15**, 652 (2003).
4. F. Röser *et al*., Opt. Lett. **30**, 2754 (2005).
5. G. P. Agrawal, *Nonlinear Fiber Optics*, 3rd ed., Optics and Photonics (Academic Press, San Diego, 2001).
6. K. Shiraki, M. Ohashi, and M. Tateda, J. Lightwave Technol. **14**, 549 (1996).
7. J. Toulouse, J. Lightwave Technol. **23**, 3625 (2005).
8. V. I. Kovalev and R. G. Harrison, Opt. Lett. **31**, 161 (2006).
9. C.-H. Liu *et al*., Electron. Lett. **40**, 1471 (2004).
10. P. L. Baldeck, F. Raccah, and R. R. Alfano, Opt. Lett. **12**, 588 (1987).
11. H. Adachihara *et al*., J. Opt. Soc. Am. B **10**, 658 (1993).
12. D. J. Bossert, J. R. Marciante, and M. W. Wright, IEEE Photonics Technol. Lett. **7**, 470 (1995).
13. J. R. Marciante and G. P. Agrawal, IEEE J. Quantum Electron. **33**, 1174 (1997).
14. D. Gloge, Appl. Opt. **10**, 2252 (1971).
15. G. P. Agrawal, *Lightwave Technology: Components and Devices* (Wiley, Hoboken, NJ, 2004).
16. P. C. Becker, N. A. Olsson, and J. R. Simpson, *Erbium-Doped Fiber Amplifiers: Fundamentals and Technology* (Academic Press, San Diego, 1999).
17. C.-J. Chen, P. K. A. Wai, and C. R. Menyuk, Opt. Lett. **20**, 350 (1995).
18. M.-Y. Cheng *et al*., presented at CLEO/QELS 2006, Long Beach, CA, 21–26 May 2006 (Paper CThAA3).

Averaging of Replicated Pulses for Enhanced-Dynamic-Range, Single-Shot Measurement of Nanosecond Optical Pulses

Introduction

Nanosecond-length laser pulses are commonly used in applications such as light detection and ranging (LIDAR) and remote sensing. Accurate measurement of the pulse shape can be critical for specific applications. In particular, laser systems used for inertial confinement fusion (ICF) are required to produce stable, high-contrast pulse shapes to achieve the highest-possible compression of the target.[1,2] While nonlinear techniques can measure pulse shapes with a contrast of the order of 10^7 (Refs. 3 and 4), reliable measurement of nanosecond-length pulses can only be achieved with either streak cameras or photodiodes in conjunction with oscilloscopes. Streak cameras offer high-dynamic-range (700:1), multichannel (>8) measurements with 30-ps temporal resolution.[5] However, the relatively slow update rate of single-shot, high-dynamic-range streak cameras (0.1 Hz) precludes their use in applications that require real-time monitoring. Such applications include real-time pulse-shape adjustment or the diagnosis of intermittent problems.

Although oscilloscope sampling rates are continually increasing, the vertical resolution has remained stagnant at 8 bits. Additionally, the effective number of bits (ENOB) is limited to 5 or 6 due to inherent noise floor and digitization effects. Therefore, when using photodiodes with oscilloscopes to measure an optical pulse shape, the oscilloscope becomes the limiting factor of measuring contrast, reducing the measurable dynamic range (DR = 2^{ENOB}) to ~45. Such a contrast is insufficient for the accurate measurement of high-contrast ICF pulse shapes that require measurement of pulses with up to 100:1 shape contrast at a reasonable level of accuracy.

The conventional method for reducing noise on periodic signals is to average temporally sequential events, which has the benefit of reducing the signal-to-noise ratio (SNR) by a factor of $\sqrt{N}$, where N is the number of traces. However, nonrepetitive, single-shot events get washed out in the averaging process; this is particularly important when trying to diagnose intermittent failures. Furthermore, the acquisition speed in sequential averaging is reduced by a factor of N.

To capture single-shot events, the pulse can be replicated and averaged with itself to reap the benefits of averaging. In previous work, the pulse of interest was sent through an active fiber loop to produce a replicated pulse train.[6] With gain in the loop, the signal was kept near maximum throughout the pulse train at the expense of amplifier noise added to the signal at every pass. Additionally, the amplitudes of the resultant pulse train followed an exponential decay curve, making it difficult to operate at high repetition rates. In this work, a passive pulse-replication structure is implemented to achieve the series of pulses. The signal is power divided, then recombined with a fixed time delay. Multiple split/recombine stages with digitally increasing delay can yield an arbitrary number of pulses, provided there is sufficient energy in the initial pulse. The replicated pulses are read from a single oscilloscope trace and subsequently averaged in order to achieve increased dynamic range. Similar pulse replication schemes have previously been implemented for increased temporal resolution in measuring picosecond pulses.[7,8]

Experimental Configuration and Measurements

The configuration for passive pulse replication is shown schematically in Fig. 109.64. A series of 2×2 fused-fiber splitters are spliced with $m \times 12.5$-ns-delay fibers between the individual stages. Since successive combinations use splits from previous combinations, the last split is the only place where light is forfeited. It should also be mentioned that since the first splitter has two input ports, two separate pulses can be run simultaneously through this architecture, provided their timing is such that the resultant pulse trains do not overlap in time.

Figure 109.65 shows the resultant 64 pulses from the raw photodiode output as measured on a Tektronix TDS 6154C digital storage oscilloscope, which has a 12-GHz analog bandwidth. The pulses are nominally spaced at 12.5 ns, although precise spacing is not critical to the method.

The trace is acquired from the scope at 25-ps resolution, and the individual pulses are separated by temporal binning. The fine temporal alignment between two pulses $P_i(t)$ and $P_j(t)$

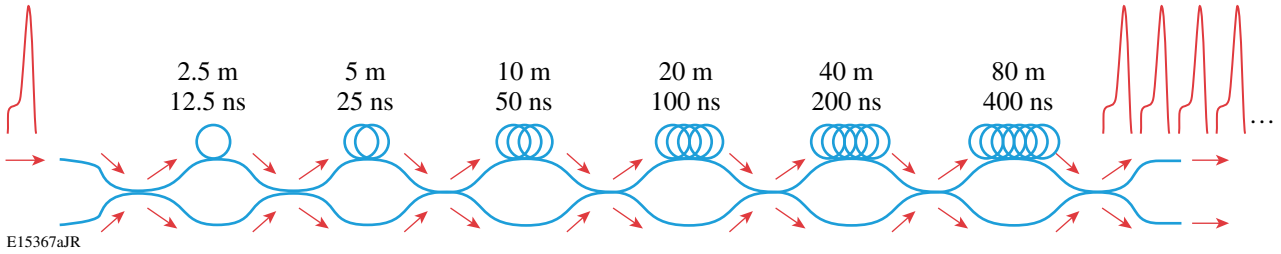

Figure 109.64
Schematic of 64-pulse passive pulse-stacking architecture.

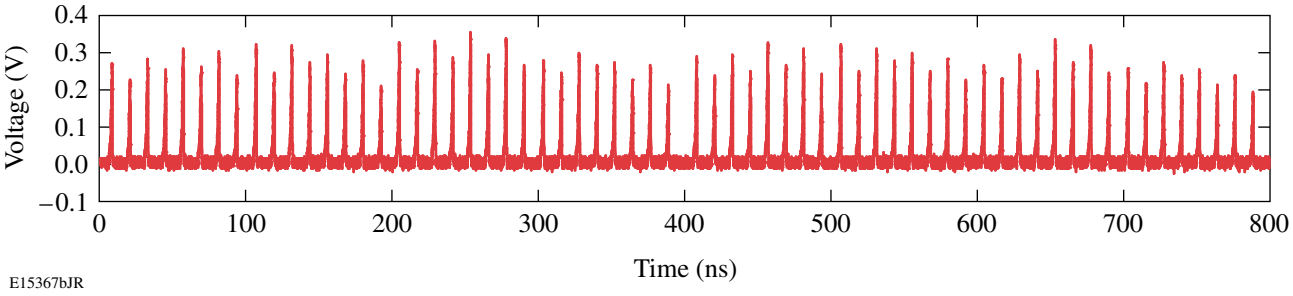

Figure 109.65
Oscilloscope trace showing 64 pulse replicas.

in the pulse train is measured once with a cross-correlation method using the formula

$$X_{ij}(t) = \mathrm{F}^{-1}\left\{\mathrm{F}\left[P_i(t)\right] \times \mathrm{F}^{*}\left[P_j(t)\right]\right\}, \quad (1)$$

where F and F^{-1} denote the discrete fast Fourier transform and its inverse and the asterisk denotes the complex conjugate. The temporal offset t_{ij} is the value of t that maximizes the function $X_{ij}(t)$. $P_j(t)$ is offset by this amount before averaging with the other pulses from the pulse train.

Figure 109.66 shows the single-shot, self-averaged pulse together with a multi-shot–averaged pulse (64 averages) and a single pulse (no averaging) for comparison. Similar to the multi-shot average, the single-shot average shows clear performance enhancement compared to the single-shot case. Additionally, due to the jitter inherent in temporal acquisitions, the multi-shot–averaged case has a reduced effective bandwidth compared to the single-shot–averaged trace, as can be seen in the relative sharpness of the leading edges of the corresponding pulses in Fig. 109.66.

The dynamic range of the measurement is defined as the ratio of the peak of the signal to the signal level where the SNR is equal to unity. Figure 109.67 shows the calculated dynamic range for the single-shot and multi-shot averages as a function of the peak signal on the photodiode. In the multi-trace averages, there are 64 temporally displaced copies at different signal amplitudes (as can be seen in Fig. 109.65), each of which is plotted independently. Given that the noise level is identical

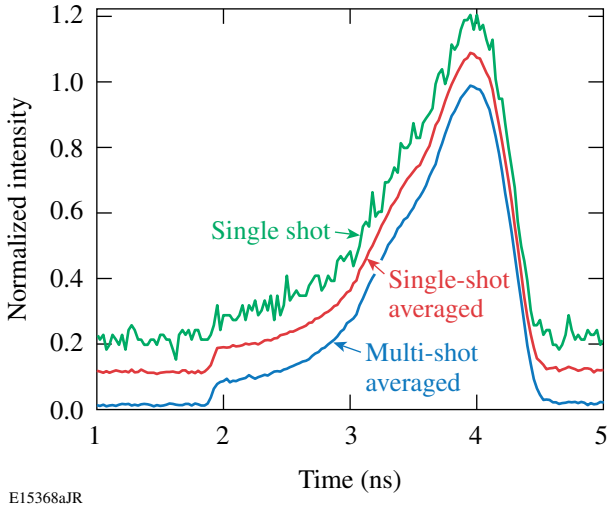

Figure 109.66
Single-shot, single-shot–averaged, and multi-shot–averaged pulse shapes. Arbitrary offsets have been added for clarity.

for all cases, increased signal amplitude corresponds directly to increased dynamic range. For the single-shot–averaging case, the data point is plotted versus the average amplitude of all of the peaks in the 64-pulse train. This plot clearly demonstrates that single-shot averaging works just as well as multi-shot averaging without the disadvantages of reduced acquisition time and the loss of single-shot events. For further comparison, the manufacturer's specifications rate the oscilloscope at 5.5 ENOB, corresponding to a maximum dynamic range of 45. The single-shot–averaging technique demonstrates a dynamic range of 312, or an ENOB of 8.3, an improvement of nearly 3 bits over the nominal performance of the oscilloscope. This level of improvement is expected from the averaging function; since the SNR is reduced by $\sqrt{N}$ and the maximum signal remains nearly the same, the dynamic range is improved by the same factor, for which $\sqrt{64} = 2^3$.

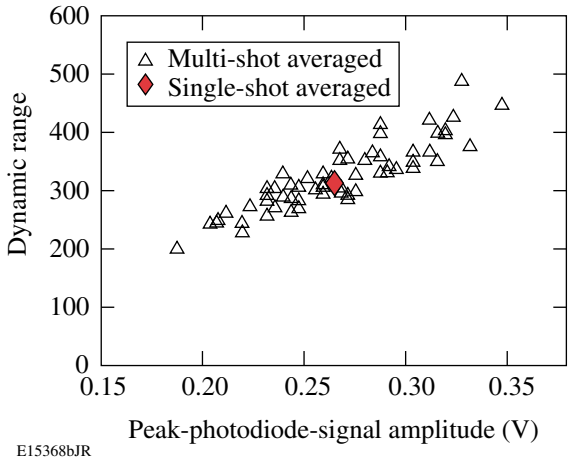

Figure 109.67
Dynamic range of single-shot–averaged and multi-shot–averaged pulses

Discussion and Conclusions

In principle, this method can be extended to a larger number of pulses in the pulse stacker, thereby achieving even better dynamic range and SNR. The ultimate limitation is peak-detected signal power, which is reduced by a factor of 2 every time the number of pulses is doubled. Provided the laser system has sufficient energy to spare for the measurement, the upper limitation on power launched is driven by damage and nonlinear effects in the fiber.

For spectrally narrowband pulses, stimulated Brillouin scattering (SBS) becomes the limiting factor in power launched into the fiber. The conventional threshold equation for the SBS threshold is $g_B P_0 L_{\text{eff}} / A_{\text{eff}} = 21$, where g_B is the Brillouin gain, P_0 is the threshold peak power, L_{eff} is the effective interaction length, and A_{eff} is the effective mode area.[9] Since the light scattered by SBS is in the reverse propagation direction, the effective length of the interaction is determined by the time of flight of the pulse in the fiber. Using typical numbers for 1053 nm, the SBS energy threshold for a 1-ns pulse is of the order of several microjoules.

Conventional damage thresholds for fibers are near 5 J/cm^2 for a 1-ns pulse, although higher values have been reported.[10] Using the more-conservative value leads to an upper energy limit of the order of a few microjoules for a single-mode fiber at 1053 nm (~6-μm core). Together, damage and SBS considerations limit the maximum launched power to a few microjoules.

The receiver of the system also has its limitations. Generally, detection of low light levels may lead to signal-to-noise issues; therefore, higher light levels are desired. However, the photodiode itself has an upper limit of peak signal power before the pulse becomes distorted by space-charge effects that arise when the extracted charge exceeds more than a few percent of the charge stored in the photodiode. For the Discovery DSC-30 photodiodes that were used, the power was limited to approximately 10 pJ per pulse in the pulse train; reasonably beyond that value, pulse-shape distortion became noticeable.

Together, the fiber launch energy and the photodiode linearity determine the maximum dynamic range of the detected signals. The single-pulse energy after passing through the system is given by $(\eta/2)^N$, where η is the transmission of the coupler and N is the number of stages. Using the energy limitations described above with a conservative 0.6-dB insertion loss for the couplers, a total of 14 stages can be utilized. Thus, this technique can be extended to achieve an increase of 7 bits over the nominal oscilloscope performance.

In conclusion, measuring pulse shapes beyond the dynamic range of oscilloscopes is achieved by passive temporal-pulse stacking. Pulses are averaged with their time-delayed replicas without introducing additional noise or jitter, allowing for high-contrast pulse-shape measurements of single-shot events. A dynamic-range enhancement of 3 bits is demonstrated experimentally, and the technique can be extended to yield an increase of up to 7 bits of additional dynamic range over nominal oscilloscope performance. Moreover, single-shot averaging does not suffer from temporal jitter; therefore it can produce higher bandwidth measurements than conventional multi-shot averaging.

ACKNOWLEDGMENT

This work was supported by the U.S. Department of Energy Office of Inertial Confinement Fusion under Cooperative Agreement No. DE-FC52-92SF19460, the University of Rochester, and the New York State Energy Research and Development Authority. The support of DOE does not constitute an endorsement by DOE of the view expressed in this article.

REFERENCES

1. J. D. Lindl, *Inertial Confinement Fusion: The Quest for Ignition and Energy Gain Using Indirect Drive* (Springer-Verlag, New York, 1998).
2. P. W. McKenty, V. N. Goncharov, R. P. J. Town, S. Skupsky, R. Betti, and R. L. McCrory, Phys. Plasmas **8**, 2315 (2001).
3. S. Luan *et al*., Meas. Sci. Technol. **4**, 1426 (1993).
4. A. Jullien *et al*., Opt. Lett. **30**, 920 (2006).
5. W. R. Donaldson, R. Boni, R. L. Keck, and P. A. Jaanimagi, Rev. Sci. Instrum. **73**, 2606 (2002).
6. A. Jolly, J. F. Gleyze, and J. C. Jolly, Opt. Commun. **264**, 89 (2006).
7. G. C. Vogel, A. Savage, and M. A. Duguay, IEEE J. Quantum Electron. **QE-10**, 642 (1974).
8. K.-L. Deng *et al*., IEEE Photonics Technol. Lett. **10**, 397 (1998).
9. G. P. Agrawal, *Nonlinear Fiber Optics*, 2nd ed., Optics and Photonics Series (Academic Press, San Diego, 1995), pp. 50–54.
10. A. Galvanauskas, presented at Frontiers in Optics 2006/Laser Science XXII, Rochester, NY 8–12 October 2006 (Paper FWA5).

Publications and Conference Presentations

Publications

R. Betti, K. Anderson, T. R. Boehly, T. J. B. Collins, R. S. Craxton, J. A. Delettrez, D. H. Edgell, R. Epstein, V. Yu. Glebov, V. N. Goncharov, D. R. Harding, R. L. Keck, J. H. Kelly, J. P. Knauer, S. J. Loucks, J. A. Marozas, F. J. Marshall, A. V. Maximov, D. N. Maywar, R. L. McCrory, P. W. McKenty, D. D. Meyerhofer, J. Myatt, P. B. Radha, S. P. Regan, C. Ren, T. C. Sangster, W. Seka, S. Skupsky, A. A. Solodov, V. A. Smalyuk, J. M. Soures, C. Stoeckl, W. Theobald, B. Yaakobi, C. Zhou, J. D. Zuegel, J. A. Frenje, C. K. Li, R. D. Petrasso, and F. H. Séguin, "Progress in Hydrodynamics Theory and Experiments for Direct-Drive and Fast Ignition Inertial Confinement Fusion," Plasma Phys. Control. Fusion **48**, B153 (2006) (invited).

R. Betti and J. Sanz, "Bubble Acceleration in the Ablative Rayleigh–Taylor Instability," Phys. Rev. Lett. **97**, 205002 (2006).

R. Betti, A. A. Solodov, J. A. Delettrez, and C. Zhou, "Gain Curves for Direct-Drive Fast-Ignition at Densities Around 300 g/cc," Phys. Plasmas **13**, 100703 (2006).

J. Bromage, C. Dorrer, I. A. Begishev, N. G. Usechak, and J. D. Zuegel, "Highly Sensitive, Single-Shot Characterization for Pulse Widths from 0.4 to 85 ps Using Electro-Optic Shearing Interferometry," Opt. Lett. **31**, 3523 (2006).

I. Carusotto, S. X. Hu, L. A. Collins, and A. Smerzi, "Bogoliubov-Čerenkov Radiation in a Bose-Einstein Condensate Flowing Against an Obstacle," Phys. Rev. Lett. **97**, 260403 (2006).

V. Yu. Glebov, D. D. Meyerhofer, T. C. Sangster, C. Stoeckl, S. Roberts, C. A. Barrera, J. R. Celeste, C. J. Cerjan, L. S. Dauffy, D. C. Eder, R. L. Griffith, S. W. Haan, B. A. Hammel, S. P. Hatchett, N. Izumi, J. R. Kimbrough, J. A. Koch, O. L. Landen, R. A. Lerche, B. J. MacGowan, M. J. Moran, E. W. Ng, T. W. Phillips, P. M. Song, R. Tommasini, B. K. Young, S. E. Caldwell, G. P. Grim, S. C. Evans, J. M. Mack, T. J. Sedillo, M. D. Wilke, D. C. Wilson, C. S. Young, D. Casey, J. A. Frenje, C. K. Li, R. D. Petrasso, F. H. Séguin, J. L. Bourgade, L. Disdier, M. Houry, I. Lantuejoul, O. Landoas, G. A. Chandler, G. W. Cooper, R. J. Leeper, R. E. Olson, C. L. Ruiz, M. A. Sweeney, S. P. Padalino, C. Horsfield, and B. A. Davis, "Development of Nuclear Diagnostics for the National Ignition Facility," Rev. Sci. Instrum. **77**, 10E715 (2006) (invited).

V. Yu. Glebov, C. Stoeckl, T. C. Sangster, C. Mileham, S. Roberts, and R. A. Lerche, "High-Yield Bang Time Detector for the OMEGA Laser," Rev. Sci. Instrum. **77**, 10E712 (2006).

B. Hu, R. Betti, and J. Manickam, "Kinetic Stability of the Internal Kink Mode in ITER," Phys. Plasmas **13**, 112505 (2006).

S. X. Hu, "Quantum Study of Slow Electron Collisions with Rydberg Atoms," Phys. Rev. A **74**, 062716 (2006).

Z. Jiang and J. R. Marciante, "Mode-Area Scaling of Helical-Core, Dual-Clad Fiber Lasers and Amplifiers Using an Improved Bend-Loss Model," J. Opt. Soc. Am. B **23**, 2051 (2006).

J. P. Knauer, F. J. Marshall, B. Yaakobi, D. Anderson, B. A. Schmitt, K. M. Chandler, S. A. Pikuz, T. A. Shelkovenko, M. D. Mitchell, and D. A. Hammer, "Response Model for Kodak Biomax-MS Film to X Rays," Rev. Sci. Instrum. **77**, 10F331 (2006).

T. Z. Kosc, C. J. Coon, G. V. Babcock, K. L. Marshall, A. Trajkovska-Petkoska, and S. D. Jacobs, "Exploring Motion Reversal in Polymer Cholesteric-Liquid-Crystal Devices," in *Liquid Crystals X*, edited by I.-C. Khoo (SPIE, Bellingham, WA, 2006), Vol. 6332, p. 633209.

T. Z. Kosc, A. A. Kozlov, and A. W. Schmid, "Formation of Periodic Microstructures on Multilayer Dielectric Gratings Prior to Total Ablation," Opt. Express **14**, 10,921 (2006).

N. N. Lepeshkin, S. G. Lukishova, R. W. Boyd, and K. L. Marshall, "Feedback-Free, Single-Beam Pattern Formation by Nanosecond Pulses in Dye-Doped Liquid Crystals," in *Liquid Crystals X*, edited by I.-C. Khoo (SPIE, Bellingham, WA, 2006), Vol. 6332, p. 63320A.

F. J. Marshall, J. P. Knauer, D. Anderson, and B. L. Schmitt, "Absolute Calibration of Kodak Biomax-MS Film Response to X Rays in the 1.5- to 8-keV Energy Range," Rev. Sci. Instrum. **77**, 10F308 (2006).

K. L. Marshall, A. G. Noto, G. Painter, and N. Tabiryan, "Computational Chemistry Methods for Predicting the Chiroptical Properties of Liquid Crystal Systems. II. Application to Chiral Azobenzenes," in *Liquid Crystals X*, edited by I.-C. Khoo (SPIE, Bellingham, WA, 2006), Vol. 6332, p. 63320C.

P. W. McKenty, M. D. Wittman, and D. R. Harding, "Effect of Experimentally Observed Hydrogenic Fractionation in Inertial Confinement Fusion Ignition Target Performance," J. Appl. Phys. **100**, 073302 (2006).

A. V. Okishev and J. D. Zuegel, "Intracavity-Pumped Raman Laser Action in a Mid-IR, Continuous-Wave (cw) MgO:PPLN Optical Parametric Oscillator," Opt. Express **14**, 12,169 (2006).

G. P. Pepe, M. Amanti, C. De Lisio, R. Latempa, N. Marrocco, L. Parlato, G. Peluso, A. Barone, R. Sobolewski, and T. Taneda, "Ultrafast Photoresponse of Superconductor/Ferromagnet Nb/NiCu Heterostructures," Phys. Stat. Sol. C **3**, 2968 (2006).

T. C. Sangster and J. M. Soures, "Validation of Direct-Drive Ignition Target Design on OMEGA," American Nuclear Society, Fusion Energy Division Newsletter (June 2006), p. 10.

M. B. Schneider, D. E. Hinkel, O. L. Landen, D. H. Froula, R. F. Heeter, A. B. Langdon, M. J. May, J. McDonald, J. S. Ross, M. S. Singh, L. J. Suter, K. Widmann, B. K. Young, H. A. Baldis, C. Constantin, R. Bahr, V. Yu. Glebov, W. Seka, and C. Stoeckl, "Plasma Filling in Reduced-Scale Hohlraums Irradiated with Multiple Beam Cones," Phys. Plasmas **13**, 112701 (2006).

V. A. Smalyuk, S. B. Dumanis, J. A. Delettrez, V. Yu. Glebov, D. D. Meyerhofer, S. P. Regan, T. C. Sangster, and C. Stoeckl, "Hot-Core Assembly in Cryogenic D_2 Direct-Drive Spherical Implosions," Phys. Plasmas **13**, 104502 (2006).

C. Stoeckl, V. Yu. Glebov, P. A. Jaanimagi, J. P. Knauer, D. D. Meyerhofer, T. C. Sangster, M. Storm, S. Sublett, W. Theobald, M. H. Key, A. J. MacKinnon, P. Patel, D. Neely, and P. A. Norreys, "Operation of Target Diagnostics in a Petawatt Laser Environment," Rev. Sci. Instrum. **77**, 10F506 (2006) (invited).

W. Theobald, J. E. Miller, T. R. Boehly, E. Vianello, D. D. Meyerhofer, T. C. Sangster, J. H. Eggert, and P. M. Celliers, "X-Ray Preheating of Window Materials in Direct-Drive Shock-Wave Timing Experiments," Phys. Plasmas **13**, 122702 (2006).

A. Trajkovska, C. Kim, K. L. Marshall, T. H. Mourey, and S. H. Chen, "Photoalignment of a Nematic Liquid Crystal Fluid and Glassy–Nematic Oligofluorenes on Coumarin-Containing Polymer Films," Macromolecules **39**, 6983 (2006).

Forthcoming Publications

B. Ashe, K. L. Marshall, C. Giacofei, A. L. Rigatti, T. J. Kessler, A. W. Schmid, J. B. Oliver, J. Keck, and A. Kozlov, "Evaluation of Cleaning Methods for Multilayer Diffraction Gratings," to be published in the Proceedings of SPIE.

V. Bagnoud, J. D. Zuegel, N. Forget, and C. Le Blanc, "High-Dynamic-Range Temporal Measurements of Short Pulses Amplified by OPCPA," to be published in Optics Express.

P. Brijesh, T. J. Kessler, J. D. Zuegel, and D. D. Meyerhofer, "Demonstration of a Horseshoe-Shaped Longitudinal Focal Profile," to be published in the Journal of the Optical Society of America B.

T. J. B. Collins, J. A. Marozas, R. Betti, D. R. Harding, P. W. McKenty, P. B. Radha, S. Skupsky, V. N. Goncharov, J. P. Knauer, and R. L. McCrory, "One-Megajoule, Wetted-Foam Target Design Performance for the NIF," to be published in Physics of Plasmas (invited).

C. Dorrer, "High-Speed Characterization for Optical Telecommunication Signals," to be published in the Proceedings of SPIE (invited).

C. Dorrer and J. D. Zuegel, "Design and Analysis of Binary Shapers Using the Error-Diffusion Algorithm," to be published in the Journal of the Optical Society of America B.

D. H. Edgell, R. S. Craxton, L. M. Elasky, D. R. Harding, S. J. Verbridge, M. D. Wittman, and W. Seka, "Three-Dimensional Characterization of Cryogenic Targets Using Systems Identification Techniques with Multiple Shadowgraph Views," to be published in Fusion Science and Technology.

G. N. Gol'tsman, O. Minaeva, A. Korneev, M. Tarkhov, I. Rubstova, A. Divochiy, I. Milostnaya, G. Chulkova, N. Kaurova, B. Voronov, D. Pan, J. Kitaygorsky, A. Cross, A. Pearlman, I. Komissarov, W. Słysz, M. Węgrzecki, P. Grabiec, and R. Sobolewski, "Middle-Infrared to Visible-Light Ultrafast Superconducting Single-Photon Detectors," to be published in IEEE Transactions on Applied Superconductivity.

V. N. Goncharov, "Ablative Richtmyer–Meshkov Instability: Theory and Experimental Results," to be published in the Proceedings of the Scottish Universities Summer Schools in Physics.

V. N. Goncharov, "Direct-Drive Inertial Fusion: Basic Concepts and Ignition Target Designing," to be published in the Proceedings of the Scottish Universities Summer Schools in Physics.

W. Guan and J. R. Marciante, "Dual-Frequency Operation in a Short-Cavity Ytterbium-Doped Laser," to be published in IEEE Photonics Technology Letters.

M. Haurylau, S. P. Anderson, K. L. Marshall, and P. M. Fauchet, "Electrically Tunable Silicon 2-D Photonic Bandgap Structures," to be published in IEEE Journal of Quantum Electronics.

S. X. Hu, "Producing Ultracold and Trappable Antihydrogen Atoms," to be published in Physical Review Letters.

S. D. Jacobs, "Manipulating Mechanics and Chemistry in Precision Optics Finishing," to be published in Science and Technology of Advanced Materials.

M. Khafizov, X. Li, R. Sobolewski, Y. Cui, and X. X. Xi, "Mechanisms of Light Detection by Superconducting Current-Biased MgB_2 Microbridges," to be published in IEEE Transactions on Applied Superconductivity.

J. Kitaygorsky, I. Komissarov, A. Jukna, D. Pan, O. Minaeva, N. Kaurova, A. Divochiy, A. Korneev, M. Tarkhov, B. Voronov, I. Milostnaya, G. Gol'tsman, and R. Sobolewski, "Dark Counts in Nanostructured NbN Superconducting Single-Photon Detectors and Bridges," to be published in IEEE Transactions on Applied Superconductivity.

T. Z. Kosc, K. L. Marshall, A. Trajkovska-Petkoska, K. Hasman, C. J. Coon, G. V. Babcock, R. Howe, M. Leitch, and S. D. Jacobs, "Development of Polymer Cholesteric Liquid Crystal Flake Technology for Electro-Optic Devices and Particle Displays," to be published in the Proceedings of SPIE (invited).

B. E. Kruschwitz, J. H. Kelly, M. J. Shoup III, L. J. Waxer, E. C. Cost, E. T. Green, Z. M. Hoyt, J. Taniguchi, and T. W. Walker, "High-Contrast Plasma-Electrode Pockels Cell (PEPC)," to be published in Applied Optics.

X. Li, M. Khafizov, Š. Chromik, M. Valerianova, V. Štrbík, P. Odier, and R. Sobolewski, "Ultrafast Photoresponse Dynamics of Current-Biased Hg-Ba-Ca-Cu-O Superconducting Microbridges," to be published in IEEE Transactions on Applied Superconductivity.

S. G. Lukishova, A. W. Schmid, R. Knox, P. Freivald, L. Bissell, R. W. Boyd, C. R. Stroud, Jr., and K. L. Marshall, "Room-Temperature Source of Single Photons of Definite Polarization," to be published in the Journal of Modern Optics.

J. A. Marozas, "Fourier Transform-Based Continuous Phase-Plate Design Technique: A High-Pass Phase-Plate Design as an Application for OMEGA and the NIF," to be published in the Journal of the Optical Society of America.

J. E. Miller, T. R. Boehly, D. D. Meyerhofer, P. M. Celliers, J. H. Eggert, D. G. Hicks, C. M. Sorce, J. A. Oertel, and P. Emmel, "A Streaked Optical Pyrometer System for Laser-Driven Shock-Wave Experiments on OMEGA," to be published in Review of Scientific Instruments.

J. Myatt, W. Theobald, J. A. Delettrez, C. Stoeckl, M. Storm, T. C. Sangster, A. V. Maximov, and R. W. Short, "High-Intensity Laser Interactions with Solid Targets and Implications for Fast-Ignition Experiments on OMEGA EP," to be published in Physics of Plasmas (invited).

S. Papernov and A. W. Schmid, "Using Gold Nanoparticles as Artificial Defects in Thin Films: What Have We Learned About Laser-Induced Damage Driven by Localized Absorbers?" to be published in the Proceedings of SPIE.

S. P. Regan, R. Epstein, V. N. Goncharov, I. V. Igumenshchev, D. Li, P. B. Radha, H. Sawada, T. R. Boehly, J. A. Delettrez, O. V. Gotchev, J. P. Knauer, J. A. Marozas, F. J. Marshall, R. L. McCrory, P. W. McKenty, D. D. Meyerhofer, T. C. Sangster, S. Skupsky, V. A. Smalyuk, B. Yaakobi, and R. Mancini, "Laser-Energy Coupling, Mass Ablation Rate, and Shock Heating in Direct-Drive Inertial Confinement Fusion," to be published in Physics of Plasmas (invited).

T. C. Sangster, R. Betti, R. S. Craxton, J. A. Delettrez, D. H. Edgell, L. M. Elasky, V. Yu. Glebov, V. N. Goncharov, D. R.

Harding, D. Jacobs-Perkins, R. Janezic, R. L. Keck, J. P. Knauer, S. J. Loucks, L. D. Lund, F. J. Marshall, R. L. McCrory, P. W. McKenty, D. D. Meyerhofer, P. B. Radha, S. P. Regan, W. Seka, W. T. Shmayda, S. Skupsky, V. A. Smalyuk, J. M. Soures, C. Stoeckl, B. Yaakobi, J. A. Frenje, C. K. Li, R. D. Petrasso, F. H. Séguin, J. D. Moody, J. A. Atherton, B. D. MacGowan, J. D. Kilkenny, T. P. Bernat, and D. S. Montgomery, "Cryogenic DT and D_2 Targets for Inertial Confinement Fusion," to be published in Physics of Plasmas (invited tutorial).

S. N. Shafrir, J. C. Lambropoulos, and S. D. Jacobs, "A Magnetorheological Polishing-Based Approach for Studying Precision Microground Surfaces of Tungsten Carbides," to be published in Precision Engineering.

S. N. Shafrir, J. C. Lambropoulos, and S. D. Jacobs, "Technical Note: Toward Magnetorheological Finishing of Magnetic Materials," to be published in the Journal of Manufacturing Science and Engineering.

W. Słysz, M. Węgrzecki, J. Bar, P. Grabiec, M. Górska, V. Zwiller, C. Latta, P. Böhi, A. J. Pearlman, A. S. Cross, D. Pan, J. Kitaygorsky, I. Komissarov, A. Verevkin, I. Milostnaya, A. Korneev, O. Minayeva, G. Chulkova, K. Smirnov, B. Voronov, G. N. Gol'tsman, and R. Sobolewski, "Fiber-Coupled, Single-Photon Detector Based on NbN Superconducting Nanostructures for Quantum Communications," to be published in the Journal of Modern Optics.

V. A. Smalyuk, R. Betti, J. A. Delettrez, V. Yu. Glebov, V. N. Goncharov, D. Y. Li, D. D. Meyerhofer, S. P. Regan, S. Roberts, T. C. Sangster, C. Stoeckl, W. Seka, J. A. Frenje, C. K. Li, R. D. Petrasso, and F. H. Séguin, "Experimental Studies of Direct-Drive, Low-Intensity, Low-Adiabat Spherical Implosions on OMEGA," to be published in Physics of Plasmas.

S. Sublett, J. P. Knauer, I. V. Igumenshchev, A. Frank, and D. D. Meyerhofer, "Double-Pulse Laser-Driven Jets on OMEGA," to be published in Astrophysics and Space Science.

S. Wu, D. Wang, P. Geiser, J. Jun, J. Karpinski, and R. Sobolewski, "Time-Resolved Intervalley Transitions in GaN Single Crystals," to be published in the Journal of Applied Physics.

L. Zheng, A. W. Schmid, and J. C. Lambropoulos, "Surface Effects on Young's Modulus and Hardness of Fused Silica by Nanoindentation Study," to be published in the Journal of Material Science.

C. D. Zhou, W. Theobald, R. Betti, P. B. Radha, V. A. Smalyuk, D. Shvarts, V. Yu. Glebov, C. Stoeckl, K. S. Anderson, D. D. Meyerhofer, T. C. Sangster, C. K. Li, R. D. Petrasso, J. A. Frenje, and F. H. Séguin, "High-ρR Implosions for Fast-Ignition Fuel Assembly," to be published in Physical Review Letters.

Conference Presentations

The following presentations were made at the 17th Target Fabrication Meeting, San Diego, CA, 1–5 October 2006:

D. H. Edgell, R. S. Craxton, L. M. Elasky, D. R. Harding, S. J. Verbridge, M. D. Wittman, and W. Seka, "Three-Dimensional Characterization of Cryogenic Targets Using Systems Identification Techniques with Multiple Shadowgraph Views."

L. M. Elasky, S. J. Verbridge, A. Weaver, D. H. Edgell, and D. R. Harding, "Developments in Layering OMEGA D_2 Cryogenic Targets."

L. M. Elasky, A. Weaver, S. J. Verbridge, R. Janezic, and W. T. Shmayda, "Tritium Migration in MCTC's During DT Introduction."

R. Q. Gram and D. R. Harding, "Thermal Conductivity of Condensed D_2 and D_2 in RF Foam Using the 3-ω Method."

D. R. Harding, L. M. Elasky, S. J. Verbridge, A. Weaver, and D. H. Edgell, "Forming Cryogenic DT Ice Layers for OMEGA."

R. Janezic, "Operational Challenges in Filling and Transferring Cryogenic DT Targets."

R. Janezic, "Performance of the Tritium Removal Systems at LLE."

A. K. Knight, D. R. Harding, "Evaluating the Dependence of the Roughness of Polyimide Capsules and Processing Conditions."

L. D. Lund, D. Jacobs-Perkins, D. H. Edgell, R. Orsagh, J. Ulreich, and R. Early, "Cryogenic Target Positioning and Stability on OMEGA."

S. Scarantino, M. Bobeica, and D. R. Harding, "Performance of the Cryogenic Test Facility Used to Simulate the Effect

of Injecting an Inertial Fusion Energy Target into a Hot Target Chamber."

W. T. Shmayda, M. J. Bonino, D. R. Harding, P. S. Ebey, and D. C. Wilson, "Hydrogen Isotope Exchange in Plastic Targets."

D. Turner, M. J. Bonino, J. Ulreich, and R. Orsagh, "Measuring and Optimizing the Dynamics of Spherical Cryogenic Targets on OMEGA."

M. D. Wittman and D. R. Harding, "Isotopic Fractionation During Solidification and Sublimation of Hydrogen-Isotope Mixtures."

The following presentations were made at Frontiers in Optics 2006/Laser Science XXII, Rochester, NY, 8–12 October 2006:

W. Guan and J. R. Marciante, "Gain Apodization in Highly Doped Fiber DFB Lasers."

W. Guan and J. R. Marciante, "Single-Frequency, 2-cm, Yb-Doped Silica Fiber Laser."

Z. Jiang and J. R. Marciante, "Loss Measurements for Optimization of Large-Mode-Area, Helical-Core Fibers."

A. V. Okishev and J. D. Zuegel, "Highly Stable, Long-Pulse, Diode-Pumped Nd:YLF Regenerative Amplifier."

L. Sun and J. R. Marciante, "Filamentation Analysis in Large-Area-Mode Fiber Lasers."

J. D. Zuegel, J. H. Kelly, L. J. Waxer, V. Bagnoud, I. A. Begishev, J. Bromage, C. Dorrer, B. E. Kruschwitz, T. J. Kessler, S. J. Loucks, D. N. Maywar, R. L. McCrory, D. D. Meyerhofer, S. F. B. Morse, J. B. Oliver, A. L. Rigatti, A. W. Schmid, C. Stoeckl, S. Dalton, L. Folnsbee, M. J. Guardalben, R. Jungquist, J. Puth, M. J. Shoup III, and D. Weiner, "New and Improved Technologies for the OMEGA EP High-Energy Petawatt Laser" (invited).

D. D. Meyerhofer, "Research Using Chirped-Pulse–Amplification Lasers at the University of Rochester," OSA Annual Meeting and APS Laser Science Meeting, Rochester, NY, 8–12 October 2006 (invited).

The following presentations were made at Optical Fabrication and Testing, Rochester, NY, 9–11 October 2006:

J. E. DeGroote, A. E. Marino, A. L. Bishop, and S. D. Jacobs, "Using Mechanics and Polishing Particle Properties to Model Material Removal for Magnetorheological Finishing (MRF) of Optical Glasses."

J. E. DeGroote, J. P. Wilson, T. M. Pfunter, and S. D. Jacobs, "Adding Chemistry and Glass Composition Data into a Mechanical Material Removal Model for Magnetorheological Finishing (MRF)."

S. N. Shafrir, J. C. Lambropoulos, and S. D. Jacobs, "A Magnetorheological Polishing-Based Approach for Studying Magnetic/Nonmagnetic WC Hard Metals," ASPE 21st Annual Meeting, Monterey, CA, 15–20 October 2006.

T. C. Sangster, R. L. McCrory, V. N. Goncharov, D. R. Harding, S. J. Loucks, P. W. McKenty, D. D. Meyerhofer, S. Skupsky, B. A. Hammel, J. D. Lindl, E. Moses, J. Atherton, G. B. Logan, S. Yu, J. D. Kilkenny, A. Nikroo, H. Wilken, K. Matzen, R. Leeper, R. Olsen, J. Porter, C. Barnes, J. C. Fernandez, D. Wilson, J. D. Sethian, and S. Obenschain, "Overview of Inertial Fusion Research in the United States," 21st IAEA Fusion Energy Conference, Chendu, China, 16–21 October 2006.

S. D. Jacobs, "Manipulating Mechanics and Chemistry in Precision Optics Finishing," International 21st Century COE Symposium on Atomistic Fabrication Technology, Osaka, Japan, 19–20 October 2006.

W. Guan and J. R. Marciante, "Dual-Frequency Ytterbium-Doped Fiber Laser," LEOS 2006, Montreal, Quebec, Canada, 29 October–2 November 2006.

The following presentations were made at the 48th Annual Meeting of the APS Division of Plasma Physics, Philadelphia, PA, 30 October–3 November 2006:

K. S. Anderson, R. Betti, P. W. McKenty, P. B. Radha, and M. M. Marinak, "2-D Simulations of OMEGA Fast-Ignition Cone Targets."

R. Betti, K. S. Anderson, C. Zhou, L. J. Perkins, M. Tabak, P. Bedrossian, and K. N. LaFortune, "Shock Ignition of Thermonuclear Fuel with High Areal Density."

T. R. Boehly, V. N. Goncharov, D. D. Meyerhofer, J. E. Miller, T. C. Sangster, V. A. Smalyuk, P. M. Celliers, G. W. Collins, D. Munro, and R. E. Olson, "Direct- and Indirect-Drive Shock-Timing Experiments on the OMEGA Laser."

D. T. Casey, J. A. Frenje, C. K. Li, J. R. Rygg, F. H. Séguin, R. D. Petrasso, V. Yu. Glebov, B. Owens, D. D. Meyerhofer, T. C. Sangster, P. Song, S. W. Haan, S. P. Hatchett, R. A. Lerche, M. J. Moran, D. C. Wilson, R. Leeper, and R. E. Olson, "Diagnosing Cryogenic DT Implosions Using the Magnetic Recoil Spectrometer (MRS)."

T. J. B. Collins, J. A. Marozas, R. Betti, D. R. Harding, P. W. McKenty, P. B. Radha, S. Skupsky, V. N. Goncharov, J. P. Knauer, and R. L. McCrory, "One-Megajoule, Wetted-Foam Target Design Performance for the NIF" (invited).

J. A. Delettrez, J. Myatt, C. Stoeckl, and D. D. Meyerhofer, "Hydrodynamic Simulations of Integrated Fast-Ignition Experiments Planned for the OMEGA/OMEGA EP Laser Systems."

D. H. Edgell, R. S. Craxton, L. M. Elasky, D. R. Harding, L. S. Iwan, R. L. Keck, L. D. Lund, S. J. Verbridge, A. Weaver, M. D. Wittman, and W. Seka, "Layering and Characterization of Cryogenic-DT Targets for OMEGA."

R. Epstein, H. Sawada, V. N. Goncharov, D. Li, P. B. Radha, and S. P. Regan, "K-Shell Absorption Spectroscopy at Low Temperatures in Preheat Conditions."

J. A. Frenje, D. T. Casey, C. K. Li, J. R. Rygg, F. H. Séguin, R. D. Petrasso, P. B. Radha, V. Yu. Glebov, D. D. Meyerhofer, and T. C. Sangster, "Diagnosing Cryogenic D_2 and DT Implosions on OMEGA Using Charged-Particle Spectroscopy."

M. Ghilea, D. D. Meyerhofer, T. C. Sangster, D. J. Lonobile, A. Dillenbeck, R. A. Lerche, and L. Disdier, "Developmental Status of a Liquid-Freon Bubble Chamber for Neutron Imaging."

V. Yu. Glebov, T. C. Sangster, P. B. Radha, W. T. Shmayda, M. J. Bonino, D. R. Harding, D. C. Wilson, P. S. Ebey, A. Nobile, Jr., R. A. Lerche, and T. W. Phillips, "Measurement of the Neutron Energy Spectrum in T-T Inertial Confinement Fusion."

V. N. Goncharov, V. A. Smalyuk, W. Seka, T. R. Boehly, R. L. McCrory, I. A. Igumenshchev, J. A. Delettrez, W. Manheimer, and D. Colombant, "Thermal Transport Modeling in ICF Direct-Drive Experiments."

O. V. Gotchev, M. D. Barbero, N. W. Jang, J. P. Knauer, and R. Betti, "A Compact, TIM-Based, Pulsed-Power System for Magnetized Target Experiments on OMEGA."

S. Hu, V. N. Goncharov, V. A. Smalyuk, J. P. Knauer, and T. C. Sangster, "Analysis of the Compressibility Experiments Performed on the OMEGA Laser System."

I. V. Igumenshchev, V. N. Goncharov, V. A. Smalyuk, W. Seka, D. H. Edgell, T. R. Boehly, and J. A. Delettrez, "Effects of Resonant Absorption in Direct-Drive Experiments on OMEGA."

N. W. Jang, R. Betti, J. P. Knauer, O. V. Gotchev, and D. D. Meyerhofer, "Theory and Simulation of Laser-Driven Magnetic-Field Compression."

J. P. Knauer, P. W. McKenty, K. S. Anderson, T. J. B. Collins, and V. N. Goncharov, "Direct-Drive, Foam-Target ICF Implosions."

C. K. Li, F. H. Séguin, J. A. Frenje, J. R. Rygg, R. D. Petrasso, R. P. J. Town, P. A. Amendt, S. P. Hatchett, D. G. Hicks, O. L. Landen, V. A. Smalyuk, T. C. Sangster, and J. P. Knauer, "Measuring E and B Fields in Laser-Produced Plasmas Through Monoenergetic Proton Radiography."

D. Li, I. V. Igumenshchev, and V. N. Goncharov, "Effects of the Ion Viscosity on the Shock Yield and Hot-Spot Formation in ICF Targets."

G. Li, C. Ren, V. N. Goncharov, and W. B. Mori, "The Channeling Effect in the Underdense Plasma."

J. A. Marozas, P. W. McKenty, P. B. Radha, and S. Skupsky, "Imprint Simulations of 1.5-MJ NIF Implosions Using a Refractive 3-D Laser Ray Trace with an Analytic SSD Model."

F. J. Marshall, R. S. Craxton, M. J. Bonino, R. Epstein, V. Yu. Glebov, D. Jacobs-Perkins, J. P. Knauer, J. A. Marozas, P. W. McKenty, S. G. Noyes, P. B. Radha, W. Seka, S. Skupsky, and V. A. Smalyuk, "Optimized Polar-Direct-Drive Experiments on OMEGA."

A. V. Maximov, J. Myatt, and R. W. Short, "Laser–Plasma Coupling Near Critical Density in Direct-Drive ICF Plasmas."

P. W. McKenty, J. A. Marozas, V. N. Goncharov, K. S. Anderson, R. Betti, D. D. Meyerhofer, P. B. Radha, T. C. Sangster, S. Skupsky, and R. L. McCrory, "Numerical Investigation of Proposed OMEGA Cryogenic Implosions Using Adiabat-Shaping Techniques."

D. D. Meyerhofer, T. C. Sangster, K. S. Anderson, R. Betti, R. S. Craxton, J. A. Delettrez, D. H. Edgell, R. Epstein, V. Yu. Glebov, V. N. Goncharov, D. R. Harding, R. L. Keck, J. D. Kilkenny, J. P. Knauer, S. J. Loucks, L. D. Lund, F. J. Marshall, R. L. McCrory, P. W. McKenty, P. B. Radha, S. P. Regan, W. Seka, V. A. Smalyuk, J. M. Soures, C. Stoeckl, S. Skupsky, J. A. Frenje, C. K. Li, R. D. Petrasso, and F. H. Séguin, "Studies of Adiabat Shaping in Direct-Drive, Cryogenic-Target Implosions on OMEGA."

J. E. Miller, T. R. Boehly, A. Melchior, and D. D. Meyerhofer, "Thermal and Kinetic Equation-of-State Experiments Using Decaying Shock Waves."

J. Myatt, A. V. Maximov, and R. W. Short, "Positron–Electron, Pair-Plasma Production on OMEGA EP."

J. Myatt, W. Theobald, J. A. Delettrez, C. Stoeckl, M. Storm, T. C. Sangster, A. V. Maximov, and R. W. Short, "High-Intensity Laser Interactions with Solid Targets and Implications for Fast-Ignition Experiments on OMEGA EP" (invited).

P. Nilson, "Magnetic Reconnection and Plasma Dynamics in Two Beam Laser–Solid Interactions."

R. D. Petrasso, C. K. Li, F. H. Séguin, J. A. Frenje, J. R. Rygg, M. Manuel, V. A. Smalyuk, R. Betti, R. S. Craxton, J. P. Knauer, F. J. Marshall, D. D. Meyerhofer, J. Myatt, P. B. Radha, T. C. Sangster, W. Theobald, R. P. J. Town, P. A. Amendt, P. M. Celliers, S. P. Hatchett, D. G. Hicks, O. L. Landen, J. Cobble, N. M. Hoffman, and J. D. Kilkenny, "Monoenergetic Particle Backlighter for Radiography and Measuring E and B Fields and Plasma Areal Density."

P. B. Radha, V. Yu. Glebov, V. N. Goncharov, D. D. Meyerhofer, T. C. Sangster, S. Skupsky, J. A. Frenje, and R. D. Petrasso, "Inferring Areal Density in OMEGA DT-Cryogenic Implosions."

S. P. Regan, R. Epstein, V. N. Goncharov, I. V. Igumenshchev, D. Li, P. B. Radha, H. Sawada, T. R. Boehly, J. A. Delettrez, O. V. Gotchev, J. P. Knauer, J. A. Marozas, F. J. Marshall, R. L. McCrory, P. W. McKenty, D. D. Meyerhofer, T. C. Sangster, S. Skupsky, V. A. Smalyuk, B. Yaakobi, and R. Mancini, "Laser-Energy Coupling, Mass Ablation Rate, and Shock Heating in Direct-Drive Inertial Confinement Fusion" (invited).

S. P. Regan, D. D. Meyerhofer, T. C. Sangster, R. Epstein, L. J. Suter, O. S. Jones, N. B. Meezan, M. D. Rosen, S. Dixit, C. Sorce, O. L. Landen, J. Schein, and E. L. Dewald, "Hohlraum Energetics with Elliptical Phase Plates on OMEGA."

J. R. Rygg, J. A. Frenje, C. K. Li, F. H. Séguin, R. D. Petrasso, and V. N. Goncharov, "Time-Dependent Nuclear Measurements of Fuel–Shell Mix in ICF Implosions."

T. C. Sangster, R. Betti, R. S. Craxton, J. A. Delettrez, D. H. Edgell, L. M. Elasky, V. Yu. Glebov, V. N. Goncharov, D. R. Harding, D. Jacobs-Perkins, R. Janezic, R. L. Keck, J. P. Knauer, S. J. Loucks, L. D. Lund, F. J. Marshall, R. L. McCrory, P. W. McKenty, D. D. Meyerhofer, P. B. Radha, S. P. Regan, W. Seka, W. T. Shmayda, S. Skupsky, V. A. Smalyuk, J. M. Soures, C. Stoeckl, B. Yaakobi, J. A. Frenje, C. K. Li, R. D. Petrasso, F. H. Séguin, J. D. Moody, J. A. Atherton, B. D. MacGowan, J. D. Kilkenny, T. P. Bernat, and D. S. Montgomery, "Cryogenic DT and D_2 Targets for Inertial Confinement Fusion" (invited tutorial).

T. C. Sangster, R. S. Craxton, J. A. Delettrez, D. H. Edgell, R. Epstein, V. Yu. Glebov, V. N. Goncharov, D. R. Harding, R. L. Keck, J. D. Kilkenny, J. P. Knauer, S. J. Loucks, L. D. Lund, J. A. Marozas, F. J. Marshall, R. L. McCrory, P. W. McKenty, D. D. Meyerhofer, P. B. Radha, S. P. Regan, W. Seka, V. A. Smalyuk, J. M. Soures, C. Stoeckl, S. Skupsky, J. A. Frenje, C. K. Li, R. D. Petrasso, and F. H. Séguin, "Implosion Performance of Fully β-Layered Cryogenic-DT Targets on OMEGA" (invited).

J. Sanz and R. Betti, "Bubble Acceleration in the Ablative Rayleigh–Taylor Instability."

H. Sawada, S. P. Regan, R. Epstein, D. Li, V. N. Goncharov, P. B. Radha, D. D. Meyerhofer, T. R. Boehly, V. A. Smalyuk, T. C. Sangster, B. Yaakobi, and R. Mancini, "Investiga-tion of Direct-Drive Shock Heating Using X-Ray Absorption Spectroscopy."

F. H. Séguin, C. K. Li, J. A. Frenje, J. R. Rygg, R. D. Petrasso, V. A. Smalyuk, R. S. Craxton, J. P. Knauer, F. J. Marshall, T. C. Sangster, S. Skupsky, A. Greenwood, and J. D. Kilkenny, "Using Target Shimming to Compensate for Asymmetric Drive in ICF Implosions."

W. Seka, V. N. Goncharov, J. A. Delettrez, D. H. Edgell, I. V. Igumenshchev, R. W. Short, A. V. Maximov, J. Myatt, and R. S. Craxton, "Time-Dependent Absorption Measurements in Direct-Drive Spherical Implosions."

R. W. Short and J. Myatt, "Instabilities of Relativistic Electron Beams in Plasmas: Spatial Growth and Absolute Instability."

S. Skupsky, "Nonlocal Ion-Heat Transport in ICF Implosions."

A. A. Solodov, R. Betti, J. A. Delettrez, and C. Zhou, "Gain Curves for Fast-Ignition Inertial Confinement Fusion."

J. M. Soures, T. R. Boehly, V. N. Goncharov, S. Hu, D. D. Meyerhofer, J. E. Miller, T. C. Sangster, W. Seka, and V. A. Smalyuk, "Spherical Shock-Breakout Measurements on OMEGA."

C. Stoeckl, J. Bromage, J. H. Kelly, T. J. Kessler, B. E. Kruschwitz, S. J. Loucks, R. L. McCrory, D. D. Meyerhofer, S. F. B. Morse, A. L. Rigatti, T. C. Sangster, W. Theobald, L. J. Waxer, and J. D. Zuegel, "Status of the OMEGA EP High-Energy Petawatt Laser Facility."

M. Storm, J. Myatt, and C. Stoeckl, "Characterization of Fast-Electron Beam Propagation Through Solid-Density Matter by Optical-Transition Radiation."

S. Sublett, J. P. Knauer, D. D. Meyerhofer, I. V. Igumenshchev, T. J. B. Collins, and A. Frank, "Influence of Episodic Mass Ejection on Hydrodynamic Jet Evolution."

W. Theobald, C. Stoeckl, C. Zhou, R. Betti, S. Roberts, V. A. Smalyuk, V. Yu. Glebov, J. A. Delettrez, T. C. Sangster, D. D. Meyerhofer, C. K. Li, and R. D. Petrasso, "High-Areal-Density Fuel-Assembly Experiments for the Fast-Ignitor Concept."

C. Zhou and R. Betti, "Fast-Ignition Fuel-Assembly Scaling Laws: Theory and Experiments."

The following presentations were made at the 9th International Fast Ignition Workshop, Cambridge, MA, 3–5 November 2006:

K. S. Anderson, R. Betti, P. W. McKenty, P. B. Radha, and M. M. Marinak, "2-D Simulations of OMEGA Fast-Ignition Cone Targets."

J. A. Delettrez, J. Myatt, C. Stoeckl, D. D. Meyerhofer, and M. G. Haines, "Hydrodynamic Simulations of Integrated Fast-Ignition Experiments Planned for the OMEGA/OMEGA EP Laser Systems."

D. D. Meyerhofer, R. Betti, V. N. Goncharov, D. H. Edgell, D. R. Harding, J. H. Kelly, T. J. Kessler, S. J. Loucks, L. D. Lund, R. L. McCrory, S. F. B. Morse, T. C. Sangster, W. Seka, C. Stoeckl, W. Theobald, L. J. Waxer, and J. D. Zuegel, "Preparations for Integrated Cryogenic Fast-Ignition Experiments on OMEGA/OMEGA EP" (invited).

J. Myatt, A. V. Maximov, and R. W. Short, "Laboratory Demonstration of e^+e^- Pair-Plasma Production on OMEGA EP."

J. Myatt, W. Theobald, J. A. Delettrez, C. Stoeckl, M. Storm, T. C. Sangster, A. V. Maximov, and R. W. Short, "High-Intensity Laser Interactions with Solid Targets and Implications for Fast-Ignition Experiments on OMEGA EP" (invited).

P. Nilson, "Optical Probing of Underdense Laser–Plasma Interactions Using the Vulcan Petawatt Laser."

A. A. Solodov, R. Betti, J. A. Delettrez, and C. Zhou, "Gain Curves for Fast-Ignition Inertial Confinement Fusion."

C. Stoeckl, S.-W. Bahk, J. Bromage, V. Yu. Glebov, O. V. Gotchev, P. A. Jaanimagi, D. D. Meyerhofer, P. Nilson, T. C. Sangster, M. Storm, S. Sublett, W. Theobald, and J. D. Zuegel, "Diagnostics for Fast-Ignitor Experiments on OMEGA/OMEGA EP."

W. Theobald, C. Stoeckl, K. S. Anderson, R. Betti, T. R. Boehly, J. A. Delettrez, R. Epstein, V. Yu. Glebov, J. H. Kelly, T. J. Kessler, B. E. Kruschwitz, S. J. Loucks, R. L. McCrory, D. N. Maywar, D. D. Meyerhofer, J. E. Miller, S. F. B. Morse, J. Myatt, P. B. Radha, A. L. Rigatti, T. C. Sangster, V. A. Smalyuk, L. J. Waxer, B. Yaakobi, J. C. Zhou, J. D. Zuegel, R. D. Petrasso, C. K. Li, C. A. Back, G. Hund, R. B. Stephens, S. P. Hatchett, M. H. Key, A. J. MacKinnon, H.-S. Park, P. K. Patel, K. L. Lancaster, and P. A. Norreys, "Fast-Ignition Research at the Laboratory for Laser Energetics."

C. Zhou and R. Betti, "Fast-Ignition Fuel-Assembly Scaling Laws."

UNIVERSITY OF
ROCHESTER